Università degli Studi di Milano-Bicocca

SCUOLA DI DOTTORATO

Corso di Dottorato di Ricerca in Scienza e Nanotecnologia dei Materiali

Advanced Spectroscopic Investigations of Colloidal Semiconductor Nanostructures for Photon Management and Radiation Detection Schemes

Candidate:
Matteo Luca Zaffalon
Matr.748697

Tutor:
Prof. Sergio Brovelli

Coordinator:
Prof. Marco Bernasconi

Academic Year 2020/2021

To boldly go where
no one has gone before
[G. Roddenberry]

Contents

Acknowledgments

I want to thank and express my gratitude to the Nanotechnology and Advanced Spectroscopy Team at the Los Alamos National Laboratory for hosting and welcoming me during my visiting period in Los Alamos. I am particularly grateful to Dr. Victor Klimov and Dr. Young-Shin Park for the stimulating discussions and teachings which have significantly improved my way of interpreting my research.

I also thank the PhD Coordinator Prof. Marco Bernasconi and the Materials Science Department for the fellowship that supported my PhD and for making the resources and equipment available as well as for giving me the opportunity to participate in important international scientific events.

The results and conclusions reported later in this thesis are the outcome of collaboration with different research groups who have synthesized the nanomaterials or made their equipment available to add value and completeness to my research. I would particularly like to thank the group of Dr. Liberato Manna (Italian Institute of Technology, Genoa, IT), the Glass To Power Spa (Rovereto, IT) team, and the group of Prof. Liang Li (Shanghai Jiao Tong University, Shanghai, PRC) for the synthesis of the nanostructures presented in this thesis; Dr. Scott A. Crooker (Los Alamos National Labotatory, NM, USA) for the magneto-optic measurements, the research group of Prof. Margherita Zavelani-Rossi (Politecnico di Milano, Milan, IT) for letting me use the ultra-fast transient absorption facilities, and the team of ENEA Casaccia, Calliope γ-ray facility (Rome, IT), for making the radiation hardness studies possible.

Chapter 1

Introduction

It was 1959 when Dr. Richard Feynman gave his lecture entitled "There's a plenty of room at the bottom" and there are those who make the start of the nanotechnology race coincide with this event. Feynman's vision offers his contemporaries the prospect of a physical synthesis that, regardless of any molecular alchemy, starts with atomic manipulation to obtain every chemical substance. Approaching the atomic dimensions, materials progressively overcome the boundaries of classical physics by entering a purely quantum regime that opens up a vastness of opportunities and strategies to obtain completely different properties otherwise inaccessible. From this point of view, the understanding of the physics of nanomaterials, in addition to obvious fundamental reasons, takes on specific and actual technological relevance. Semiconductor colloidal nanocrystals (NCs) appeared in the scientific landscape over 30 years ago with the pioneering work of Dr. Louis E. Brus in the late 1980s. To date, NCs continue to collect a vast interest in the worldwide community of nanosciences thanks to their unique and peculiar physics capable of combining the intimate manipulation of electronic wave functions with the ease of synthesis and processing of colloidal solutions.

More recently, wave function manipulation has extended beyond the established concept of size control and quantum confinement, paving the way for a new set of paradigms and tool sets borrowed from the long-standing semiconductor physics such as heterostructuring and controlled doping introducing energy states that participate in the photophysics of the system. The new flexible functionalities and their intimate control have opened to the first commercial technologies based on nanocrystals such as light emitting devices (LEDs, full color displays), large-area luminescent solar concentrators (LSCs), fast scintillators or cutting-edge applications such as single-photon

emission, also for bioimaging and sensing [1, 2]. The continuous achievements confirm the lively interest of the community of physicists, chemists, materials scientists and engineers in the field of nanotechnologies and in particular that of colloidal nanocrystals. Despite these successes, many fundamental aspects of NCs synthesis and photophysics are still debated and require a deeper understanding of the elusive physics underlying their optical properties. The results of these studies shall define new clear guidelines for the design and synthesis of novel materials that meet the current technological needs in terms of energy supply and efficiency, as well as for the environment protection and health. To contribute to these tasks, in this thesis I focus on the fundamental study of photophysics and scintillation properties of novel colloidal nanocrystals such as heavy metals-free I-III-VI_2 and single- or double-perovskites using advanced spectroscopies such as ultra-fast transient absorption, spectro-electrochemistry and thermally-stimulated luminescence, filling the gaps and promoting new strategies that could implement their perspective applications.

In Chapter 2 I present a detailed study on the energetics of the band edge exciton in ternary I-III-VI_2 NCs of stoichiometric $CuInS_2$ and $AgInS_2$. For this aim, I use a combination of complementary spectroscopic techniques such as ultrafast transient absorption, magnetic circular dichroism and time-resolved photoluminescence (PL) at cryogenic temperatures revealing the presence of intrinsic sub-levels with different parity in the NC valence band responsible for the peculiar optical properties of this class of NCs. Specifically, the difference in energy between the absorption edge and the photoluminescence - as well its dynamics - are function of the NC size. These results are incorporated in a Monte Carlo ray-tracing simulation to model the performance of stoichiometric $CuInS_2$ as a near zero self-absorption chromophore in colorless LSCs. Following such theoretical insights, a large-area LSC prototype with record efficiency is fabricated embedding $CuInS_2$ NCs, with optimal size, capable of maximizing solar harvesting while mitigating self-absorption losses. These results are therefore extended to $AgInS_2$ NCs, a less investigated material to date, confirming also in this case the intrinsic origin of the largely Stokes-shifted PL as a result of the detailed structure of the valence band.

In Chapter 3 I propose an extensive discussion on the topic of ionizing radiation detection through high-atomic number nanostructures of $CsPbBr_3$. To unlock their full potential as reliable and cost-effective alternatives to conventional scintillators, lead-halide perovskites (LHPs) urge to conjugate several features such as high scintillation

yield, fast and Stokes-shifted emission, and emission stability over prolonged exposure to high doses of ionizing radiation. In this chapter these issues are addressed by performing, for the first time, a comprehensive study on $CsPbBr_3$ using radioluminescence (RL) and PL measurements side-by-side to thermally-stimulated luminescence (TSL) and afterglow experiments. First, will be studied the sensitization process of a conjugated organic dye coupled to $CsPbBr_3$ NCs, designed so as to exhibit a largely Stokes-shifted and fast luminescence. Their applicability in real-world scenarios will be also demonstrated by simulating scintillation waveguiding performances and by testing α-particles detection over large surfaces. Then, will be illustrated an in-depth investigation of the scintillation mechanisms of $CsPbBr_3$ as a function of the material's dimensionality (namely, nanocubes, nanowires, nanosheets, and bulk single-crystals). By means of temperature-controlled RL and PL measurements side-by-side to TSL and afterglow experiments on $CsPbBr_3$, will be revealed the interplay between the band-edge exciton and shallow/deep trap states affecting the PL and the scintillation yield. Overall, these results will offer a solid platform upon which will be presented novel synthetic strategies to suppress trapping sites at the NC surfaces. As a result, in the last section of this chapter, will be demonstrated that post-synthetic resurfacing with fluorine ions passivates the NC surface unlocking the technological potential of $CsPbBr_3$ NCs for radiation detection and conversion. The stability of $CsPbBr_3$ NCs will be tested in terms of radiation hardness for γ-radiation. Side-by-side PL and RL measurements will demonstrate the PL and scintillation yields stability upon extreme delivered γ-doses (1 MGy), also showing that the suppression of surface defects with F^- ions preserves the band-edge origin of RL with a 6-fold enhancement of the light-yield compared to standard NCs. The (de)trapping-related phenomena are investigated trough TSL and afterglow measurements revealing the residual presence of a-thermal tunneling from shallow defects at the NC surface whose substantial suppression via fluorination makes minority thermal processes - previously observed in $CsPbBr_3$ bulk crystals - visible.

Finally, in Chapter 4, I'll characterize a novel class of lead-free double perovskite (DP) NCs of composition $Cs_2B^+InCl_6$ (with B^+ = Na, K) and Rb_3InCl_6 NCs which are emerging as environmental friendly alternatives to conventional LHP. By combining temperature controlled and time-resolved PL spectroscopies, I will elucidated the origin of luminescence in Sb-doped DP NCs also evaluating the role of $[SbCl_6]$ octahedra connectivity in determining the Stokes shift's amplitude and the luminescence efficiency. In view of applications for radiation detection, I verified the hardness of DPs up to 500

Gy through RL measurements, while Monte Carlo simulations show essentially perfect waveguiding performance in large-area devices. The Sb-doped Rb_3InCl_6 NCs, despite the higher PL quantum yield, have instead a main RL contribution originating from the host lattice which overlaps with their absorption profile making then unsuitable for large-area detectors. These results suggest a new, still unexplored materials design concept for Stokes shift engineering via B^+ cation substitution with great potential for light management technologies based on wavelength-shifting waveguides.

Chapter 2

The Intrinsic Origin of Stokes-Shifted Emission in Ternary I-III-VI_2 Nanocrystals Enables Record Efficient Large-Area Luminescent Solar Concentrators

Ternary (I-III-VI_2) $CuInS_2$ and $AgInS_2$ nanocrystals (NCs), valued for their efficient and largely Stokes-shifted photoluminescence, are receiving attention as heavy-metals-free materials for solar cells, luminescent solar concentrators (LSCs), LEDs, and bio-imaging. The origin of the optical properties of this class of NCs are however not fully understood. A recent theoretical model suggests that their characteristic Stokes-shifted and long-lived luminescence arises from the structure of the valence band and predicts distinctive optical behaviours in defect-free NCs: the quadratic dependence of the radiative decay rate and the Stokes shift on the NC radius. If confirmed, this would have crucial implications for LSCs as the solar spectral coverage ensured by low-bandgap NCs would be accompanied by increased re-absorption losses. In this chapter, is introduced a detailed spectroscopic investigation of stoichiometric $CuInS_2$ and $AgInS_2$ NCs, revealing for the first time the spectroscopic signatures predicted for the free band-edge exciton, thus supporting the VB-structure model. By combining complementary spectroscopic techniques, will be revealed the excitonic recombination pathways also identifying the main loss channels whose suppression leads to emission efficiencies close to unity. Such fundamental photophysical knowledge is then exploited to formulate new design

guidelines for the fabrication of large-area LSCs based on stoichiometric $CuInS_2$ NCs, suitable for building integration, featuring optical power efficiency as high as 6.8%, corresponding to the highest value reported to date for large-area devices.

2.1 State of the Art

Ternary semiconductor nanocrystals of I–III–VI_2 composition, such as $CuInS_2$, $AgInS_2$, or $CuGaSe_2$, are attracting considerable interest for numerous energy and optoelectronic technologies including photovoltaic (PV) cells [3–8], luminescent solar concentrators [9–12], light emitting diodes [13–17], as well as bioimaging [16, 18, 19] where their inherent lower toxicity offers a significant advantage over Cd- and Pb-based NCs. In addition to their heavy-metal-free composition, I–III–VI_2 NCs feature important electronic and photophysical properties, such as degenerate p-type transport [20, 21] and broadband absorption tunable from visible to near infrared [22–27] that is spectrally very well separated from an efficient, longlived photoluminescence (i.e. a very large Stokes shift) [28, 29]. This characteristic optical behavior makes I–III–VI_2 NCs the most promising chromophores for efficient LSCs, combining effective harvesting of the solar spectrum and reabsorption-free waveguiding of the propagating luminescence. As a result, efficient solar concentration has been demonstrated in large area devices [9–12, 30, 31] that further feature neutral coloring particularly adapt for architectural integration of LSCs as, i.e. PV windows [9, 32]. Despite tremendous advancements in this field, the fundamental photophysics of I–III–VI_2 NCs is still not fully understood, in particular concerning the long luminescence decay time and the characteristic wide global Stokes shift, Δ_{SS}^{G}, between the absorption and emission spectra [33], resulting in the lack of clear design guidelines for their optimization.

As discussed in the following, the term "global" is used here to indicate that, in contrast to the norm, the electronic transitions determining the spectral energies for absorption and emission in I–III–VI_2 are not the same [33, 34]. Mostly based on the similarity between the luminescence spectral shape, lifetime, and Stokes shift of $CuInS_2$ NCs and those of copper doped II–VI NCs [33,35,36] —and by analogy those of $AgInS_2$ to silver-doped chalcogenides [36, 37] — most studies to date have considered the photoluminescence (PL) to arise from the radiative recombination of a conduction band (CB) electron with a hole localized in copper-related (silver-related) defects [9, 38, 39]. Experimental support to this argument was provided by spectroscopic, [28, 38, 40–42] spectro-electrochemical [43–45] and electrical [21] methods. Magnetooptical [46] ex-

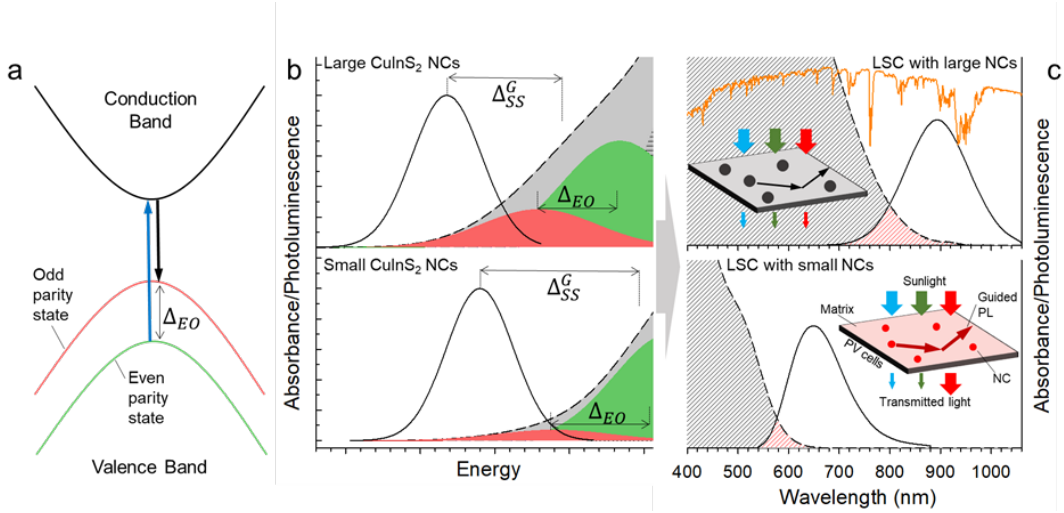

Figure 2.1: ***a)*** *Schematic depiction of the band structure of $CuInS_2$ NCs featuring odd and even parity valence band (VB) sublevels separated by a splitting energy Δ_{EO}. Optical absorption (blue arrow) is dominated by the electronic transition coupling the even VB sublevel and the conduction band (CB), whereas luminescence (black arrow) occurs by parity forbidden radiative decay of the electron into the odd VB sublevel.* ***b)*** *Representative optical properties for large (top) and small (bottom) $CuInS_2$ NCs as predicted by the VB structure model [34]. In small particles, Δ_{EO} is large resulting in small intermixing between the VB substates and negligible oscillator strength coupling the odd parity VB substates and the CB (represented by the weak red absorption band). The absorption spectrum is dominated by the even parity substates (green band), the resulting global Stokes shift, Δ^G_{SS}, is large and the low-energy absorption tail is weak. Δ_{EO} drops in larger NCs leading to larger intermixing between the VB substates and consequent broader low-energy absorption tail and smaller Δ^G_{SS}.* ***c)*** *Side-by-side comparison between the normalized PL (solid black lines, excitation at 400 nm) and optical absorption (dashed black lines) spectra of stoichiometric $CuInS_2$ NCs with radius $a = 2.2$ nm (top panel) and $a = 1.0$ nm (bottom panel). The absorption profiles are normalized to 1 OD at the respective band-edge energy evaluated from the transient transmission spectra reported in Figure 2.3. The spectral overlap between the absorption and PL profiles are highlighted by red shading to emphasize the effect of broadened absorption tail with increasing a resulting in stronger reabsorption. Insets: schematic depiction of the LSCs under solar irradiation showing uniform spectral coverage for devices embedding large NCs resulting in no spectral distortion of the transmitted light. LSCs featuring small NCs instead transmit a larger fraction of the solar spectrum above 600 nm resulting in tinted devices and low color rendering index of the transmitted light.*

periments further revealed marked temperature-dependent Zeeman splitting due to *sp-d* exchange interaction between band-edge carriers and paramagnetic Cu^{2+} cations (with $3d^9$ electronic configuration) in both Cu-doped II-VI NCs and nonstoichiometric $CuInS_2$ NCs (Cu/In ratios between 1.25 and 1.45). [46, 47] Strongly nonlinear magnetic field dependence of the circular polarization-resolved emission observed in both Cu:ZnSe NCs and $CuInS_2$ NCs [35, 46] with respect to the linear trend typically found

in undoped CdSe NCs, further corroborated the picture that emission from nonstoichiometric $CuInS_2$ NCs involves localized dopant or defect states that feature a complex splitting of their level structure in applied magnetic fields. According to this picture, single particle experiments on copper deficient $CuInS_2$ NCs (1:2 Cu/In precursor ratio) by Zang et al. [42] revealed markedly narrower single NC PL spectra with respect to the ensemble (60 meV vs 400 meV) that, together with the weak temperature dependence of the PL linewidth, [43, 48] suggest that the broad ensemble PL spectrum is mostly determined by the energy distribution of defect acceptor sites among different particles. Recent transport measurements [21] support this argument. [49] The same study further highlighted the presence of In-related substitutional and/or interstitial defects acting as donors in indium treated NCs, in agreement with the excitonic pathway mediated by donor defects proposed by Kraaz et al. [50] and Leach et al. [38] An alternative interpretation ascribes the photophysics of $CuInS_2$ NCs to the recombination of self-trapped excitons featuring a strongly localized hole in the highest occupied molecular orbital due to the 3d states of Cu^+ cations. [35, 51]

2.1.1 The Valence Band Structure Model for Stoichiometric $CuInS_2$ Nanocrystals

A recent theory by Efros and co-workers [34] proposes a very different possibility, namely that the characteristic broadband optical absorption spectrum, long PL lifetimes and wide Δ_{SS}^{G} can be explained by the structure of the valence band (VB). Specifically, effective mass calculations highlight a VB structure featuring low-energy odd parity hole sublevels of p-type symmetry (corresponding to the high energy VB sublevel depicted in red in the single electron diagram of Figure 2.1) separated by a splitting energy, Δ_{EO}, from higher-lying even parity hole levels (corresponding to the green VB sublevel in Figure 2.1a), whose wavefunctions have s-type contributions. As a result of the parity selection rules, the absorption spectrum is dominated by the optical transition between the even hole VB sublevel with total angular momentum F = 1 and the $1S_e$ electron level (blue arrow in Figure 2.1a), also featuring a s-type symmetry. On the other hand, the long-lived PL (black arrow in Figure 2.1a) arises from the parity-forbidden radiative transition of the $1S_e$ electron into the odd VB state also featuring F = 1. A recent work [52] provided experimental support for such a VB structure picture by showing the presence of an intense twophoton absorption transition below the one-photon absorption band edge. However, the PL of such NCs was suggested to still occur via a defect-mediated pathway, resulting in size and shape

independent Δ_{SS}^{G}, similarly to what observed by Xia et al. [40] and Grandhi et al. [53] and commonly exhibited by Cu-doped CdSe NCs. [54]

Importantly, the model by Efros and co-workers (hereafter indicated as the VB structure model) makes testable predictions [34]: the quadratic decrease of Δ_{SS}^{G} with the particle radius, a, and the linear growth of the radiative decay rate with a^2. These distinctive size dependences of the spectral and dynamical properties of I–III–VI_2 NCs arise from the linear proportionality of the admixture between the odd and even parity states with a. Specifically, as schematically depicted in Figure 2.1b (bottom panel), small $CuInS_2$ NCs exhibit a large Δ_{EO} and negligible absorption from the odd parity VB sublevels (highlighted in red) featuring vanishingly small oscillator strength, thus resulting in a large Δ_{SS}^{G}. Upon increasing the NCs size, odd and even parity sublevels come closer in energy, [34] resulting in a linear trend of Δ_{EO} with a^{-2}. The resulting intermixing between such states intensifies the low energy absorption tail in large NCs (top panel in Figure 2.1b) which ultimately leads to the linear dependence of Δ_{SS}^{G} on a^{-2}. On the same lines, increasing intermixing between VB substates should result in the linear growth of the radiative decay rate with a^2. To date, however, no study has experimentally investigated such spectroscopic signatures, leaving the model without direct experimental validation. Crucially, this photophysical scenario and in particular the progressive reduction of Δ_{SS}^{G} in larger NCs, would have important implications for the use of $CuInS_2$ NCs as reabsorption-free emitters in LSCs. This is because the wide solar coverage (SC) enabled by low bandgap (large size) NCs with broadband absorption extending the near-IR region would be accompanied by stronger reabsorption losses of the propagating luminescence with respect to smaller NCs, due to the larger overlap with the respective emission spectrum. This behavior is shown in Figure 2.1c for representative $CuInS_2$ NCs with different particle size (a = 2.2 nm vs a = 1.0 nm) discussed in detail in the next section. On the other hand, whilst small NCs would be less affected by reabsorption (Figure 2.1c, bottom panel) their SC would be limited to the visible spectral region. This would limit the maximum achievable device efficiency and result in colored LSC panels which are not ideal for building integrated PV technologies. If the VB structure model is confirmed, the realization of efficient LSCs with simultaneously optimized solar harvesting and light concentration efficiency based on $CuInS_2$ NCs would require identifying the tradeoff between such antithetical size effects.

2.2 Optical and Magneto-Optical investigation of the Band-Edge Exciton in $CuInS_2$ Nanocrystals: Novel Design Guidelines for Efficient Large-Area Luminescent Solar Concentrators

In this section the validity of the VB model for stoichiometric $CuInS_2$ NCs will be discussed through optical and magneto-optical measurements on a set of NCs of various sizes. Consistently with the model introduced by Efros and co-workers [34], optical absorption and transient transmission measurements reveal the gradual broadening of the absorption tail, resulting in the linear increase of Δ_{SS}^{G} with a^{-2}. Importantly, this behavior is accompanied by the linear growth of the PL radiative decay rate with a^2, also in agreement with the excitonic mechanism proposed in ref. [34]. In addition to this, PL measurements below $T \sim 50$ K show a 100-fold lengthening of the PL decay time, but no change in the PL quantum yield (Φ_{PL}), pointing to a further fine structure of the emitting band-edge exciton state, with splitting that scales as a^{-3}. Such a photophysics had so far never been observed in I–III–VI_2 NCs and is similar to what is well known in conventional II–VI NCs, [55, 56] suggesting that also in this class of semiconductor NCs the fine structure of the first exciton manifold might emanate from enhanced exchange interaction. [57, 58] Crucially, side-by-side time-resolved PL measurements on nonstoichiometric $CuInS_2$ NCs and Cu-doped CdSe NCs of comparable size show exclusively the lengthening of the PL lifetime with decreasing temperature due to gradual suppression of thermally assisted nonradiative decay, strongly indicating that the observed fine structure effect derives from the very nature of the intrinsic band-edge exciton of defect-free $CuInS_2$ NCs.

In order to evaluate the implications of the observed size dependence of the optical properties of $CuInS_2$ NCs on their use as LSC emitters, a Monte Carlo ray-tracing simulations based on the experimental spectra is performed. The calculations highlight the interplay between the positive effect of wider solar harvesting with increasing particle size and the detrimental stronger optical losses by reabsorption, thus suggesting guidelines for device optimization. Based on such indications, a large area (30 cm $\times$ 30 cm) plastic LSC device embedding stoichiometric $CuInS_2$ NCs with optimal size was finally fabricated and tested. By optically coupling such a device with c-Si solar cells, a record optical power efficiency (OPE) of 6.8% has been demonstrated further confirming the technological relevance of such fundamental findings.

2.2.1 Samples Description

$CuInS_2$ NCs were synthesized within the Dept. of Materials Science following a well known heat-up procedure [23,26,59,60] that ensures production of stoichiometric particles by suitably tuning the reactant concentration. [23,28,41,51] Specifically, a mixture of CuI (0.4 mmol), $In(OAc)_3$ (0.4 mmol), and 5 mL of 1-dodecanethiol (DDT) was loaded into a three-neck flask and was degassed under vacuum at 130 °C for 1 h. In order to grow particles of different sizes, the temperature was initially raised to 230 °C to let the particles nucleate and grow. Aliquots were taken at different reaction times (2.5, 5, 10, 20, 30, 40, and 60 min) in order to obtain different nanocrystal sizes. Finally, the reaction was quenched by cooling the solution to room temperature. The NCs were cleaned by repeated precipitation with acetone and redispersion in hexane. In order to synthesize copper-deficient NCs (Cu:In = 1:4) (see later in this chapter) was varied only the amount of the copper precursor (0.1 mmol). On the other hand, when a precursor ratio of 1:1 In:Cu was used, $CuInS_2$ NCs with In:Cu:S stoichiometric ratios close to 1:1:2 were obtained, as confirmed by inductively coupled plasma atomic emission spectroscopy (ICP-AES) analysis indicating a composition of $Cu_{1.04}InS_{2.01}$.

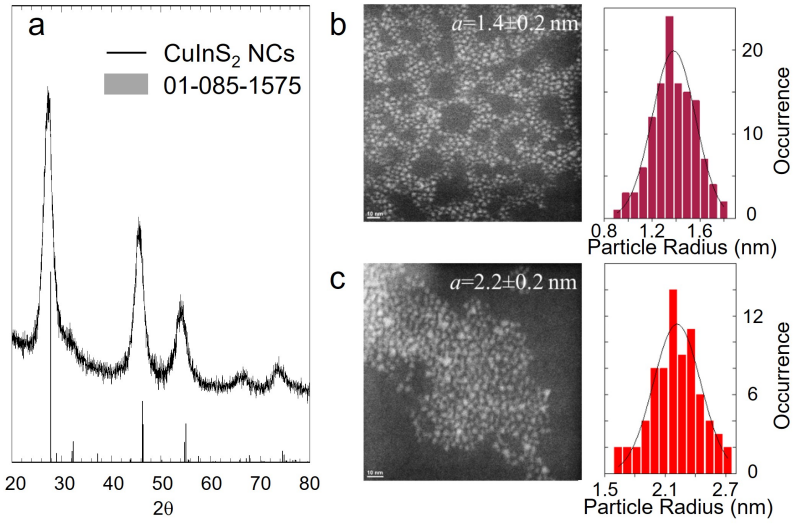

Figure 2.2: ***a)*** *X-ray diffraction pattern of representative $CuInS_2$ NCs (a=2.2±0.2 nm) together with the pattern of tetragonal-chalcopyrite-type $CuInS_2$. Transmission electron micrographs of representative $CuInS_2$ NCs featuring mean radius a=1.4±0.2 nm* ***(b)*** *and a=2.2±0.2 nm* ***(c)****.*

The $CuInS_2$ NCs present tetragonal chalcopyrite-like structure (Figure 2.2a). Transmission electron micrographs (TEM) of two representative aliquots are reported in Fig-

ure 2.2b and 2.2c showing size distribution consistent with previous reports. [40, 61] High-resolution TEM (HR-TEM) images of representative NCs in the two chosen samples mostly show spheroidal particles, rather than well-faceted shapes, especially in the smaller NCs. This holds in particular for the smallest NCs (not shown in Figure 2.2), which are harder to identify even by HR-TEM imaging, due to the low number of atoms, which hardly stabilize in an ordered (i.e., crystalline) structure, thus in an anisotropic shape.

2.2.2 Experimental Details

Spectroscopic Studies

Absorption spectra of NCs in solution were measured with a Cary 50 UV–Vis spectrophotometer. Steady-state PL measurements were performed by exciting samples at 3.06 eV with ps-pulsed diode lasers (Picoquant LDH-P series, ∼70 ps pulses). The emitted light was dispersed with a spectrometer and detected with a charged-coupled device (TM-C10083CA Hamamatsu Mini-Spectrometer). Transient PL measurements were carried out using ∼70 ps pulses at 3.06 eV from a pulsed diode laser (Picoquant LDH-P series). The emitted light was collected with a Hamamatsu R943-02 time-correlated single-photon counting unit (time resolution ∼600 ps) coupled to an Oriel Instruments Cornerstone 260 monochromator. Temperature dependent PL and trPL measurements were carried out on NC thin films drop-casted on quartz substrates and mounted inside a cryostat with optical access.

For the ultrafast transient transmission (TT) measurements, the laser source was a Ti:sapphire laser with chirped pulse amplification (Coherent LIBRA-HE), which provided 95 fs pulses at 800 nm at a repetition rate of 2 kHz. The excitation pulses at 3.1 eV were obtained by second harmonic generation in a 1mm thick β barium borate crystal. Pump pulse duration ∼150 fs. The probe beam was a white light supercontinuum generated by focusing a small fraction of the fundamental beam onto a 2 mm thick sapphire plate. After chopping the pump beam at 1kHz, pump and probe were focused on the sample by means of a lens and a spherical mirror. Pump fluence on the sample position was $\sim 80 \mu$J cm^{-2}. A computer-controlled optical multichannel analyzer working at the repetition rate of the laser source acquires the map of the differential transmission $\Delta T/T = (T_{on} - T_{off})/T_{off}$, as a function of the pump-probe time delay; T_{on} and T_{off} are the probe spectra transmitted by the excited and unperturbed samples.

Magnetic Circular Dichroism

Magnetic Circular Dichroism (MCD) measures were carried out at the National High Magnetic Filed Laboratory in Los Alamos (NM, USA) with the kind collaboration of Dr. Scott A. Crooker. In MCD measures the normalized difference in transmission between left- and right-circularly polarized light through films of nanocrystals in the Faraday geometry [62]. Nanocrystal films were mounted in the variable-temperature insert (1.5–300 K) of a 7 T superconducting magnet with direct optical access. Probe light of tunable wavelength was derived from a Xenon lamp directed through a spectrometer. The probe light was mechanically chopped at 137 Hz and was modulated between right and left circular polarizations at 50 kHz using a photoelastic modulator. The transmitted light was detected with a silicon avalanche photodiode.

The MCD measures the Zeeman splitting (ΔE_Z) between spin-up and spin-down (J=$\pm$1) excitons, which couple to right and left circularly polarized light respectively. This splitting arises from two sources: 1) the temperature-independent intrinsic g-factor of the host semiconductor, and also 2) any additional splitting arising from sp-d coupling of the exciton to embedded magnetic dopants. If these dopants are paramagnetic, then this latter contribution is temperature-dependent. MCD is experimentally performed by measuring the normalized difference between the transmission of right- and left-circularly polarized light (T_R and T_L, respectively) through the nanocrystal sample in the Faraday geometry, (T_R-T_L)/(T_R+T_L), as a function of photon energy. When the ΔE_Z is small compared with the Gaussian width of the fundamental 1S absorption peak (as is the case here), the MCD spectrum is derivative-like with a low-energy maximum amplitude that is proportional to ΔE_Z (see the calibration procedure described below). Details of the technique can be found in Ref. [62]. For any given sample, the Zeeman splitting is directly proportional to the magnitude of the MCD signal. The constant of proportionality is sample-dependent and is determined by comparing the MCD signal with the Zeeman splitting that is directly measured between separate high-resolution RCP and LCP absorption spectra. This calibration procedure is performed for every sample, typically at the highest field and lowest temperature to obtain the maximum splitting. By design, MCD is a differential technique and is therefore extremely sensitive to small Zeeman splittings; it measures the difference in transmission/absorption between RCP and LCP light, which is modulated at a known frequency and lock-in amplifier techniques are used to detect these small differences. Even very small energy splittings of order micro-electron volts give appreciable MCD signals, even on samples with broad absorption peaks.

Monte Carlo Ray-Tracing Simulations

The performance of squared LSC with increasing lateral size (L = 5 cm, 10 cm, 20 cm, 50 cm, 1 m and 2 m) are simulated via a Monte Carlo ray-tracing method, in which the photon propagation follows the geometrical optics laws. Because the LSC thickness (0.5 cm) is much larger than the light coherence length, interference has been neglected. The stochastic nature of the simulations is reflected in the fact that the ray is transmitted or reflected with the probabilities proportional to respective energy fluxes given by Fresnel Laws. The dependence of these probabilities on the state of polarization of the incident ray (e.g., s- or p-polarized) is also considered. A specific event (i.e. transmission or reflection) is chosen according to random Monte Carlo drawing. Monte Carlo ray-tracing simulations of the LSC were performed using the experimental absorption spectra of the NCs in solution and their relative photoluminescence spectra. AM 1.5G Solar spectrum is employed as LSC excitation source. Once a photon is absorbed by a NC, the subsequent fate of the excitation (i.e., reemission or nonradiative relaxation) is again determined by the Monte Carlo sampling according to the emission quantum yield, set as equal for all the samples ($\Phi_{PL} = 95\%$). The direction of reemission is distributed uniformly, and the reemission wavelength is determined using the rejection sampling applied to the accurate NCs PL spectra obtained from experiment. The ultimate fate of each photon is either loss due to nonradiative recombination or escape from the LSC via one of the interfaces. A single-ray Monte Carlo simulation is typically repeated 10^6–10^7 times to have a proper statistical averaging. A stochastic nature of simulations allows one to easily evaluate LSCs performance, such as the optical quantum efficiency (edge-emitted photons per absorbed solar photons) and the optical efficiency (edge-emitted photons per impinging solar photons).

2.2.3 Results

Optical Absorption, Steady-State Photoluminescence and Magneto-Optical Data

In Figure 2.3a are reported the optical spectra of the $CuInS_2$ NCs showing the characteristic broadband absorption profile and the Stokes-shifted PL of I–III–VI_2 NCs progressively moving to lower energy with increasing particle radius. According to previous reports, the absorption spectra show no discernible first excitonic peak, but exclusively a low energy shoulder. [16,40,63] To most accurately determine the spectral position of the dominant absorption feature, I performed ultra-fast transient transmis-

sion (TT) measurements. The TT spectra measured at low excitation fluence — when the number of photons absorbed per NC per pulse ($\langle N \rangle$) is much less than unity (dashed lines in Figure 2.3a) — are dominated by a bleaching band due to the saturation of band-edge states where carriers accumulate following intraband relaxation. [9, 28] The bleaching peak energy is used to extract the mean particle radius for the various NC aliquots by using the sizing curve provided in ref. [40–42]. The obtained NC radii for the largest NCs for which reliable TEM images can be obtained, agree with the particle size estimated from the analysis of the respective micrographs reported in Figure 2.2. The peak energy of each TT spectrum that identifies the "center of mass" of the low energy absorption due to the interplay between Δ_{EO} and the respective oscillator strength of the even and odd parity VB sublevels shifts toward the low energy portion of the respective absorption spectrum with increasing a. This is consistent with the VB structure model predicting a larger contribution from the odd VB sublevels in larger particles (Figure 2.1a) progressively broadening the absorption tail. As a result, Δ_{SS}^{G} extracted as the energy difference between the bleaching maximum and the respective PL peak (black bars in Figure 2.3a), and reported in Figure 2.3b, increases linearly with a^{-2} in agreement with the theoretical prediction. [34] This represents a first experimental evidence of the VB structure origin of the Stokes-shifted PL in stoichiometric I–III–VI_2 NCs where the radiative exciton decay does not necessarily involve an intragap defect state. As anticipated above, previous magneto-optical studies on nonstoichiometric $CuInS_2$ NCs revealed the presence of paramagnetic species in the NC, likely associated with copper-related defects, [46] similar to what observed in II–VI chalcogenide NCs doped with group-11 transition metals. [37, 47, 64] Therefore, magneto-optical experiments can be used to corroborate the absence (or reveal the presence) of such states in our stoichiometric NCs. With this in mind, two representative sets of $CuInS_2$ NCs have been sent to the National High Magnetic Field Laboratory (Los Alamos, NM, United States) for magnetic circular dichroism (MCD) measurements as a function of temperature and magnetic field. [62]

In Figure 2.4a and 2.4b are reported the MCD spectra for the smaller and large NC size of $CuInS_2$ NCs, namely $a = 1.0$ nm and $a = 2.2$ nm, at increasing magnetic field up to B = 6 T at 2.7 K, together with the corresponding linear absorption spectrum. For the smaller NCs, the MCD spectrum shows one main peak at ∼2.35 eV corresponding to the NC's absorption shoulder that intensifies with increasing magnetic field. In the inset of Figure 2.3c, is also reported the extracted Zeeman splitting energy (Δ_{EZ}) growing linearly with the magnetic field thus suggesting the absence of paramagnetic species in these NCs (details on the procedure for extracting Δ_{EZ} are reported in the

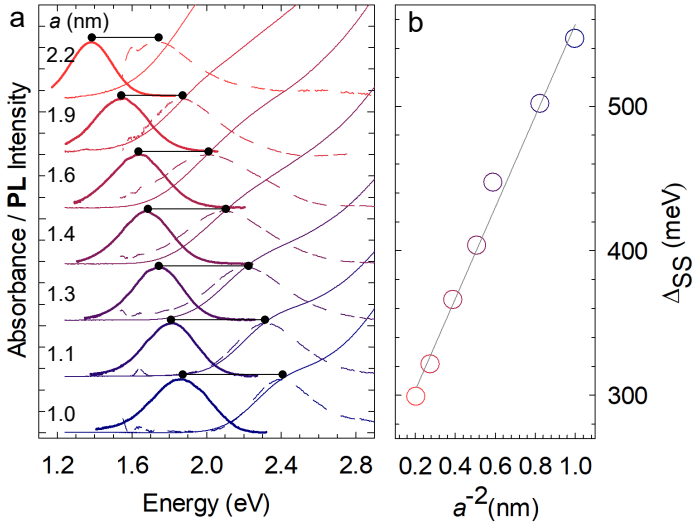

Figure 2.3: ***a)*** *Optical absorption (thin solid lines), PL spectra (bold solid lines) and normalized transient transmission (TT, dashed lines) spectra at 100 ps pump-probe delay of $CuInS_2$ NCs with increasing mean radius a. The global Stokes shift values, Δ^G_{SS}, between the absorption and PL spectra of each NC sample are indicated by black bars are reported as a function of a in panel* ***b)****. Global Stokes shift, Δ^G_{SS}, extracted as the energy difference between the peak energy of the TT and PL spectra in panel 'a' as a function of the particle size a.*

Supporting Information). Accordingly, these data are perfectly fitted with the linear Zeeman splitting function $\Delta_{EZ} = \mu_B F B g_{EX}$, where μ_B is the Bohr magneton and g_{EX} is the Landé factor of the band-edge exciton responsible for optical absorption (mostly formed by a hole in the even VB substate and a CB electron). Similar analysis and results are found for the larger NCs shown in Figure 2.4b and 2.4d. The obtained g-factor, $g_{EX} = 0.22$, also found for NCs with $a = 2.2$ nm, is in agreement with previous results on $CuInS_2$ NCs. [46] Most importantly, the magnetic response of the absorption peak (Figure 2.4c) is found to be temperature independent, in contrast to the temperature-dependent MCD that was observed in nonstoichiometric $CuInS_2$ due to paramagnetic defects. [46] Therefore, MCD data further corroborate the picture that the photophysical behavior of our stoichiometric $CuInS_2$ NCs is intrinsic.

Temperature-Controlled Time-Resolved Photoluminescence

Further support to the VB structure model emerges from the analysis of the exciton decay kinetics with increasing a. As anticipated above, within this model, gradual

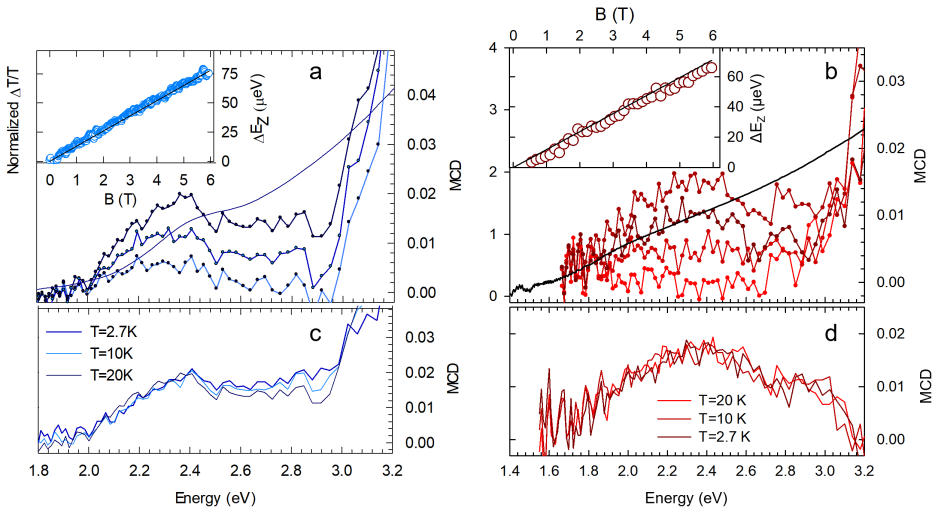

Figure 2.4: *MCD of $CuInS_2$ NCs with size $a = 1.0$ nm* ***(a)*** *and $a = 2.2$ nm* ***(b)*** *at 2.7 K and increasing magnetic field ($B = 2, 4, 6$ T). The linear absorption at 2.7 K is shown as a bold blue line. Inset: Zeeman splitting of the band-edge exciton versus magnetic field together with the fit to the linear Zeeman splitting function (black line). The respective temperature dependences of MCD at 6 T for $T = 2.7$-20 K are shown in panels* ***(c, d)****.*

intermixing between the VB substates results in an a^2-dependence of the radiative decay rate, k_{RAD}. To experimentally evaluate this effect, steady state and time-resolved PL experiments were performed. Since the Φ_{PL} and decay kinetics of $CuInS_2$ NCs are known to be strongly affected by temperature-dependent nonradiative processes, [43] I conducted the experiments at decreasing temperature from 300 to 5 K. This enables to suppress phonon-assisted nonradiative decay phenomena and thereby evaluate the evolution of k_{RAD} versus a.

To start with this part of the analysis, in Figure 2.5a I report the Φ_{PL}-values of five representative $CuInS_2$ NCs with increasing size ($a = 1.0$, 1.4, 1.6, 1.9, and 2.2 nm) from 300 to 5 K. The inset shows the evolution with T of the PL spectra of the $a = 1.0$ nm NCs. Φ_{PL} of all systems increases with decreasing T, reaching saturation at ∼100 K, thus confirming the presence of temperature-activated nonradiative channels that are suppressed at lower T. The 100 K $\leq T \leq$ 300 K interval is labeled as range **I**. For lower temperatures (range **II**), Φ_{PL} is largely constant for all systems. Consistently with previous reports, the efficiency losses in range **II** are ascribed to ultrafast trapping of photocarriers by surface defects in the absence of a wide gap passivating shell that result in a subpopulation of nonemissive NCs in the ensemble. [43] It must be highlighted that, for this study, I choose to investigate exclusively core-only $CuInS_2$ NCs, as the overgrowth of a protecting wide bandgap shell, such as ZnS, [63] typically leads to

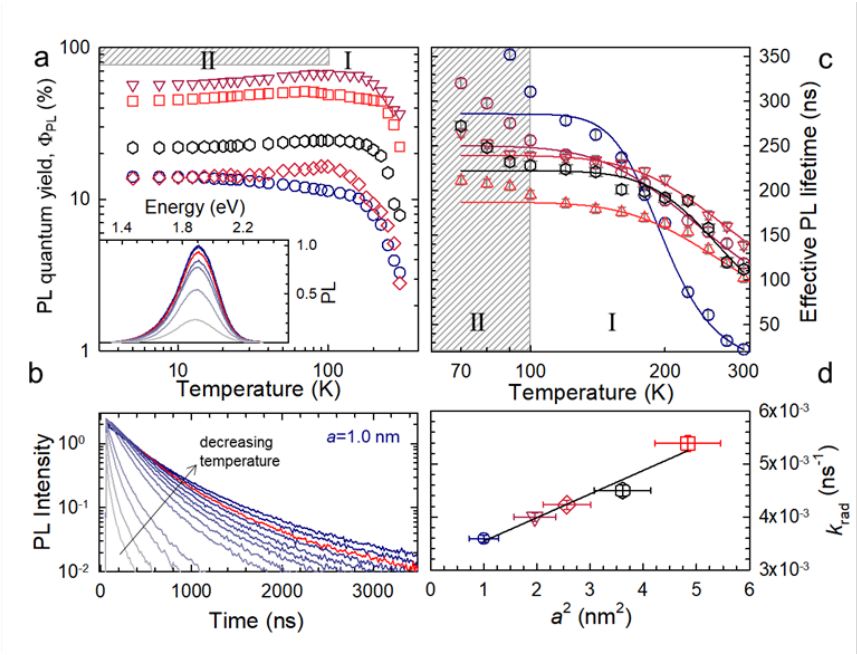

Figure 2.5: ***a)*** *PL quantum yield as a function of temperature of $CuInS_2$ NCs of increasing size, a = 1.0 (circles), 1.4 nm (triangles), 1.5 nm (diamonds), 1.9 nm (hexagons) and 2.2 nm (squares). Inset: PL spectra of $CuInS_2$ NCs with a = 1.0 nm at decreasing temperature (from grey to dark blue). The red line corresponds to T = 100 K.* ***b)*** *PL decay curves of NCs having a = 1.0 nm at decreasing temperature (indicated by the black arrow). The red line corresponds to T = 100 K.* ***c)*** *Effective PL decay times as a function of temperature (from 300 to 70 K) of the same $CuInS_2$ NCs as in panel 'a' together with the respective fitting curves to Eq.1.* ***d)*** *Effective radiative decay rates (k_{RAD}) of the same NCs showing quadratic growth with a^2 in agreement with predictions from ref. [34]. The black line represents the linear fit of k_{RAD} vs. a^2. The vertical bars are the uncertainties calculated considering the time resolution of the trPL setups. The horizontal bars are obtained by considering the dispersion of the NC size.*

the formation of alloyed quaternary particles by diffusion of Zn, which modifies the electronic structure of the core. [23, 42, 43] Nevertheless, the invariance of Φ_{PL} of the particles in range **II** confirms the temperature-independence of surface trapping and indicates that the photophysics for $T \leq 100$ K discussed later in this chapter is due to purely radiative phenomena occurring in surface trapping-free NCs.

Looking first at the PL decay curves in range **I** (Figure 2.5b) for NCs with a = 1.0 nm, are observed the typical multiexponential kinetics of unshelled $CuInS_2$ NCs that progressively slow down with decreasing T with no measurable variation of the zero-delay intensity, in agreement with the temperature independence of ultrafast charge trapping channels depleting the NC bands faster than instrumental temporal resolution. [43] Importantly, for T close to 100 K the PL decay curves accumulate indicating that

the PL process is approaching its radiative regime. To better monitor the evolution of the PL kinetics in range **I** and to evaluate the radiative decay time as a function of a, in Figure 2.5c is reported the respective effective PL lifetimes ($\tilde{\tau}$) extracted as the time after which the PL intensity drops by $1/e$. At room temperature, the $\tilde{\tau}$-values of the various NCs are uncorrelated to their respective Φ_{PL}, consistent with the major nonradiative channel being ultrafast carrier trapping that renders a subpopulation of NCs nonemissive without affecting the PL lifetime of the emissive particles. More importantly, in accordance with the Φ_{PL} trends, $\tilde{\tau}$ of all NCs increases and reaches a nearly constant value for $T\sim$100 K, based on which such a lifetime is ascribed to the effective radiative exciton decay time, $\tilde{\tau}_{RAD} = 1/k_{RAD}$, of the bright subpopulation of NCs in the ensemble. To evaluate $\tilde{\tau}_{RAD}$ for our NCs, I performed a global fit of the $\tilde{\tau}$ versus temperature trends in range **I** using the equation: $\tilde{\tau}^{-1} = \tilde{\tau}_{RAD}^{-1} + \tilde{\tau}_{NRAD}^{-1}(T)$, that neglects ultrafast surface trapping and describes the nonradiative decay rate by the standard displaced harmonic oscillator model [65]

$$\tau_{NRAD}^{-1}(T) = A * exp(-E_A/(k_B T)) \tag{2.1}$$

Through this fit, activation energies are obtained for the nonradiative decay of $E_A \sim$70 $\pm$ 4 meV. More importantly for our purposes, the k_{RAD}-values obtained through the fitting procedure grow linearly with a^2 (Figure 2.5d), in agreement with theoretical expectations based on the VB structure model.

A closer look at the lowest temperature values in Figure 2.5c, highlighted by the gray patterned area and corresponding to constant values of Φ_{PL}, reveals further increase of $\tilde{\tau}_{RAD}$ for $T < 100$ K that is particularly evident for the smallest NCs in the set. This additional temperature trend becomes evident by looking at the time-resolved PL data in range **II** shown in Figure 2.6 revealing the unexpected emergence of exciton fine structure effects in ternary I–III–VI_2 NCs. In Figure 2.6a, are reported the PL decay traces for $CuInS_2$ NCs (a = 1.0 nm) across the entire range of investigated temperatures. The PL decay curve corresponding to 100 K is shown in red to highlight the accumulation of decay lines as the thermally assisted nonradiative losses are suppressed and to mark the passage from temperature range **I** to range **II**. Strikingly, by lowering the temperature further, the PL kinetics dramatically slows down and turns from multiexponential to markedly nearly double-exponential with an initial fast portion followed by a tens of microseconds long component, over two orders of magnitude slower than the radiative kinetics at $\sim$100 K. The effect is highlighted in Figure 2.6b where are emphasized the first two decades of signal in the first 2.5 μs of decay. This

kind of kinetic behavior occurring at constant values of Φ_{PL} has been widely reported for binary chalcogenide NCs, including CdSe, [55–58] CdTe, [66] ZnSe, [67] and their heterostructures (i.e., CdTe/CdSe or CdSe/CdS NCs) [68, 69] as well as in PbSe [70] NCs, where the fast initial decay at low temperature has been ascribed to coupling of the ground state to a confined acoustic phonon or to the thermalization of excitons from a higher-energy optically allowed state (commonly referred to as the bright exciton) to a lower-lying optically forbidden (dark) exciton state. The much slower decay, on the other hand, arises from the radiative recombination of dark excitons in thermal equilibrium with the environment. [55,69] This decay becomes progressively faster with increasing temperature as a result of thermal excitation of dark excitons to the bright upper exciton state. Figure 2.6c reports the evolution of $\tilde{\tau}_{RAD}$ with temperature for five $CuInS_2$ NC samples of increasing size extracted following the procedure used in range **I** and by neglecting the initial decay portion due to rapid thermalization in range **II**. For the smallest NCs, $\tilde{\tau}_{RAD}$ approaches 20 μs at temperatures below ∼20 K and undergoes a two orders of magnitude decrease at higher temperatures ($\tilde{\tau}_{RAD}$(100 K) ∼250 ns).

In analogy to the behavior of CdSe NCs, this effect is ascribed to the thermal activation between two substates of the exciton fine structure having markedly different emission lifetime. Note that, in contrast to CdSe NCs, in $CuInS_2$ NCs both such states belong to the weakly allowed exciton consisting of a CB electron and a hole in the odd parity VB sublevel. Therefore, I adopt the language typically used to describe exciton states that are strongly and weakly forbidden by symmetry in transition metal dichalcogenide semiconductors [71] and label the long-lived exciton as dark and the higher lying emissive exciton as gray, so as to distinguish the current case from the norm, where the emissive state is optically allowed and therefore "bright." By assuming a Boltzmann distribution of excitons between these two dark (D) and gray (G) states, the transition between the slow and fast decay regimes is modeled in a simple three-level scheme (inset of Figure 2.6a), by expressing the radiative decay rate as

$$k_{RAD}(T) = \tilde{\tau}_{RAD}^{-1}(T) = \left(k_D + k_G e^{-\Delta_S/k_B T}\right)\left(1 + e^{-\Delta_S/k_B T}\right)^{-1} \tag{2.2}$$

where k_D and k_G are the radiative decay rates of dark and gray excitonic states respectively and Δ_S being the respective splitting energy. The above model reproduces the experimental data well for all $CuInS_2$ NCs, yielding Δ_S-values comparable to those found in binary chalcogenide NCs of similar size (Figure 2.6d). [57] Interestingly, as observed in CdSe NCs, Δ_S is found to scale linearly with a^{-3}, suggesting that also in $CuInS_2$ NCs

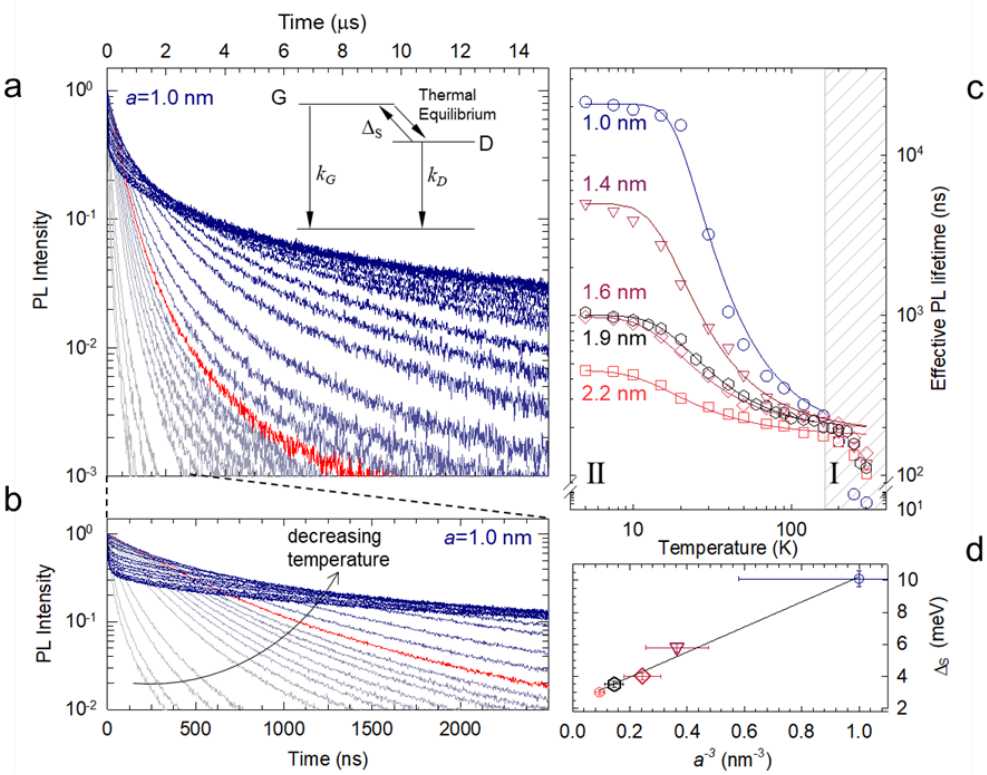

Figure 2.6: ***a)*** *PL decay curves for $CuInS_2$ NCs ($a = 1.0$ nm) at decreasing temperature from 300 K to 5 K (from grey to blue). The red line corresponds to $T = 100$ K. Inset: three-level model of grey (G) and dark (D) exciton states separated by energy Δ_S.* ***b)*** *Enlargement of the initial portion of the PL decay vs. T highlighting the appearance of the initial fast portion for T below 100 K.* ***c)*** *Effective PL decay lifetimes of $CuInS_2$ NCs of increasing size as a function of temperature together with the respective fits to Eq.2. (d) Δ_S-values extracted through the fitting procedure as a function of a^{-3}, highlighting the inverse volume dependence of the dark-grey splitting energy. The vertical bars are the uncertainties propagated through the fitting procedure using Eq.2. The horizontal bars are obtained by considering the dispersion of the NC size.*

the fine structure splitting energy follows the linear dependence with the inverse of the particles volume of the exchange energy of uncorrelated electron–hole pairs. [58] Importantly, time-resolved PL measurements on off-stoichiometry $Cu_{1-x}In_xS_2$ ($x = 0.8$) and Cu:doped CdSe NCs with $a = 1.0$ nm shown in Figure 2.7 evidence no fine structure effects in neither system. This supports the picture that the excitation responsible for the optical properties of stoichiometric $CuInS_2$ nanocrystals is of different nature than the Cu-defect emission in both off-stoichiometry $CuInS_2$ NCs and in Cu:doped II-VI chalcogenides. It is also worth noting that time-resolved PL measurements at 5 K show nearly no acceleration of the PL kinetics upon the application of a magnetic field (B = 5 T; Figure 2.8), as is instead observed in CdSe NCs due to magnetic mixing of the

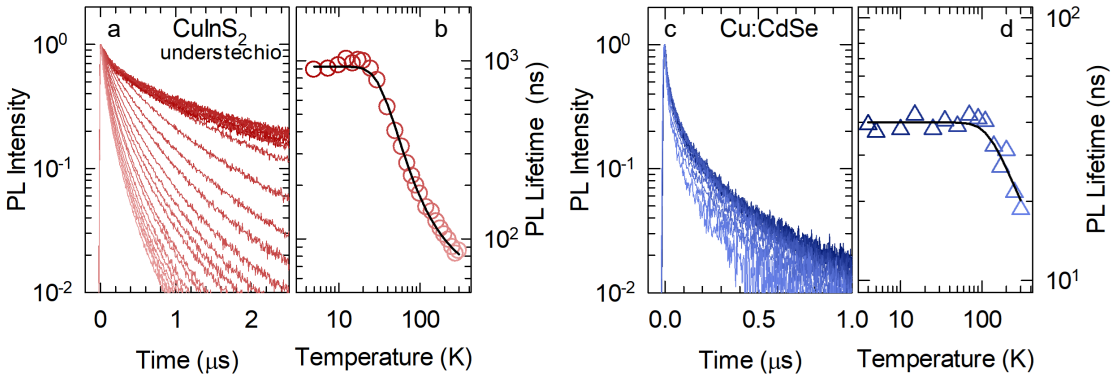

Figure 2.7: *PL decay curves of off-stoichiometry $CuInS_2$ NCs* ***(a)*** *and Cu:doped CdSe NCs* ***(c)*** *(Cu:In=1:4, a=1.0 nm) at decreasing temperature (from 300 K to 4K, grey to black curves). The respective effective PL decay times as a function of temperature are shown in panels* ***(b, d)*** *together with the respective fitting curves to Eq.2.2. The extracted ΔE-values are 30 meV for the Cu:CdSe NCs and 15 meV for the $CuInS_2$ NCs.*

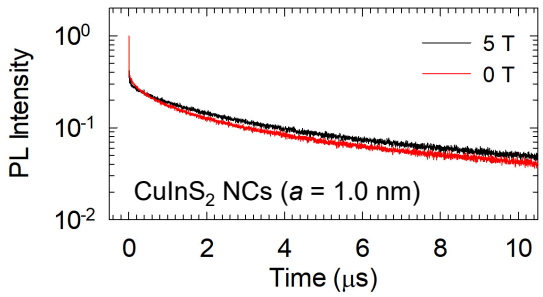

Figure 2.8: *PL decay curves of $CuInS_2$ NCs (a=1.0 nm) at 5 K in the absence (red curve) and in the presence (black curve) of a 5 T magnetic field upon excitation at 3.05 eV.*

dark and bright exciton state Hamiltonians. [56] Consequently, it can be speculated that such an effect might be due to the optically forbidden nature of both the dark and gray excitons in $CuInS_2$ NCs resulting in substantial decrease of the coupling to external magnetic fields.

LSC Performance Optimization Strategies via Monte Carlo Simulations

The agreement between the size dependencies of the spectral and dynamical parameters observed for our $CuInS_2$ NCs with the theoretical predictions by Efros and coworkers [34] provide strong indications that the optical properties of stoichiometric

ternary I–III–VI_2 NCs are due to the detailed structure of the VB. This has important implications for the application of this class of NCs to light management technologies and in particular to LSCs. These devices typically consist of optical waveguides coated or doped with chromophores that absorb sunlight and emit longer wavelength luminescence that propagates by total internal reflection to the device edges, where it is converted to electricity by PV cells installed along the device perimeter. Such an all-optical functioning mechanism makes LSCs particularly suitable for building integrated PV applications spanning from sound barriers [72] to coverages [73] and electrodeless solar windows, [74] and could even help architects in enhancing the aesthetical value of a building. As anticipated above, the realization of efficient LSCs relies of the combination of broadband optical absorption to ensure effective solar harvesting and minimized spectral overlap between the absorption and PL spectra of the chromophores, so as to suppress losses to re-absorption (other critical aspects are the optical quality and transmittance of the waveguide matrix [32] and the type of PV cells [75]).

For building integration and in particular for solar glazing applications, a further key parameter that is directly connected to the spectral coverage is the color of an LSC panel, which determines both the indoor-to-outdoor vision and the quality of the transmitted sunlight illuminating indoor settings. In the case of NCs featuring a continuous optical absorption spectrum, a large SC and a neutral coloring can be achieved by using particles featuring an absorption edge in the near infrared spectral region. [9] However, in the case of the stoichiometric $CuInS_2$ NCs discussed in this chapter, mitigation of quantum confinement in large particles is accompanied by the gradual reduction of Δ_{SS}^{G} , resulting in stronger reabsorption of the propagating PL that is detrimental for the device efficiency. In order to evaluate the impact of such a behavior on the device performance, the experimental results (i.e. the optical absorption and PL spectra) discussed so far were incorporated in a Monte Carlo ray-tracing simulation developed in cooperation with Glass To Power SpA (see the Experimental section). As a result, the LSC performance are evaluated by estimating the number of photons emitted from the waveguide edges, by varying independently the NC sizes and the lateral dimension (L) of a squared LSC.

In Figure 2.9a, are computed the behavior of LSCs featuring the same absorptance below the effective bandgap energy of the respective NCs (corresponding to the peak energy of the 1S bleach in the TT spectra). For small devices (L = 5 cm, 10 cm) where average light propagation distances are relatively short, reabsorption losses play a minor role with respect to solar harvesting, resulting in the monotonic growth of

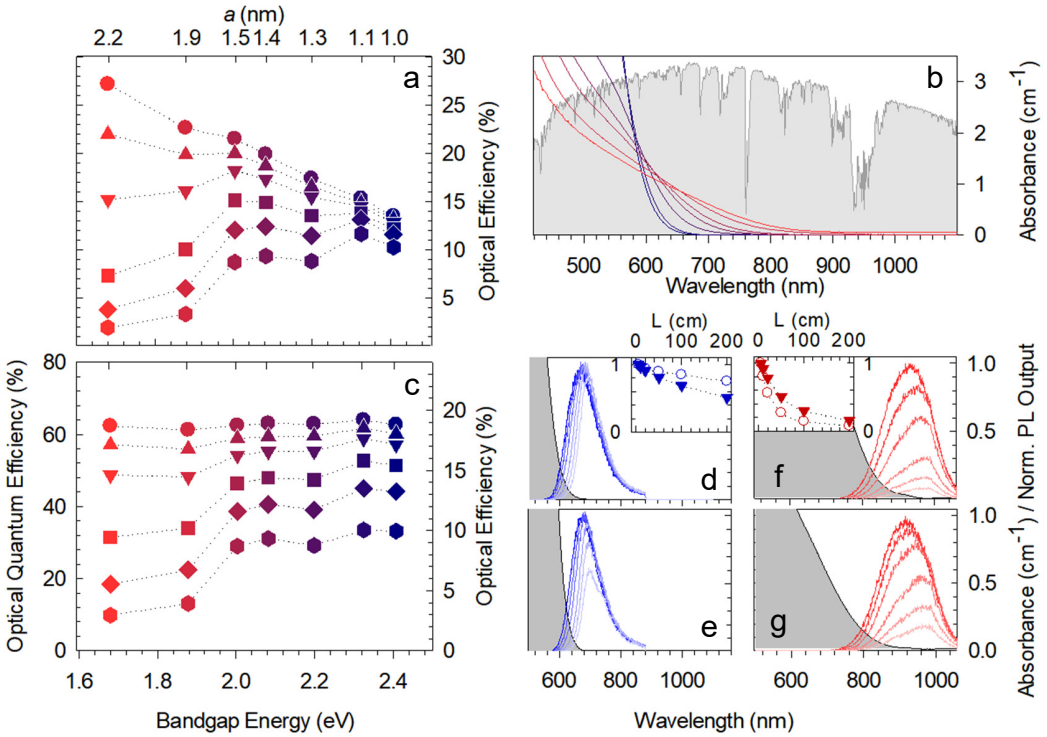

Figure 2.9: ***a)*** *Monte Carlo ray tracing calculation of the optical efficiency (OE) of squared LSCs (thickness 0.5 cm) with increasing lateral size (L), embedding the $CuInS_2$ NCs with different bandgap energy shown in Figure 2.3a. The simulated LSCs feature the same integrated optical absorption below the band-edge of the respective NCs (defined as the peak energy of the 1S bleach in the TT spectra reported in Figure 2.3a).* ***b)*** *Absorption spectra of LSCs based on the same $CuInS_2$ NCs assuming identical spectral coverage of SC=30%. The AM 1.5G solar spectrum (expressed in photons$\times m^{-2} \times s^{-1}$) used for the simulations is reported in grey.* ***c)*** *Calculated optical quantum efficiency O_{QE} and OE as a function of the NC size (i.e. bandgap energy) for LSCs with identical solar coverage (30%) and increasing L.* ***d, f)*** *Edge-emitted PL spectra of NCs with $a = 1.0$ nm (blue lines) and $a = 2.2$ nm (red lines) embedded into LSCs with increasing L featuring the same below gap absorptance. The respective integrated PL intensities are shown respectively as blue and red circles in the insets of panel 'd' and 'f'.* ***e, g)*** *Edge-emitted PL spectra of the same LSCs in the case of equal spectral coverage, SC = 30%. The respective integrated PL intensities are shown as blue and red triangles in the insets of panel 'd' and 'f'.*

the optical efficiency (*OE*, evaluated as the number of edge-emitted photons divided by the number of solar photons impinging on the device surface) with increasing NC size, reaching $OE > 20\%$ for L = 10 cm, despite a relatively low solar coverage (SC $<$ 40%). For larger L-values, reabsorption becomes the dominant parameter, gradually lowering the *OE* for LSCs embedding large NCs. Importantly, an optimum is found for large LSCs (L = 0.5 m) embedding NCs with $a = 1.5$ nm showing *OE* as high as 15%. Notably, nearly constant $OE > 10\%$ versus a is calculated also for devices

with 1 m^2 size, which would be particularly adapt for architectural integration. It is worth noting that the use of NCs with $a \geq 1.4$ nm has the key advantage of enabling the fabrication of LSC devices of neutral color, whose integration into glazing systems would introduce negligible distortion of the transmitted solar spectrum.

To simulate a more realistic and applicative scenario, depending on the NC size (i.e. the spectral position of the absorption edge) the NC loading in the LSC is varied in order to obtain devices featuring the same solar harvesting capability. Consistent with the smaller bandgap and steeper low-energy absorption tail of small NCs ($a < 1.3$ nm) — due to negligible oscillator strength of the optical transition coupling the odd parity VB sublevel and the CB with respect to larger particles — the desired SC is achieved with LSCs featuring a high NC loading, resulting in a sharp absorption edge at ∼580 nm.The respective absorption spectra are shown in Figure 2.9b together with the AM 1.5G solar spectrum used for the simulations (expressed in photons$\times m^{-2} \times s^{-1}$). Upon increasing a, progressively lower NC contents are required for the same SC and the resulting absorption spectrum is gradually more uniform across the visible/near-IR region. As a consequence, for LSCs featuring the same spectral coverage, reabsorption losses are enhanced (reduced) in LSCs with small (large) particles than in the example discussed in Figure 2.9a that compared devices with equal absorptance at the bandgap of the respective NC emitters. This is testified by the OE (and O_{QE}) trend of LSCs with increasing L in Figure 2.9c. Specifically, the spread of the OE values versus L is narrower (larger) for $a = 2.2$ nm ($a = 1.0$ nm) in Figure 2.9a, which is consistent with the corresponding trends of the integrated PL output with the LSC dimension reported in the insets of Figure 2.9d and 2.9f, showing opposite behavior for the two different NC sizes. Most importantly, Figure 2.9c indicates that, despite the significant transparency of 70%, OE as high as 12% could be achieved for large colorless LSCs (L = 1 m) embedding NCs with $a = 1.5$ nm and that increasing the device area to 4 m^2 would still yield efficiencies close to 10%.

Large-Area LSC Prototype Characterization

Finally, to experimentally validate the design guidelines for efficient LSCs obtained from the Monte Carlo simulations, the team has fabricated a prototype large-area semitransparent LSC devices (30 cm × 30 cm × 0.7 cm, 60% absorptance in the 400–750 nm spectral range) that utilize stoichiometric $CuInS_2$ NCs. Based on the outcome of the theoretical modeling, NCs with size $a \sim 1.5$ nm have been chosen, as they present the best tradeoff between broadband SC and suppressed reabsorption capability. Prior to

encapsulation, the NCs were shelled with a 1 nm thick ZnS layer to protect their surfaces from the radical initiators used for the production of the poly(methyl methacrylate) (PMMA) waveguide. In agreement with previous reports, shelling substantially enhanced Φ_{PL} from 30 ± 5% to 85 ± 5% without modifying the spectral properties of the NCs. [24, 63, 76] The choice of PMMA as the waveguide material is dictated by its excellent optical properties, [32] high resistance to exposure to UV light, and various chemical treatments, as well as excellent performance in all-weather conditions. Figure 2.10a shows a photograph of the fabricated LSC containing 0.05 wt% of NCs under ambient illumination featuring the characteristic neutral brownish coloring well suited for architectural integration. [9, 10]

The optical absorption and PL spectra of the NCs in toluene solution and embedded into the PMMA waveguide are reported in Figure 2.10b, showing virtually identical spectral properties for the two samples (except for the absorption peak at 900 nm due to the vibrational overtone of the C–H stretching mode of the polymer). In agreement with previous reports, [9] side-by-side PL efficiency measurements show that Φ_{PL} of the pristine NCs is nearly completely preserved in the nanocomposite ($\Phi_{PL}^{PMMA} = 80 \pm 5\%$). The substantial absence of light scattering from the polymeric slab is confirmed by PL measurements in an integrating sphere on the same nanocomposite sample (3 cm × 3 cm) with either clear or blackened edges, so as to distinguish between the light emitted from the LSC faces and the guided PL emitted from the slab edges. The PL data reported in Figure 2.10c show that the emission from the LSC edges corresponds to ∼76% of the total emission intensity, which closely matches the maximum theoretical value of light-trapping efficiency for a PMMA waveguide (∼74.1% considering a refractive index of the polymer matrix n = 1.49) defined by Snell's law.

Having assessed the optical quality of the waveguide, the performances of the prototype are quantified by measuring the *OE*, the O_{QE} and the optical power efficiency (OPE), defined as the ratio between the optical power emitted by the LSC and the incident solar power. For these measurements, we index-matched the perimeter edges (A_{edge} = 120 cm × 0.7 cm = 84 cm^2) of the LSC shown in Figure 2.10a to calibrated c-Si solar cells and exposed the LSC to outdoors illumination perpendicular to its top surface (A_{LSC} = 30 cm × 30 cm = 900 cm^2) and used a calibrated photodiode to instantaneously monitor the solar irradiance impinging onto the LSC top surface. No reflector or back diffuser was placed at the bottom of the waveguide. Based on these measurements, we obtained an OPE = 6.8 ± 0.2%, which is the highest optical power efficiency reported to date for a large area LSC. The corresponding O_{QE}-value is 29.2%, corresponding to *OE* = 7.4%. The effective mitigation of reabsorption losses us-

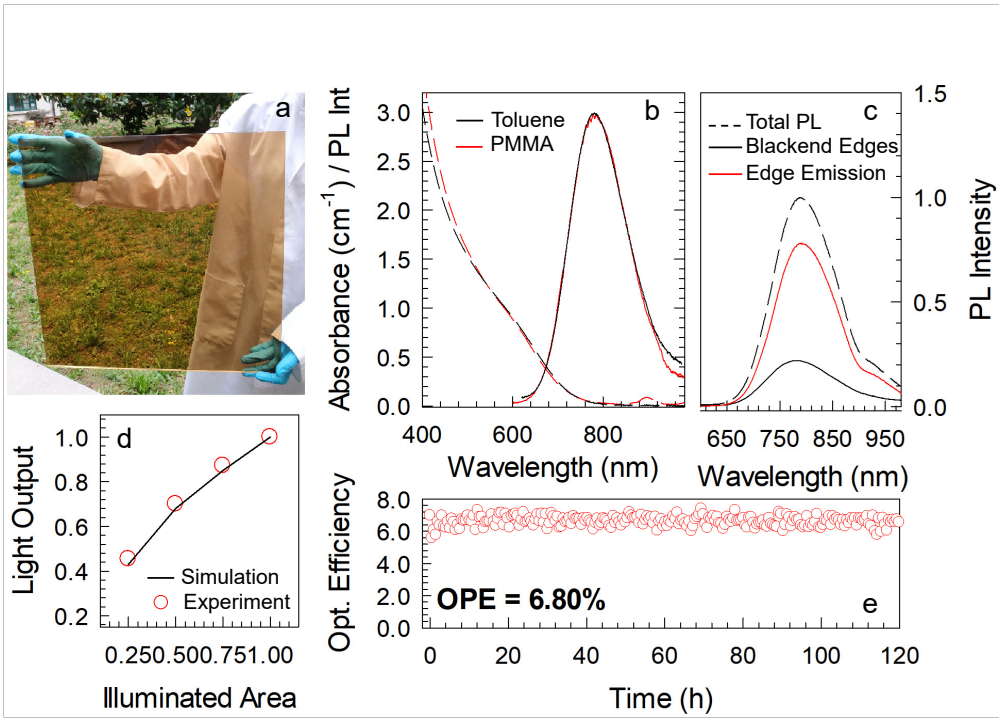

Figure 2.10: ***a)*** *Photograph under daylight of an NC:PMMA (NCs embedded in PMMA) nanocomposite waveguide (400–750 nm transparency ∼40%, dimensions: 30 cm × 30 cm × 0.7 cm).* ***b)*** *Optical absorption (dashed lines) and PL (continuous lines) spectra of ZnS-capped CuInS2 NCs (a = 1.5 nm) in toluene solution (black curves) and embedded into a PMMA nanocomposite (red curves, NC concentration of 0.05 wt%).* ***c)*** *PL spectra of a portion (3 cm × 3 cm) of the same LSC with the edges clear (total PL, black dashed line) and blocked by black paint (solid black line, corresponding to light emitted from the slab surface). The red line is the difference between the total PL and the surface emission and corresponds to the PL emitted from the waveguide edges.* ***d)*** *Relative optical output power measured from c-Si PVs coupled to one perimeter edge of the LSC as a function of the device area illuminated by a calibrated solar simulator (1.5 AM Global, circles). The theoretical trend obtained through Monte Carlo ray-tracing simulation of an ideal LSC with no scattering or reabsorption losses is reported as a black curve.* ***e)*** *Stability test under stress conditions: artificial sunlight illumination (∼1 Sun); temperature of 55 °C. Point-to-point fluctuations in the OPE-values are due to oscillation in the intensity of excitation light.*

ing $CuInS_2$ NCs with a = 1.5 nm, together with the absence of scattering losses, results in the nearly ideal behavior of the LSC. [77] This is highlighted in Figure 2.10d, where is shown the light output emitted from one of the device edges (30 × 0.7 cm^2) measured using the same setup adopted for the *OE* measurements (with only one slab edge coupled to the photodiodes and no back-reflector), but progressively exposing increasingly larger portions of the LSC area to the solar simulator. The same figure also reports the expected trend calculated using Monte Carlo ray-tracing simulation for an ideal scattering- and reabsorptionfree device of identical dimensions embedded with emitters

of the same Φ_{PL} as the used NCs, in which the light output is determined exclusively by the numeric aperture of the illuminated device area. The experimental data are in very good agreement with the simulated trend, which supports the ascription that the LSC is close to an ideal device. Finally, accelerated aging test assess the stability of the stoichiometric $CuInS_2$ NCs and polymer waveguide in working conditions exposing the LSC to continuous illumination with solar light at 55 °C. Remarkably, as shown in Figure 2.10e, the OPE of the LSC remains constant for over 120 h of continuous operation, thus further supporting the technological potential of stoichiometric $CuInS_2$ NCs in real-world applications.

2.2.4 Conclusions

To summarize, through the combination of optical and magneto-optical experiments on stoichiometric $CuInS_2$ NCs as a function of size and temperature I have revealed, for the first time, the spectroscopic signatures predicted for the excitonic photophysics of I–III–VI_2 NCs. In agreement with effective mass calculations, measurements show quadratic dependence of the global Stokes shift and the radiative decay rate on the particle size, thus strongly supporting the theory by Efros and coworkers. [34] The absence of intragap defect states is consistent with magnetic circular dichroism experiments showing temperature independent MCD perfectly reproduced by the linear Zeeman splitting function. Time-resolved PL measurements performed below 50 K further reveal the dynamic signature of emission originating from a lower-lying dark-like exciton which are not found in Cu:doped CdSe NCs or off-stoichiometry $CuInS_2$ NCs. The splitting energy separating such a state from a gray exciton follows a linear trend with the inverse of particle volume as commonly observed in undoped II–VI chalcogenide NCs, suggesting that also in I–III–VI_2 NCs such a behavior originates from enhanced electron–hole spin interaction.

We then evaluated the impact of the observed size dependence of the Stokes shift in stoichiometric $CuInS_2$ NCs on their suitability to LSCs, where I–III–VI_2 NCs are considered among the most promising candidates for high performance devices. Monte Carlo ray-tracing simulations provided rational guidelines enabling to decouple the beneficial effect of progressively wider solar harvesting efficiency with increasing particle size from the concomitant detrimental increase of reabsorption losses in large area devices and thereby to suggest compromise optimization strategies to realize efficient LSCs with size and aesthetics compatible with building integrated PV applications. Based on such theoretical guidelines, a large-area LSC device was fabricated in collab-

oration with Glass To Power Spa by embedding stoichiometric $CuInS_2$ NCs into mass polymerized PMMA waveguides. Thorough characterization of such a device revealed optical grade quality of the matrix and efficient NC emission, leading to an OPE as high as 6.8%, corresponding to the highest value reported to date for large-area LSC devices.

2.3 Intrinsic and Extrinsic Exciton Recombination Pathways in $AgInS_2$ Colloidal Nanocrystals

In this section, I will extend the fundamental photophysical knowledge of stoichiometric $CuInS_2$ NCs to $AgInS_2$ NCs. Despite their comparably promising optical properties, $AgInS_2$ NCs have been much less investigated than $CuInS_2$ NCs [78–81]. Recently, building upon the theoretical description of the VB structure of $CuInS_2$ NCs by Efros and co-workers [34], Baimuratov et al. [82] theoretically investigated the origin of the optical behavior of $AgInS_2$ NCs also by taking into account the contribution of electron-phonon coupling and the additional effect of point defects. To date, however, detailed experimental studies of the photophysical mechanisms in $AgInS_2$ NCs have not yet been reports and thus the understanding of this important class of NCs lags behind that of their copper-based analogues. In this section, I aim to contribute to this task by investigating the optical properties of $AgInS_2$ NCs using complementary spectroscopic techniques including continuous wave (cw) and time-resolved photoluminescence (PL), spectro-electrochemistry (SEC), ultra-fast transient transmission (TT), and magnetic circular dichroism (MCD) experiments. Optical absorption and TT measurements enable to resolve two spectral contributions responsible for the broadband absorption profile, while photoluminescence excitation (PLE) measurements reveal that the Stokes-shifted PL can also be excited using resonant excitation as much as 550 meV below the dominant absorption edge. This suggests that, similar to $CuInS_2$ NCs, the PL derives from an optical transition coupling the CB minimum to an odd-parity VB sublevel where the photohole thermalizes. TT dynamics enable us to quantify the hole localization time (1.4 ps), and temperature-controlled MCD measurements corroborate the absence of paramagnetic intragap states involved in the Stokes-shifted PL of ternary I-III-VI_2 chalcogenides NCs. In order to identify the main non-radiative pathways affecting the PL quantum efficiency of our NCs – in view of their application as active materials in optoelectronic devices – I perform spectro-electrochemistry measurements and PL experiments as a function of temperature. The PL behavior under applied electrochemical potential reveals that thermally-assisted surface electron trapping is the main nonradiative loss channel, whose suppression via electrochemical passivation of electron traps or by lowering the sample temperature to 3.5 K leads to PL quantum efficiency close to unity. Interestingly, consistent with recent results on defect-free $CuInS_2$ NCs [83], the PL dynamics below $T{\sim}50$ K show an almost 100-fold slowing down, at constant PL quantum yield (Φ_{PL}), thus pointing to a further fine structure

of the emissive band-edge exciton state composed of the CB electron and the hole in the odd-parity VB sublevel. Crucially, side-by-side time-resolved PL measurements on Ag:doped CdSe NCs, where the photohole rapidly localizes in the Ag-dopant site, show exclusively the increase of the PL lifetime with decreasing temperature due to gradual suppression of thermally-assisted nonradiative decay and no fine structure effects. This indirectly corroborates the picture that in ternary $AgInS_2$ NCs the peculiar low-temperature PL kinetics is associated to the fine structure of the lowest excitonic level with either carriers in the respective quantized band-edge states.

2.3.1 Samples Description

For the synthesis of $AgInS_2$ NCs was followed a heat-up procedure using the method proposed by Torimoto and co-workers [84]. A precursor ratio of 1:1 In:Cu - Ag(OAc) (0.2 mmol), $In(OAc)_3$ (0.2 mmol) - was loaded into a three-neck flask with thiourea (0.2mmol), 3 mL oleylamine (OLA), and 2 mL of 1-dodecanethiol (DDT) and was degassed under vacuum at 110 °C for 1 hour. Then, under nitrogen flow, the temperature was raised to 230 °C for 15 minutes to let the particles grow. Finally, the reaction was quenched by cooling the solution to room temperature. The NCs were cleaned by precipitation with methanol and redispersion in hexane. Using such a precursor ratio, were obtained stoichiometric $AgInS_2$ NCs with In:Ag:S ratios of to 1.06:1:2.04, as confirmed by elemental analysis by inductively coupled plasma atomic emission spectroscopy (ICP-AES). The obtained NCs were of tetragonal crystal structure with radius distribution of 2.3±0.4 nm (Figure 2.11).

The synthesis of Ag-doped CdSe NCs (Ag:CdSe) has been carried out with the kind collaboration of the group of Prof. Jiatao Zhang from Beijing Institute of Technology (China). Ag nanoparticles (NPs) as described by Liu et al. [85] were used as seeds for the 3% Ag:CdSe synthesis. Monodisperse Ag NPs (∼5 nm) were first prepared and reacted with a Se precursor in the molar ratio 1:5 at 50°C for the preparation of amorphous Ag_2Se NPs. The Se precursor was prepared from 1 mmol Se powder with 7 ml octadecylene at 270°C. The obtained Ag_2Se NCs (0.035 mmol) were dispersed in 10 ml toluene with 0.2 ml oleic acid (OA) and 0.1 ml oleylamine (OAm), then a 1 ml methanol solution containing 0.1 g $Cd(NO_3)_2{\cdot}4H_2O$ was added. After 2 min magnetic stirring, 0.1 ml tributylphosphine (TBP) was added, and the mixture was heated at 55°C for 1 h under magnetic stirring. The doping level was estimated by XPS analysis as described in Ref. [37].

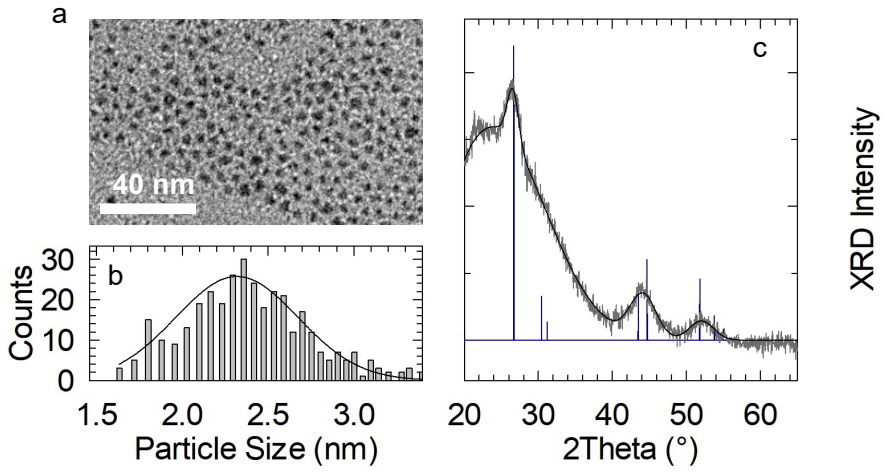

Figure 2.11: ***a)*** *TEM overview image of $AgInS_2$ NC sample featuring mean radius 2.3±0.4 nm.* ***b)*** *$AgInS_2$ NC size distribution extracted from 'a' and presented as the radius of the disc with the same projected area as the NC.* ***c)*** *X-ray diffraction pattern of $AgInS_2$ NCs at room temperature.*

2.3.2 Experimental Details

Spectroscopic Studies

Optical absorption and PL measurements are carried using the experimental setup described in Section 2.2.2 (transient PL measurements have a time resolution of ∼400 ps). Photoluminescence quantum yield measurements were performed in an integrating sphere on NCs deposited onto silica substrates using the same excitation source and detection setup. The same films were mounted in the variable temperature insert of a closed cycle He cryostat for monitoring the dependence of the emission yield with temperature. Temperature dependent PL and trPL measurements were carried out on NC thin films drop-casted on quartz substrates, excited using a frequency tripled pulsed Nd:YAG laser at 3.49 eV with a 150 Hz repetition rate (pulse duration, 5 ns), and mounted inside a cryostat with optical access.

Ultrafast Transient Transmission (TT) and Magnetic Circular Dichroism (MCD) measurements are carried out with the same experimental setup described in Section 2.2.2

Spectro-Electrochemistry Study

ITO-coated glass slides (50 × 7 × 0.7 mm, $R_S < 100\ \Omega$) were purchased from Delta Technologies (part no. CG-90IN-CUV). The ITO-coated surface was first covered with ZnO NPs (Nanograde, ∼50 nm diameter) to avoid quenching of NC emission by fast charge/energy transfer to the ITO. The ZnO NP layer (∼60 nm thick, measured using a Dektak profilometer) was deposited by dip-coating the glass/ITO substrate into an ethanol suspension of ZnO NPs (2 mg ml^{-1}, one dip for 10 s) and annealed at 150 °C for 10 min in a nitrogen glovebox. To test the stability of the glass/ITO/ZnO NP substrates during potential scans, control experiments were performed in which I monitored changes in optical absorption spectra for prolonged exposures to negative and positive potentials. The results of these measurements indicate that the substrates are unaffected by either positive or negative EC potentials for exposure times of tens of minutes, which are much longer than the measurement time used in SEC experiments (∼10 min). The NCs were deposited onto the ZnO NP layer as a few-monolayer-thick film by dip-coating from a dilute toluene solution. The ZnO NP layer used in this study was not treated with crosslinkers and therefore it represented a dielectric tunneling barrier of ∼1 V. The introduction of the additional ZnO spacer as well as the presence of insulating surface ligands can also lead to an appreciable attenuation of the actual shift of the FL compared to the nominal applied EC potential. The ITO was connected as a working electrode to the potentiostat (Bio Logic SP-200 Research grade potentiostat/galvanostat) and the film was placed into a quartz cuvette filled with the electrolyte (0.1 M tetrabutylammonium perchlorate ($TBAClO_4$) in propylene carbonate). Ag and Pt wires were used as pseudoreference and counter electrodes, respectively. All potentials reported in this section are measured relative to the quasi-reference Ag electrode during staircase voltammetry scans (10 s per scan). The film was excited at 3.06 eV with a ps-pulsed-wave diode laser and the emitted light was collected with a focusing lens and detected with a charge-coupled device spectrometer.

2.3.3 Results

Optical Absorption and Photoluminescence data

The optical absorption spectrum of the NCs in toluene (Figure 2.12a) shows the characteristic broadband profile of I-III-VI_2 NCs with an absorption shoulder at ∼2.25 eV and a low-energy tail extending into the PL peak. The broad (FWHM ∼0.3 eV) PL spectrum is centered at 1.64 eV corresponding to a Stokes shift as large as ∼650 meV

from the absorption shoulder. The Φ_{PL} at room temperature is 40±5%. Consistent with previous reports [79], the corresponding PL dynamics (Figure 2.12b) are nearly single-exponential – except for a slightly faster initial drop possibly due to charge trapping – with lifetime τ = 820 ns (as extracted from single exponential fitting of the dominant PL decay excluding the initial fast drop). Interestingly, the PLE spectrum collected at the PL maximum resembles nearly perfectly the low-energy absorption tail, and the respective PL spectra excited at progressively lower energy (Figure 2.12c) show no significant difference in shape or energy position with respect to each other or in comparison with the PL spectrum excited well above the absorption shoulder at 3.1 eV. The constant PL linewidth suggests that the exciton thermalizes to the same state below the dominant absorption shoulder, independently from the excitation energy.

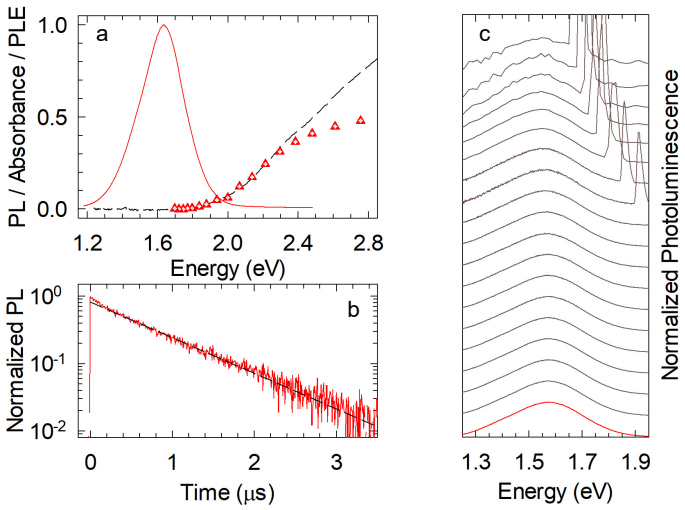

Figure 2.12: ***a)*** *Optical absorption (black dashed line), PL (solid red line) and PLE (triangles) spectra for a colloidal NC solution in toluene. PL excited with a 405 nm (3.06 eV) pulsed diode laser at 20 MHz. PLE obtained for PL maximum at 1.64 eV by varying excitation from 3.06 eV to 1.7 eV.* ***b)*** *Normalized PL decay at PL maximum at 1.64 eV using 3.06 eV pulsed excitation.* ***c)*** *PL spectra of the same NCs under progressively lower energy excitation (from bottom to top corresponding to the PLE data in panel 'a').*

Spectrally Selective Ultra-fast Transient Transmission Spectroscopy

More detailed insights into the structure of the absorption spectrum and the carrier dynamics are obtained by ultra-fast *TT* spectroscopy using a spectrally selective pump operating in the low-fluence regime (when the number of photons absorbed per NC per pulse is much less than unity). Upon pumping above the absorption shoulder at 2.3

eV (Figure 2.13a), the differential transmittance ($\Delta T/T$) spectrum exhibits two intense bleaching bands at ∼2.25 eV and ∼2.05 eV (indicated as "A" and "B") in good correspondence with the absorption shoulder and with the low-energy tail of the steady-state absorption profile, respectively. The inspection of TT fast dynamics in Figure 2.13b shows an almost instantaneous photobleaching of the A transition – comparable with the temporal resolution of the experimental setup (∼100 fs) – while the B signal grows more slowly with a rise time of 1.4 ps. These results support the VB structure model with the A band corresponding to the parity-allowed optical transition coupling the even-parity VB sublevel and the CB minimum, which also features an even-parity symmetry. On the other hand, the B band is associated with a lower-energy transition coupling the odd-parity VB sublevel and the CB. This transition exhibits small oscillator strength due to the parity selection rules. The slow photobleaching risetime observed for the B signal (Figure 2.13b) is related to hole dynamics; in particular, pumping above the absorption shoulder, it describes thermalization of the photohole from the higher-lying even-parity hole sublevel to the odd-parity sublevel. Following this picture, pumping directly within the B bleaching band should not change the TT spectrum since promoting electrons from the odd states into the CB inhibits also the A band transition. Furthermore, direct excitation of odd VB sublevel would result in an instantaneous bleaching also for the B signal. To explore this scenario, I selectively pump at 1.97 eV, far below the absorption shoulder. The resulting $\Delta T/T$ spectrum is nearly unchanged showing both A and B bands (Figure 2.13c), while bleaching dynamics are now also instantaneous for the B signal (Figure 2.13d). As a result, the overall TT analysis corroborates the VB structure model showing two transitions separated in energy by ∼0.2 eV that are ascribe to odd- and even-parity VB sublevels, and reveals an efficient photohole thermalization process occurring at the picosecond timescale.

I point out that similar TT dynamics have been observed [43] for Ag:CdSe NCs where silver atoms undergo a transient photo-oxidation from the nonmagnetic Ag^+ ($[Kr]4d^10$) configuration to Ag^{2+} ($[Kr]4d^9$) which behaves as a paramagnetic radiative acceptor centre for a CB electron. Crucially, the unpaired spin of the lone electron in the d-shell of Ag^{2+} couples strongly with the band-edge exciton, resulting in the characteristic non-linear temperature and magnetic field MCD dependence due to sp-d exchange interactions [64]. Therefore, magneto-optical experiments can be used to corroborate the absence (or reveal the presence) of intragap metastable Ag^{2+}-like acceptor states also in our $AgInS_2$ NCs. In Figure 2.13f are reported the MCD spectra at increasing temperature from 2.5 K to 20 K at constant magnetic field (H = 6 T). Importantly, opposite to what observed in Ag:CdSe NCs, the magnetic response

of our stoichiometric $AgInS_2$ NCs is temperature independent, same as what found in stoichiometric $CuInS_2$ NCs [83]. To further investigate this aspect, the evolution of the Zeeman splitting energy (ΔE_Z) were extracted at 2.5 K when continuously increasing H from 0 to 6 T in Figure 2.13g. In agreement with Figure 2.13f, ΔE_Z grows linearly with H as a result of the sole intrinsic Landé factor of the NCs exciton showing no further sp–d exchange interaction between the semiconductor bands and Ag^{2+} lone spins. Accordingly, these data are well fitted by the linear Zeeman splitting function $\Delta E_Z = \mu_B H g_{ex}$, where μ_B is the Bohr magneton, and g_{ex} is the Landé factor for the exciton with total angular momentum F = 1 responsible for optical absorption. The obtained g-factor gex ∼0.5 is similar to previous results for $CuInS_2$ NCs (gex = 0.22). Therefore, my experimental results support a scenario in which the broad absorption profile is dominated by parity selection rules, while the long-lived PL arises from the parity-forbidden recombination of the 1Se electron into the odd-parity VB state activated by photohole localization. Within this framework, and in accordance with theoretical predictions [82], strong electron-phonon coupling could be responsible for the homogenously-broadened PL spectrum shape in $AgInS_2$ NCs [86], as previously reported in single-particle PL measurements [87–89] (FWHM ∼0.2-0.35 eV). Consistent with Kruchinin's calculations, electron-phonon coupling also accounts for the additional ∼250 meV spectral separation between absorption shoulder and PL peak, leading, together to the ∼200 meV separation due to the odd- even-parity VB effect to the observed ∼450 meV Stokes shift.

Spectro-electrochemical investigation of nonradiative loss channels

With a view to optimize these NCs for optoelectronic applications, I conducted SEC experiments to obtain a picture of the principal loss channels. Electrochemical measurements are performed as cyclic staircase voltammetry for negative and positive electrochemical potentials (V_{EC}) against a silver-wire pseudoreference electrode. These measurements can be interpreted in terms of a deliberate modulation of the Fermi level (FL) where negative (positive) V_{EC} is equivalent to raising (lowering) the FL, resulting in a reversible passivation (activation) of surface electron traps associated with under-coordinated surface atoms or dangling bonds [43].

In Figure 2.14a is shown the complete set of PL spectra for $AgInS_2$ NCs under application of negative V_{EC} cyclically scanned between 0 and -2.4 V. Notably, the PL maximum exhibits a 0.18 eV red-shift after drop-casting on indium tin oxide (ITO)/ZnO substrate, ascribable to energy transfer processes in aggregated NCs films as previ-

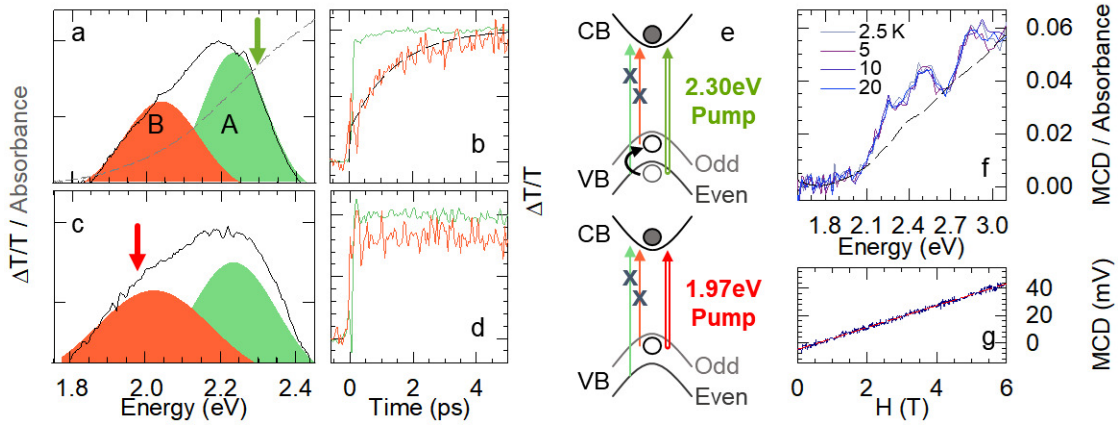

Figure 2.13: ***a)*** *Normalized transient transmission spectrum of $AgInS_2$ NCs collected at 5 ps after pumping at 2.3 eV in low fluence regime highlighting the A and B transitions, depicted here as shaded areas. Steady-state absorption spectrum for the same toluene solution of NCs used in TT measurements is reported as gray dashed line. The short green arrow shows the pumping energy.* ***b)*** *Normalized bleaching $\Delta T/T$ kinetics for the A transition at 2.25 eV (green line) and for the B band at 1.9 eV (red line) after pumping close to the band-edge at 2.3 eV to avoid thermalization effects. The dashed line is a fit to an exponential rise function with 1.4 ps characteristic time.* ***c,d)*** *Same as 'a' and 'b', but for pumping within the B transition band at 1.97 eV. A short red arrow shows the pumping energy.* ***e)*** *Schematic diagram of the photophysical mechanism occurring at different pumping energies: slightly above the absorption shoulder at 2.3 eV (top panel) and within the B transition at 1.97 eV (bottom panel). Crossed thin vertical lines emphasise transition bleaching after the pump event. f) MCD spectra at 6 T, at different temperatures (T = 2.5, 5, 10, 20 K). The dashed line is the absorption spectrum for the polymeric slab containing $AgInS_2$ NCs used in MCD measurements.* ***g)*** *Zeeman splitting (ΔE_Z) versus magnetic field collected at 2.5 K showing linear trend (R^2 = 0.996).*

ously reported in core-shell $CuInS_2$/ZnS NCs [90]. To quantify the effect of raising the FL on the PL intensity, the integrated PL intensity are plotted as a function of the applied potential (Figure 2.14b), showing almost no effects at the initial stage of the potential ramp (up to V_{EC} = -1.2 V). This effect is common in SEC experiments using ITO/ZnO substrates, where the ZnO layer represents a dielectric tunnelling barrier resulting in a voltage drop across it [91]. By lowering the working electrode potential, the PL intensity undergoes a sudden growth by ∼120% at -2.25 V. At even more negative potentials, the PL exhibits a reversible intensity drop likely associated with direct electron injection in the CB resulting in the activation of non-radiative Auger recombination [43, 92]. The PL evolution has been monitored during several cycles showing good reproducibility and symmetry by lowering and raising the applied potential, thus indicating that the voltage sweep does not damages the NC surfaces and that the passivation and activation of surface traps occur with similar time kinetics. On the other

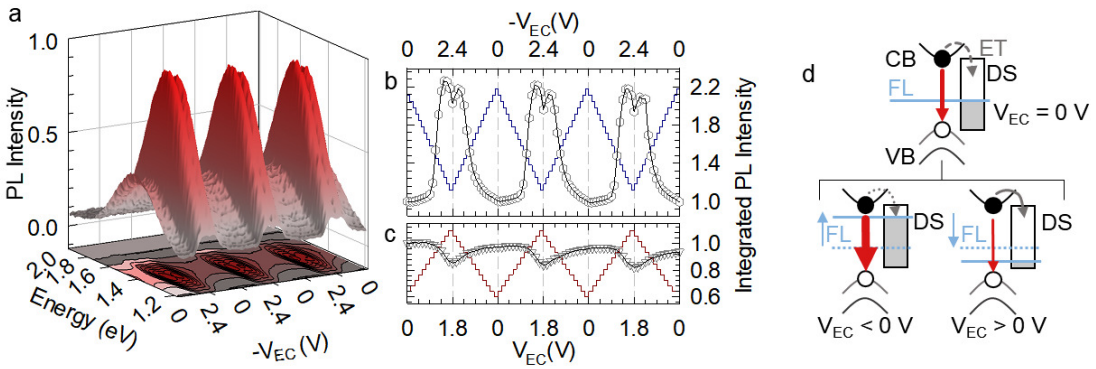

Figure 2.14: ***a)*** *Normalized PL spectra for $AgInS_2$ NCs at room temperature obtained during three cycles of staircase voltammetry with negative V_{EC} potential: lowered from 0 to -2.4 V and then back to 0 V against Ag-wire pseudoreference (150 mV steps, each lasting 10 s).* ***b)*** *Spectrally integrated and normalized PL intensity as a function of V_{EC} extracted from 'a'. The applied V_{EC} is reported in background as blue vertical step line.* ***c)*** *Same as 'b' for positive V_{EC} potential increasing from 0 to +1.8 V and then back to 0 V.* ***d)*** *Schematic of the radiative recombination pathway (red arrow) and the competing nonradiative carrier trapping processes to defect states (DS) shown as gray arrows. The effect of the EC potential on PL intensity depends on the filling/emptying of DS (right of the band diagram) in response to changes in the position of the Fermi Level (FL) represented as a blue line.*

hand, by lowering the FL (Figure 2.14c), can be observed a slight PL dimming (∼15%) at 1.8 V that almost completely recovers when returning to $V_{EC} = 0$ V. The overall SEC behavior – illustrated in Figure 2.14d – suggests that surface electron trapping (ET) is the dominant loss channel with respect to competitive surface hole trapping, and that its suppression would ultimately lead to Φ_{PL} close to unity. Similar suppression of electron trapping can be achieved growing a large bandgap shell; however, the use of zinc chalcogenides is typically accompanied by Zn diffusion into the NC core which modifies the electronic structure of the material. Hence, a defect-mediated radiative recombination is commonly invoked in alloyed $AgInS_2$/ZnS NCs to model their optical behavior, where the defect's nature and position within the NC volume determine the PL energy and decay rate [93].

Temperature-Dependent and Time-Resolved Photoluminescence

Complementary indications about loss channels in $AgInS_2$ NCs come from temperature-dependent steady state and time-resolved PL experiments. In Figure 2.15a, is reported a set of representative PL spectra at different temperatures in the range from T = 300 K to T = 3.5 K for $AgInS_2$ NCs showing monotonic growth of the PL intensity with decreasing T, saturating at Φ_{PL} ∼100% below 50K (Figure 2.15b) and followed

by a slight drop possibly due to non-radiative competitive channels which become competitive with the dark-exciton emission at low T. Nearly 100% PL efficiency indicates essentially complete suppression of thermally activated nonemissive channels, and that the system has reached its radiative regime. The relative Φ_{PL} increase at cryogenic temperatures is consistent with SEC experiments at negative potentials, suggesting that electron trapping at the NC surface is phonon-assisted. By fitting the integrated PL intensity evolution with T to the function [86,94] $I_{PL}(T) = c/(1 + q * exp(-E_a/k_BT))$ where c is a scaling factor, k_B is the Boltzmann constant and q is a fitting parameter acting as a weight for the probability of this process, is obtained the trapping activation energy E_a ~29 meV, similarly to previous reports [83].

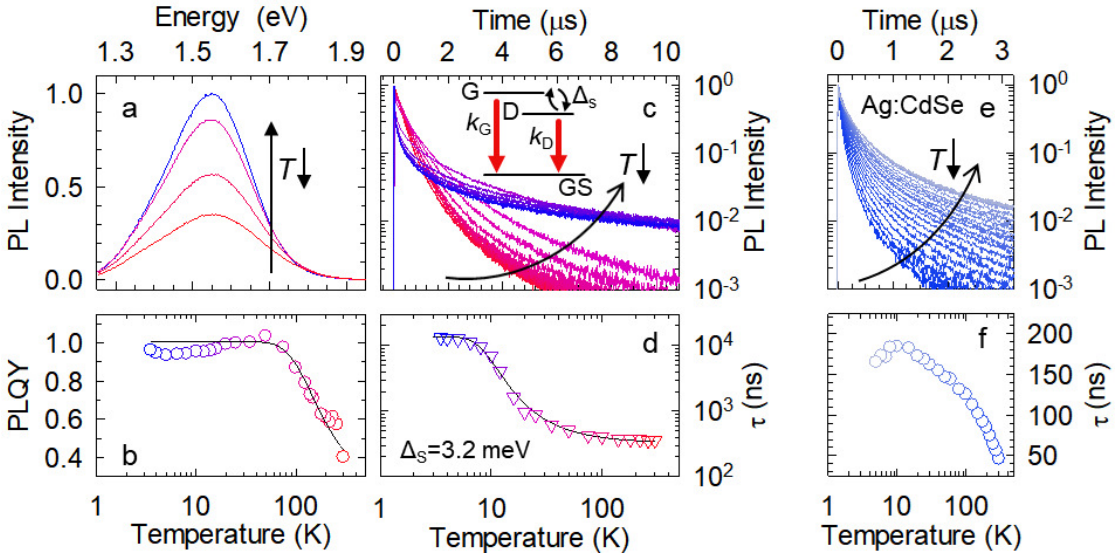

Figure 2.15: ***a)*** *Representative set of PL spectra of $AgInS_2$ NCs under pulsed laser excitation at 3.5 eV (355 nm) with 150 Hz repetition rate progressively lowering temperature from 300 K to 3.5 K (from red to gray).* ***b)*** *Spectrally integrated and normalized PL intensity from (a) and corresponding Φ_{PL}. The solid black line represents the fit with the equation described along with the text ($R^2 = 0.989$).* ***c)*** *Decay curves for PL maximum at decreasing temperature from 300 to 3.5 K under 3.5 eV (355 nm) excitation at 150 Hz repetition rate. Inset: three-level model of gray (G) and dark (D) exciton states separated in energy by Δ_S.* ***d)*** *PL decay lifetimes extracted from 'c' as a function of temperature together with the respective fit (black line) to Eq. 2.2.* ***e)*** *PL decay curves for Ag:CdSe NCs at decreasing temperature from 300 K to 4 K (from blue to gray) collected at Ag-related PL maximum (1.69 eV) under pulsed laser excitation at 3.5 eV (355 nm) with 500 Hz repetition rate. f) PL decay lifetimes extracted from 'e' as a function of temperature.*

To further investigate temperature assisted losses, I perform time-resolved PL measurements, as a function of T, showing gradual lengthening of the PL dynamics with decreasing T(Figure 2.15c). We notice that for $T >$ 50 K, the zero-delay PL inten-

sifies with no significant variation of τ by cooling down the system before reaching Φ_{PL} maximum at 50 K: this behavior is largely due to suppression of ultrafast charge trapping channels depleting the NC bands faster than instrumental temporal resolution. Strikingly, by lowering the temperature below 50 K, PL kinetics slows down dramatically and becomes double-exponential with an initial fast portion followed by a tens-of-microseconds long component, nearly two orders of magnitude slower than kinetics at 300 K (Figure 2.15d). This behavior occurring at constant Φ_{PL} is in very good agreement with previous observations for stoichiometric $CuInS_2$ NCs [83] and suggest a further fine structure of the band edge exciton featuring an higher lying emissive state and a non-emissive state in thermal equilibrium with the environment and responsible for the long PL decay at low T. In analogy to stoichiometric $CuInS_2$ NCs discussed in Section 2.2, both such states belong to the weakly allowed exciton consisting of a CB electron and a hole in the odd -parity VB sublevel. Therefore, the long-lived weakly emissive exciton is labeled as "dark" (D) and the higher-lying emissive exciton as "gray" (G), to distinguish the current case from the case of CdSe quantum dots, where the emissive state is optically allowed and therefore referred to as "bright". By assuming a Boltzmann distribution of excitons between these two dark and gray states, the transition between the slow and fast decay regimes is modeled with a three-level scheme (inset of Figure 2.15c), by expressing the radiative decay rate using equation 2.2. The model yields a Δ_S value of 3.2 meV consistent with what found in $CuInS_2$ NCs of similar size2.2. Importantly, analogous temperature-controlled time-resolved PL measurements on Ag:CdSe NCs (Figure 2.15e and 2.15f), show exclusively the lengthening of PL decays with decreasing Tdue to suppression of thermally activated non-radiative channels and no fine structure effects, thus corroborating the picture that the observed optical behavior is direct consequence of the band edge exciton structure of $AgInS_2$ NCs and not to the involvement of localized defect states.

2.3.4 Conclusions

In summary, I combined ultra-fast TT and MCD spectroscopies as well as temperature-dependent PL and SEC experiments to investigate the recombination mechanisms in ternary $AgInS_2$ NCs. Optical absorption and TT measurements reveal two spectral contributions responsible for the broadband absorption profile, in agreement with recent theoretical models. Temperature dependent MCD experiments indicate the absence of Ag-related intragap acceptors states acting as radiative recombination centers. Time-resolved PL measurements as a function of temperature show a further fine

structure of the band-edge exciton, that is not present in Ag:CdSe NCs, which can be associated with the intrinsic (non-trap mediated) PL nature in $AgInS_2$ NCs. Finally, temperature dependent PL and SEC experiments reveals that surface electron trapping is the main nonradiative loss channel, that can be suppressed via electrochemical passivation of electron traps or by lowering the temperature to 3.5 K, leading to PL efficiency close to unity.

Chapter 3

Novel Strategies in Lead Halide Perovskites Nanostructures Towards Effective Radiation Detection and Energy Conversion Schemes

Radiation detection is of outmost importance in fundamental scientific research and applications including medical diagnostics, homeland security, environmental monitoring, and non-destructive inspection in industrial manufacturing [95, 96]. Lead halide perovskites (LHP), prized for their solution processability, strong light-matter interaction [97, 98], large electron-hole diffusion length [88, 97] and tunable, intense radioluminescence (RL) at visible wavelengths [99, 100] are attracting growing attention as high-atomic number (Z) materials for next generation scintillators and photoconductors for ionizing radiation detection [100–103]. To unlock their full potential as reliable and cost-effective alternatives to conventional scintillators, LHP urge to conjugate high scintillation yields with fast emission lifetime, mitigated reabsorption to suppress losses in large volume/high-density detectors, and emission stability over prolonged exposure to high doses of ionizing radiation. Nonetheless, no clear picture of radiative and non-radiative mechanisms involved in the scintillation process has been reported to date, as well as on the role of the material dimensionality, or their radiation hardness for doses above a few kGy. In this chapter, following the work on reabsorption-free LSCs previously described, I first tackle the technological problem of producing efficient and fast scintillators for large-area detectors. To do this $CsPbBr_3$ NCs are employed as high-atomic number (Z) sensitizers for a conjugated organic dye designed so as to exhibit

a large Stokes shift and a short emission lifetime also when embedded in a polymeric matrix. This approach leads to the fabrication of the first example of low reabsorption, fast and efficient perovskite plastic scintillator showing performance approaching high-quality commercial plastic and bulk crystals scintillators, and emission lifetime competitive with established fast scintillators based on rare earths. These results encourage further studies geared towards unlocking the full technological potential of LHP NCs. This issue is addressed by performing, for the first time, a comprehensive study using radioluminescence and photoluminescence measurements side-by-side to thermally-stimulated luminescence (TSL) and afterglow experiments on $CsPbBr_3$ with increasing dimensionality, namely nanocubes, nanowires, nanosheets, and bulk crystals. All systems are found to be affected by shallow defects resulting in delayed intragap emission following detrapping via a-thermal tunneling. TSL further reveals the existence of additional temperature-activated detrapping pathways from deeper trap states, whose effect grows with the material dimensionality, becoming the dominant process in bulk crystals. Having established solid experimental background in LHPs trapping/detrapping mechanisms, with a view to systematically boost emission yield and to extend the use of LHP in harsh environments, is demonstrated that post-synthesis resurfacing with fluorine ions passivates trap states at the NC surface responsible for delayed emissions also producing over 500% enhancement of the scintillation efficiency now matching with commercial bulk scintillator crystals. These results have profound implications for the widespread of LHPs in radiation detection schemes for high-energy physics, nuclear batteries, as well as in space-grade solar cells where high radiation hardness is critical for successful and long-running operation.

3.1 State of the Art

Key features in radiation detection are high interaction probability with ionizing radiation and efficient direct conversion of radiation into charge carriers, both enhanced in high-Z materials [104]. For this reason, all-inorganic ($CsPbX_3$, X= Br, I, Cl) and hybrid organic-inorganic ($APbX_3$, A=methyl ammonium, MA; formamidinium, FA) lead halide perovskites have emerged as promising new class of materials for the development of both direct radiation-to-charge converters and scintillation-based detectors [105]. Very recently, hybrid $MAPbBr_3$ single crystals have shown X-ray sensitivity 1000-fold larger than conventional amorphous α-Se X-ray photoconductors, allowing to significantly reduce the dose exposure, which is a critical parameter in medical

imaging. Similarly, planar devices based on $CsPbBr_3$ single crystals have shown energy resolution comparable to commercial γ-ray $Cd_{1-x}Zn_xTe$ (CZT) detectors [106]. At the nanoscale, colloidal synthesis routes for LHP nanocrystals (NCs) have further opened to the demonstration of fast-emitting and color tunable scintillators across the UV-visible spectrum, achievable by tailoring the exciton recombination energy via size [107–109] and composition control [110]. As result, efficient LHP NCs can be produced at room temperature featuring narrow emission band and broad color gamut [99, 102], as well as be processed into photoconductive films [99] or be directly synthetized in-situ onto pattern rigid or flexible substrates to fabricate large scale detectors arrays [111]. These aspects represent substantial improvements with respect to conventional rare-earth-doped scintillators, such as perovskites [112,113], silicates [114] and mixed garnets [115–117], where the emission energy is dictated by the dipole allowed transitions of the emitting center, and production volumes are limited by costly and complicated monolithic synthesis routes at high temperature.

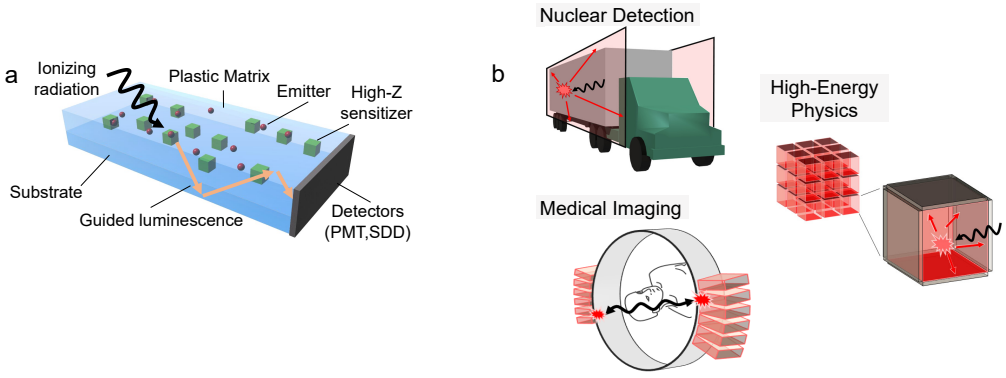

Figure 3.1: ***a)*** *Schematic depiction of a high-Z sensitized plastic scintillator and* ***(b)*** *its applications in nuclear detection, diagnostic imaging and high-energy physics.*

In the last decades, before the introduction of LHP NCs, plastic scintillators have emerged as affordable alternatives to conventional inorganic scintillating crystals that can be fabricated in different sizes and shapes with features suitably tuned for specific applications [118]. In the most common embodiment, these devices consist of transparent polymeric matrices doped or coated with scintillating materials, typically organic dyes or polymers (Figure 3.1a). Owing to their fabrication versatility and lightweight, plastic scintillators find application, among others, in sectors such as nuclear monitoring and border control, where large-area radiation portal monitors are employed for the detection of nuclear materials in vehicles and cargo containers (Figure 3.1b). Along the same lines, thin films of fast scintillators, also coupled to massive crystals,

are being investigated for advancing radiometry applications relying on the time of flight (TOF) technique [119, 120]. These include medical imaging in positron emission tomography (TOF-PET, Figure 3.1b), where fast timing is critical for the image quality and their reconstruction process, as well as in high-energy physics experiments, where high event rates in high-luminosity colliders require a fast response to mitigate the pile-up and to localize the events vertexes. Therefore, plastic scintillators offer a technologically mature platform in which to experiment LHPs in order to combine the flexibility of fabrication and customization of plastic matrices with the advanced optical and scintillation properties of LHP NCs.

All these ground-breaking advancements highlight the potential of LHP NCs as active components of novel, efficient, and flexible radiation detectors. Nonetheless, as of today, very little is known about the thermodynamics and kinetics of trapping and detrapping mechanisms of carriers generated upon interaction with ionizing radiation as well as the radiation hardness of LHP NCs which remain often considered as easily damaged by the exposure to ionizing radiation. Shallow and deep defects within LHP forbidden gap are both responsible for relevant, and typically detrimental, effects on the scintillation process. Specifically, shallow traps with longer but comparable lifetime to the scintillation decay-time are known to compromise the time-resolution of scintillators causing slow scintillation tails due to slow detrapping. [121, 122] On the other hand, deep traps - that is, localized electronic states with a lifetime much longer than the scintillation decay time - trap carriers in a stable and irreversible way (except upon the delivery of the necessary energy budget), thereby reducing the scintillation efficiency. [114, 123] Finally, intermediate trapping behaviors can also be present, leading to millisecond long RL decay tails commonly referred to as afterglow (AG). [121, 124, 125] While recent reports investigated a seemingly ubiquitous low-temperature trap emission in the photoluminescence (PL) [126–129] and RL [130] spectra of $CsPbBr_3$ nanostructures and bulk single crystals (BSCs), no information concerning non-radiative intermediate and deep traps is available in the literature, as well as on the role of the material dimensionality on the trapping and detrapping processes. So far, no materials-design strategy has been demonstrated to suppress parasitic charge trapping and detrapping processes boosting the scintillation efficiency and suppressing unwanted slow emission tails that might limit the use of LHPs in fast timing applications such as positron emission tomography [119, 131].

3.2 Efficient, Fast and Reabsorption-Free Sensitized Plastic Scintillators Based on $CsPbBr_3$ NCs

Having established solid experimental background in LHPs trapping/detrapping mechanisms, in this section I tackle the technological problem of producing efficient and fast scintillators for large-area detectors. Here I contribute to address this problem by demonstrating the first example of a plastic scintillator exploiting perovskite NCs as high-Z sensitizers for a conjugated organic emitter specifically engineered to feature a large Stokes shift between its absorption and emission spectra and fast emission lifetime. Altogether, this hybrid design ensures strong interaction with ionizing radiation by the NC sensitizers, nearly reabsorption-free waveguiding of the scintillation light and a fast detection speed. The organic molecule of choice is the perylene dyad 9,9'-Bis[perylene-3,4-dicarboxylic-3,4-(N-(2,5-Di-tert-butylphenyl)] (hereafter indicated as **1**), whose chemical structure is depicted in Figure 1c together with the respective band diagram showing HOMO and LUMO levels perfectly isoenergetic to the valence and conduction bands of $CsPbBr_3$ NCs. This is relevant to prevent charge separation between the two species, leading to slow indirect exciton decay or efficiency losses by exciton splitting. $CsPbBr_3$ NCs were selected as high-Z sensitizers as they combine spectrally tuneable luminescence [107, 132], heavy-metal-based composition and unmatched tolerance to structural defects (so-called defect tolerance) [133]. This ensures very high emission quantum efficiency also in NCs without engineered passivating shells that can be produced at room temperature with highly scalable and cost affordable methods [107]. This aspect is of great importance for both the fabrication of large-area scintillating waveguides and for the study of rare events in fundamental physics, where the collection of statistically significant experimental data requires very large volume detectors typically based on tons of scintillating materials. Owing to these advantageous properties, lead halide perovskites have recently emerged as promising candidates for radiation detection, as testified by successful demonstrations of X- and γ-rays electronic-based detectors and scintillators based on nanostructured, film and single perovskite crystals [99, 106, 134–141]. Importantly for our design, $CsPbBr_3$ NCs exhibit high luminescence quantum yield and perfect resonance between their emission spectrum and the optical absorption of **1**. This is key for several reasons, namely to provide high efficiency via nearly complete loss-free sensitization of the dyad to ensure reabsorption-free waveguiding of the sensitized scintillation light and to obtain an emission lifetime of less than 4 ns, which is faster than the luminescence of spin al-

lowed 5d-4f transitions of Ce^{3+} and Pr^{3+} cations used in conventional fast scintillators crystals (typically tens of nanoseconds) [115]. Faster scintillating compounds do exist, such as BaF_2, relying on core-valence transitions (0.6-3 ns), however they typically feature a limited light yield (c.a. 1400 ph/MeV for BaF_2) [142]. Importantly, as shown below, the competitive performance of our sensitized nanocomposite results directly from the synergy between the NC and the dye and could have not been obtained by using the two components independently. This is because, **1** features a low interaction probability with ionizing radiation and the $CsPbBr_3$ NCs exhibit a luminescence lifetime of tens of nanoseconds and a very small Stokes shift between their absorption and luminescence spectra that results in strong reabsorption of the emitted light. This is particularly detrimental in high-volume/high-load detectors featuring huge optical density, and in large-size waveguides in which the optical distance between the scintillation event and the device edges is particularly long. The same problem afflicts other light-management applications such as luminescent solar concentration [91], the solution of which has generated a variety of approaches for increasing the Stokes-shift of perovskite NCs, including doping [143] or the use of multi-layered perovskite nanostructures [144]. Stokes-shift-engineering of perovskite NCs, however, typically comes with a cost in terms of the luminescence lifetime that can increase up to milliseconds in reabsorption-free Mn-doped NCs [91], thus rendering such systems unsuitable for fast-timing or high-luminosity applications. For these reasons, no example of efficient perovskite-based plastic scintillator free from reabsorption losses and with fast temporal response has been reported to date.

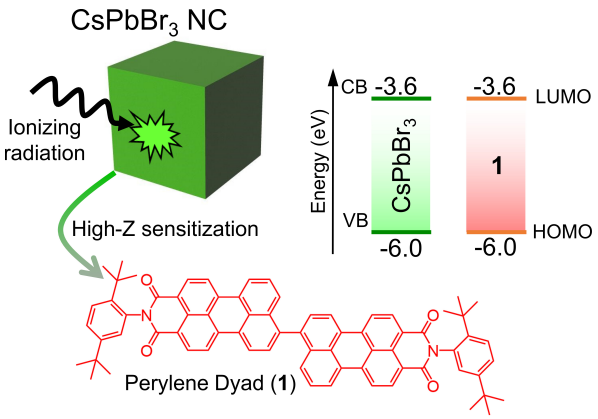

Figure 3.2: *Sketch of a $CsPbBr_3$ NC sensitizing the perylene dyad 9,9'-Bis[perylene-3,4-dicarboxylic-3,4-(N-(2,5-Di-tert-butylphenyl)] (labelled **1** for brevity). The energy levels of the two systems are also shown to highlight the resonance between the respective frontier levels.*

Side-by-side photoluminescence and radioluminescence experiments on both liquid solution and in poly (methyl methacrylate) (PMMA) nanocomposites, embedding mixtures of **1** and the $CsPbBr_3$ NCs, demonstrate essentially perfect sensitization in PMMA. As a result, the radioluminescence response of **1** sensitized by the NCs in PMMA is nearly 30-fold that of the emitter alone. Comparative radioluminescence measurements show that the performance of our hybrid sensitized plastic scintillator is quantitatively comparable to that of massive commercial bismuth germanate (BGO) scintillation crystals with light output as high as $\sim$ 9000 ph/MeV [145]. Furthermore, measurements using 5.5 MeV α-particles emitted by ^{241}Am isotopes as excitation source suggest an achievable light yield larger than 1000 ph/MeVα, thus further corroborating the applicative potential of our design, since the alpha light yield in plastic scintillators is typically much smaller than the X- or γ- light yield. Finally, I experimentally demonstrate the effectiveness of mitigating reabsorption losses strategy in large size radiation detectors by fabricating plastic scintillator consisting of a PMMA waveguide coated with NC:**1** PMMA nanocomposite layer. According to the sensitization effect of the NCs and the large Stokes shift of **1**, the radioluminescence of our proof-of-concept device propagates for long optical distances with very small loss by reabsorption, in full agreement with Monte Carlo ray-tracing simulations. Similar measurements performed by exposing the device to the α-particles radiated by ^{241}Am isotopes confirm nearly reabsorption-free waveguiding of the scintillation light also in operative conditions.

3.2.1 Samples Description

Synthesis of 9,9'-Bis[perylene-3,4-dicarboxylic-3,4-(N-(2,5-Di-tert-butylphenyl)]

Under N_2 atmosphere, a mixture of Ni(COD)2 (187 mg, 0.680 mmol), COD (610 mg, 5.64 mmol), Bipy (106.15 mg, 0.680 mmol) and anhydrous DMF (60 ml) is prepared and stirred at room temperature (RT) for 1 h obtaining a purple solution. N-(2,5-Di-tert-butylphenyl)-9-bromo- perylene-3,4-dicarboximid [146] (400 mg, 0.680 mmol) is added to the solution and the mixture is stirred at 65°C for 20 h. The reaction mixture is poured in HCl(aq.) 5% (400 ml) and stirred for 45 min at RT. The solid product is filtered on filter paper, washed with H_2O (300 ml) and H_2O/MeOH 1:1 (100 ml). The residue that is eliminated during the filtering process on paper is extracted with toluene in a Knofler-Bohm extractor with simultaneous azeotropic removal of residual water with a Dean-Stark apparatus. The extract is evaporated under reduced pressure and the solid residue is further purified by chromatography (SiO_2, eluent: CH_2Cl_2) obtaining product as a red solid (212 mg, 0.208 mmol, yield: 61%).

Synthesis of $CsPbBr_3$ NCs

2 mL hexane, 1 mL isopropanol, and 5 µL ml of Cs_2Co_3 (dissolved in pure propionic acid at 1 M) were mixed in air and at room temperature, followed by the injection of 100 µL of lead bromide precursor (0.5 M in a mixture of isopropanol, propionic acid and butylamine at volume ratio of 1:1:1). The solution immediately turned green, with the precipitation of $CsPbBr_3$ NCs, which were centrifuged for 2 min at 1000 rpm and redispersed in 600 µl of toluene.

Preparation of the polymeric nanocomposites

In a vial, toluene solution of appropriate concentration of $CsPbBr_3$ NCs and/or **1** were added to a $CHCl_2$ solution (1 ml) containing 120 mg of poly-methyl methacrylate. Upon evaporation at 20°C for 22 hours in $CHCl_2$ atmosphere, smooth and homogeneous polymeric nanocomposites (0.4mm thick, 12 mm diameter) were obtained. The same procedure was adopted to produce the active layer of the scintillator waveguide using a PMMA waveguide as substrate. The PMMA waveguide was fabricated by bulk polymerization using the industrial cell-casting process. First, the so-called 'syrup' was prepared. The monomer methyl methacrylate (MMA 99%, Aldrich), purified through a basic aluminium oxide column, was heated in a beaker to 80 °C. When the MMA temperature stabilized, 2,2'-Azobis(2-methylpropionitrile) (AIBN, 98%, Aldrich, 100 ppm *wt/wt* with respect to MMA) was added. At that point, pre-polymerization (an exothermic process) took place and the monomer temperature increased to the MMA boiling temperature (95 °C). When the monomer achieved the stage of vigorous boiling, the syrup was quenched. In the second step, the pre-polymer was degassed by four freeze–pump–thaw cycles in order to remove oxygen and introduce an argon atmosphere, and then mixed with MMA containing lauryl peroxide (98%, Aldrich, 400 ppm *wt/wt* with respect to MMA) described above (10% *wt/wt* with respect to the syrup). Finally, the viscous liquid was introduced into the casting mould under argon flow, where the polymerization reaction proceeded. The casting mould was made from two glass plates sealed with a polyvinyl chloride (PVC) gasket (to preserve the inert atmosphere) and clamped together. The clamps contained springs in order to accommodate the shrinkage of the polymer plate during the polymerization process. The casting mould was placed in a water bath at 55 °C for 48 h. Finally, the bar was post-cured in the oven at 115 °C overnight.

3.2.2 Experimental Details

Optical spectroscopy

Steady-state and time-resolved photoluminescence (PL) spectra as a function of temperature were performed using the setup described in Section 2.2.2.

Radioluminescence spectroscopy

The samples were excited by ionizing radiation using a Philips 2274 X-ray tube operating at 30 kV and 30 mA through a beryllium window. At this operating voltage, X-rays are produced by a Bremsstrahlung mechanism due to the impact of electrons generated through thermionic effect and accelerated onto a tungsten target. The radioluminescence spectra were collected at room temperature with a homemade apparatus featuring a liquid nitrogen-cooled, back-illuminated and UV-enhanced, CCD detector (Jobin Yvon Symphony II) coupled to a monochromator (Jobin Yvon Triax 180) equipped with a 100 grooves/mm grating as detection system. The spectra were corrected for the spectral response of the acquisition system. The dose values reported in the text for X-ray irradiations were obtained by comparison with a calibrated ^{90}Sr-^{90}Y beta radioactive source and using optically stimulated luminescence emission from quartz crystalline powder (100-200 μm).

Measurements with ionizing sources

The PMMA nanocomposite samples were faced to a 6×6 mm^2 Hamamatsu s13360-6050CS silicon photomultiplier (SiPM). The anode current was read out by a LMH6702 wide bandwidth operational amplifier. The amplitude of the signal is proportional to the number of activated cells of the SiPM. The signals from the SiPM were collected with a 2 GHz, 12-Bit oscilloscope and analyzed to extract the pulse amplitude information. A calibration measurement without samples was first performed to evaluate the proportionality factor between number of activated cells and voltage. When no direct photon source illuminates the detector, single cells can be activated only by single electrons emitted by thermal effect. As a consequence, amplitudes related to single, double and triple cell activation can be easily identified and can be used to extract the voltage signal amplitude that corresponds to exactly 1 electron, as in the case of the photoelectron extracted by 1 photon. After the calibration measurement, the PMMA nanocomposite samples were faced towards the SiPM surface.

Two sources of ionizing radiation were used: a ^{241}Am source that emits alpha

particles with energy of 5.5 MeV (It also emits X-rays with energies ranging from 11 to 26 keV) and ^{224}Rn and subsequent nuclei of the Thorium chain implanted on the surface of the samples. The energies of the alphas emitted in the decay of such implanted nuclei range from 4 to 10 MeV. In the case of the ^{241}Am source, control experiments with the sample shielded from alpha radiation were performed showing strong reduction in the total measured rate and in the rate of events corresponding to a high number of cells fired simultaneously, thus confirming that the signal emerges from interaction between the alpha particles and the nanocomposite.

3.2.3 Results

Optical Properties

The $CsPbBr_3$ NCs were synthesized following the room temperature large-scale protocol introduced by Akkerman et al. [147]. The organic emitter **1** was synthesized according to the procedure reported in the Experimental section. Figure 3.3a reports the molar extinction coefficient and photoluminescence spectra of the two systems in toluene solution. The $CsPbBr_3$ NCs exhibit the typical narrowband photoluminescence at ∼518 nm (FWHM∼25 nm) nearly resonant to the respective first excitonic absorption peak at ∼514 nm. The photoluminescence quantum yield, as measured with an integrating sphere, is $\Phi_{PL,NC} = 75\pm8\%$. The optical absorption spectrum of **1** shows a first vibronic peak at 520 nm followed by progressively weaker replicas at higher energy ($\Delta_E \sim 150$ meV). Crucially, such a spectrum exhibits essentially perfect spectral overlap with the emission peak of the NCs, which ensures efficient sensitization of **1** upon NC excitation by both UV light and ionizing radiation as discussed in detail below. The photoluminescence spectrum of **1** is peaked at 582 nm ($\Phi_{PL,1} = 60\pm5\%$), corresponding to a Stokes shift as large as ∼60 nm from the respective absorption edge, originating from the planarization of the perylene units in the excited state. This, together with the sharp absorption onset, lead to a very small spectral overlap between the absorption and the luminescence of **1**, which is the key for suppressing reabsorption losses.

In order to evaluate the potential of **1** as a reabsorption-free emitter by taking into consideration the effect of stochastic reabsorption and re-emission events in a real waveguide, a Monte Carlo ray tracing simulations of light propagation were performed in collaboration with Glass To Power Spa. In these simulations, we used the experimental absorption and photoluminescence spectra reported in Figure 3.3a and the device dimensions (0.5 cm × 0.7 cm × 15 cm, active layer thickness 300μm), refractive

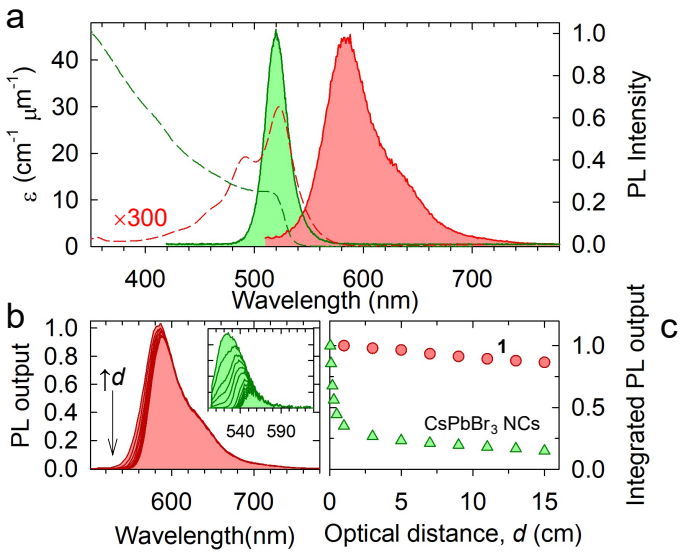

Figure 3.3: ***a)*** *Molar extinction coefficient (dashed lines) and photoluminescence spectra (solid lines) of the NCs (green, excitation wavelength $\lambda_{EX} = 405$ nm) and **1** (red, $\lambda_{EX} = 500$ nm). The extinction spectrum of **1** was scaled by a factor of 300 for clarity.* ***b)*** *Photoluminescence spectra of **1** obtained via Monte Carlo ray tracing simulation as a function of increasing optical distance, d, between the excitation spot and the edge of a plastic waveguide calculated considering the experimental quantum yield $\Phi_{PL,1} = 60 \pm 5\%$. Inset: Photoluminescence spectra for an identical simulated device based on $CsPbBr_3$ NCs.* ***c)*** *The corresponding spectrally integrated photoluminescence intensity vs. d showing near-invariance of the emission intensity. The trend for the device based on $CsPbBr_3$ NCs (green triangles) shows strong drop by reabsorption for $d < 1$ cm.*

index and optical density (1 OD at 522 nm) of the real plastic scintillator waveguide demonstrated later in this work. Simulations thus investigated the evolution of the light output probability from one of the small 0.5 cm × 0.7 cm edges for an increasingly long optical distance, d, from the excitation spot. In Figure 3.3b and 3.3c I report the simulated photoluminescence spectra vs. d together with the evolution of the respective integrated intensity. Importantly, reabsorption causes only a minor intensity drop of the high-energy spectral portion of the luminescence spectrum resulting in very limited reabsorption losses of only ∼15% for d as long as 15 cm. In contrast, simulations considering an identical device but based on $CsPbBr_3$ NCs show strong drop by reabsorption in less than one centimeter, consistent with the nearly perfect resonance between the respective absorption and photoluminescence spectra.

Sensitization process in solution and in polymer nanocomposites

Based on the promising optical properties of our Stokes shift engineered organic emitter, I proceeded with the experimental demonstration of its efficient sensitization by the NCs. With this aim, I first monitored the photoluminescence spectrum of binary mixtures of the $CsPbBr_3$ NCs and **1** in toluene solutions using selective optical excitation at 400 nm where the molar extinction coefficient of **1** (ϵ_1 =$\sim$6$\times10^{-3}$ cm$^{-1}\mu$M^{-1}) is $\sim$5000-fold smaller with respect to the NCs (ϵ_{NCs} = $\sim$30 cm$^{-1}\mu$M^{-1}, Figure 3.3a). In this condition, direct photo-excitation of **1** is negligible and the emerging photoluminescence is thus ascribed to sensitization by the NC. The photoluminescence spectra of the solutions at increasing concentration of **1** are reported in Figure 3.4a.

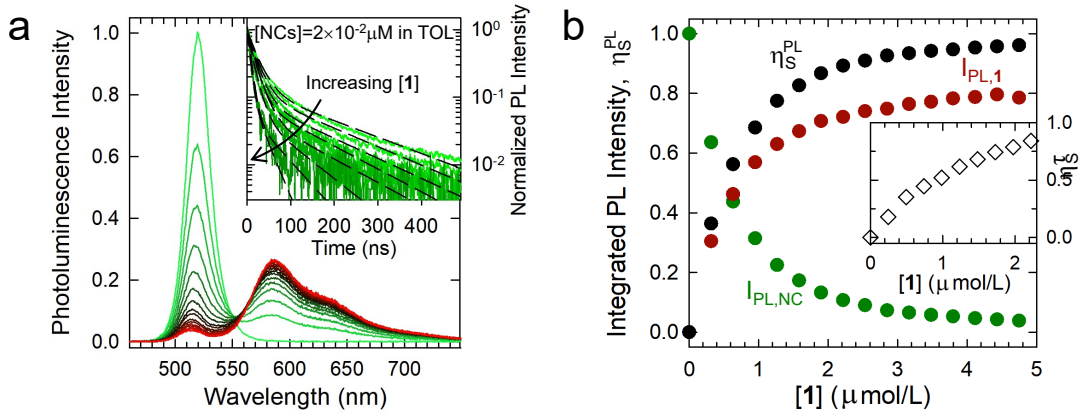

Figure 3.4: ***a)*** *Photoluminescence spectra of toluene (TOL) solution of $CsPbBr_3$ NCs with increasing concentration of* ***1*** *(**[1]**, from zero, green curve, to 4.8 μM, red curve) under selective NC excitation at λ_{ex} = 400 nm. Inset: respective photoluminescence decay traces for **[1]** from zero to 2.2 μM together with the fitting curves (dashed black lines) to double exponential functions.* ***b)*** *Integrated photoluminescence intensity of the NC ($I_{PL,NC}$, green circles) and* ***1*** *($I_{PL,1}$, red circles) extracted from the spectra in a as a function of **[1]**. The black circles are the respective sensitization efficiency (η_S^{PL}) values. Inset: sensitization efficiency, η_S^{τ}, as a function of **[1]**.*

Consistent with the strong spectral resonance between the NC luminescence and the absorption spectrum of **1**, the NC emission progressively drops to nearly zero accompanied by the concomitant growth of the luminescence of **1**, with a clear isosbestic point at $\sim$550 nm indicating that the changes in amplitude of the two contributions are linearly related. The anti-correlation between the two trends is highlighted in Figure 3.4b, where the evolution of the respective spectrally integrated intensities ($I_{PL,NC}$, $I_{PL,1}$) vs. [**1**] is reported. Notably, by keeping into account the respective photoluminescence quantum yields, I obtain that for [**1**] $\geq$ 3.5 μM, the emission by the NCs alone ($I_{PL,NC}(0)$) is nearly perfectly compensated by the luminescence of **1**, indicating

that in such conditions sensitization occurs with essentially no losses. Consistently, the sensitization efficiency (η_S^{PL}) extracted from the evolution of the NC emission intensity vs. [**1**] through the expression $\eta_S^{PL} = 1 - I_{PL,NC}([1])/I_{PL,NC}(0)$, approaches unity in the same concentration range. In order to investigate the nature of the sensitization process in greater detail, I performed time-resolved measurements of the NC photoluminescence at increasing concentration of **1**. As shown in the inset of Figure 3.4a, the emission dynamics of the pure NCs is double exponential, with a fast component ($\tau_{Fast} \sim 30$ ns) due to the direct decay of band-edge excitons, followed by a longer-lived decay ($\tau_{Slow} \sim 215$ ns) that is commonly ascribed to thermally repopulated band-edge excitons from shallow trap states typical of halide perovskite materials [148, 149]. Notably, upon increasing the concentration of **1**, the NC emission kinetics progressively accelerates, resulting in $\tau_{Fast} \sim 5$ ns ($\tau_{Slow} \sim 25$ ns) for [**1**]$\sim$2.2 μM. This, together with the evolution of the emission spectrum with [**1**], strongly suggests that the sensitization under selective UV excitation of the NCs is a nonradiative process mediated by the NC band-edge exciton, likely associated to resonant energy transfer. Consistently, the sensitization efficiency extracted from the analysis of the fast component of the NC emission kinetics as $\eta_S^{\tau} = 1 - \tau_{NC}([1])/\tau_{NC}(0)$ reported in the inset of Figure 3.4b, is in quantitative agreement with the evolution of η_S^{PL}.

A practical demonstration of efficient high-Z sensitized plastic scintillators based on $CsPbBr_3$ NCs and **1** is, however, not straightforward as it requires that both systems retain their optical properties when embedded into polymeric composites and that the sensitization process takes place in such a medium under excitation by ionizing radiation. To experimentally assess these key aspects, the team focused on the fabrication of PMMA nanocomposites embedding the NCs and **1** both individually and blended. Among possible polymers, PMMA was specifically chosen for its high optical quality, low absorption coefficient across the whole visible spectrum resulting in minimal absorption losses by the scintillator matrix also for large size devices and its good radiation hardness [150]. For these reasons, PMMA is commonly used for fabricating plastic optical fibers also adopted in dosimetry. For the fabrication of the nanocomposites, the two species were added to PMMA dissolved into dichloromethane and finely mixed by vigorous stirring for 5 minutes. In order to strengthen the interaction with ionizing radiation in view of potential application, the nanocomposites were produced with 2.0 $wt\%$ of the NCs, whereas the amount of **1** was tuned to maximize the sensitization efficiency as discussed below. The obtained thick solutions were then dried in controlled conditions of temperature (20°C) and dichloromethane vapor atmosphere. This is important to control the evaporation kinetics of the solvent so as

to avoid the formation of bubbles and cracks occurring for rapid drying process, as well as to prevent precipitation of the NCs and phase segregation of **1** leading to the formation of non-emissive molecular aggregates for excessively slow kinetics. By tuning the drying time to ∼22 hours, smooth and homogeneous PMMA solid composites (thickness around 0.4 mm) were obtained.

In Figure 3.5a and 3.5b are reported the photoluminescence spectra of two PMMA nanocomposites, respectively embedding 2.0 $wt\%$ of NCs or 0.15 $wt\%$ of **1** compared to the respective toluene solutions. The spectral profiles and photoluminescence decay curves in the two media are very similar to each other, indicating no significant effect by the incorporation into the polymer for either emitter. The respective photoluminescence decay curves are shown in Figure 3.5c and 3.5d. Similar dynamics are observed for the $CsPbBr_3$ NCs in toluene and in PMMA, with a minor acceleration of both components ($\tau_{Fast} \sim 23$ ns, $\tau_{Slow} \sim 180$ ns vs. $\tau_{Fast} \sim 30$ ns and $\tau_{Slow} \sim 215$ ns) in the nanocomposite possibly due to the activation of nonradiative losses following the incorporation into the slightly polar PMMA matrix, in agreement with recent single particle spectroscopy results on $CsPbBr_3$ NCs [151]. Consistently, the photoluminescence quantum yield of the NCs in PMMA measured with an integrating sphere decreases to $\Phi_{PL,NC} = 65\pm5\%$. Crucially, in full agreement with the photoluminescence decay data in toluene solutions (Figure 3.4a), the emission dynamics of the NCs in the blended nanocomposite ([**1**]=0.15$wt\%$) is much faster that for bare NCs in PMMA. This indicates that also in the polymer matrix the main decay channel for the NC band-edge excitons is nonradiative energy transfer to the dye. The photoluminescence kinetics of **1** is single exponential in both toluene and PMMA and the lifetime increases from 2.8 ns to 3.9 ns in the plastic matrix. This is ascribed to the suppression of the rotational degrees of freedom of the perylene units around the central bond and of the aryl sidechains that lead to nonradiative losses in the toluene solution. Accordingly, the photoluminescence efficiency of **1** increases to $\Phi_{PL,1} = 78\pm5\%$ in the nanocomposite. Even more importantly for our purposes, the radioluminescence spectra - excited by Bremsstrahlung radiation through a X-ray tube with tungsten target, operated at 30 kV - of the NCs and **1** in PMMA are very close to the respective photoluminescence profiles (Figure 3.5a and 3.5b), indicating that interaction with X-rays creates the same excited states as optical excitation.

Based on this crucial point, I proceeded with analyzing the sensitization process in PMMA under X-ray excitation. In Figure 3.5e is reported the radioluminescence spectra of PMMA nanocomposites containing 2.0 $wt\%$ of NCs and increasing loads of **1** from zero to 0.155$wt\%$. The radioluminescence spectra follow a nearly identical

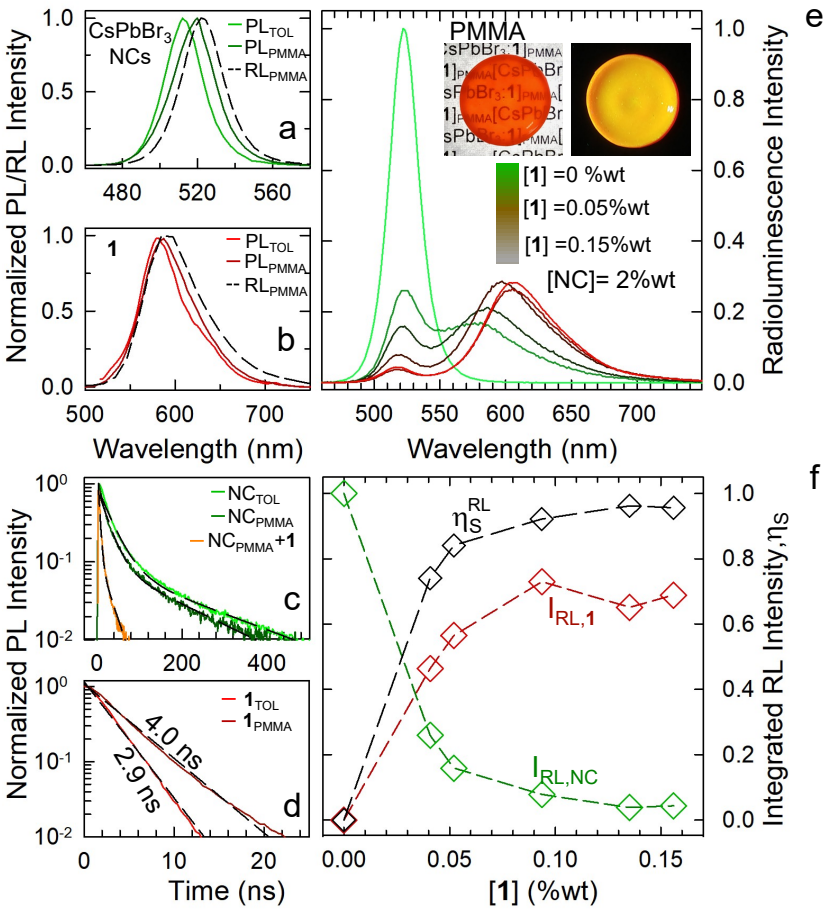

Figure 3.5: **a, b)** *Photoluminescence spectra of toluene solutions (PL_{TOL}) and PMMA nanocomposites (PL_{PMMA}) containing pure NCs (2.0 wt%, λ_{ex} = 400 nm; 'a') and* ***1*** *(0.155 wt%, λ_{ex} = 500 nm; 'b') compared to the radioluminescence spectra of the respective nanocomposites (RL_{PMMA}).* **c)** *Photoluminescence decay curves of $CsPbBr_3$ NCs in toluene solution (NC_{TOL}) compared to PMMA nanocomposites containing pure NCs (NC–PMMA, 2.0 wt%) or a NC–****1*** *blend (NC–****1****–PMMA, 2.0 wt%:0.155 wt%). The respective fits to a double exponential function are shown as dashed black lines.* **d)** *Photoluminescence decay curves of* ***1*** *in toluene ($\mathbf{1}_{TOL}$) or in a PMMA nanocomposite (****1****–PMMA, [****1****] = 0.15 wt%) together with the respective single-exponential fitting curves (dashed black lines).* **e)** *Radioluminescence spectra of PMMA nanocomposites embedding 2 wt% of NCs and increasing loads of* ***1*** *from zero to 0.155 wt%. Inset: photographs of a PMMA nanocomposite embedding NC–****1*** *blends (2.0 wt%:0.155 wt%) illuminated by ambient light (left) and 400 nm light (right).* **f)** *Integrated radioluminescence intensity of the NC ($I_{RL,NC}$, green diamonds) and* ***1*** *($I_{RL,1}$, red diamonds) extracted from the spectra in 'e' as a function of [****1****]. The black diamonds are the respective η_S^{RL} values.*

trend to that observed for the toluene solution under selective NC excitation (Figure 3.4a), with the radioluminescence of the pure NCs at ∼520 nm progressively turning into the emission of **1** peaked at ∼605 nm. The effect is highlighted in Figure 3.5f

showing the nearly perfect anticorrelation between the respective integrated radioluminescence intensities resulting in the sensitization efficiency to saturate at $\eta_S \sim 95\%$ for $[\mathbf{1}] \geq 0.01 wt\%$ which indicates that sensitization takes place with negligible losses also in the plastic nanocomposites under X-ray excitation. I point out that, despite the time-resolved photoluminescence measurements in Figure 3.5c demonstrate that the sensitization of **1** under UV excitation is due to efficient nonradiative energy transfer from the NC's band-edge excitons, the mechanism leading to the sensitized emission of **1** could be more complex using ionizing radiation, likely involving co-existing processes activated by primary interaction of the ionizing radiation in the NCs, as well as in the polymer matrix. Specifically, primary interactions in the NC could produce, together with excitons, also high-energy free electrons, both by photoelectric effect and by Auger-mediated relaxation of deep holes, that could excite other NCs or **1** along their track. Monte Carlo simulations by Bulin et al. [152] have recently shown that a significant fraction of energy produced by primary interaction between ionizing radiation and NCs is indeed deposited outside the NC. In this case, the sensitization process is not solely determined by energy transfer from the NC excitons to the dyad and the dimming of the NC radioluminescence intensity with increasing [**1**] shown in Figure 3.5e and 3.5f could be caused also by a progressively larger fraction of propagating electrons being intercepted by **1** molecules. Similarly, excited NCs and **1** could be produced by electrons emitted by PMMA, however, this effect is likely very weak given the very large difference between the radioluminescence intensity of **1** in the presence and in the absence of the NCs reported below.

Proof-of-concept: sensitized nanoscintillators

The efficient high-Z sensitization of **1** by the NCs has a profound effect on the radioluminescence properties of the PMMA nanocomposites, resulting in scintillation performance comparable to commercial massive scintillator crystals. This is highlighted in Figure 3a where is reported the radioluminescence spectra performed in the exact conditions of X-ray irradiation and collection geometry of two PMMA nanocomposites of the same dimensions (thickness = 0.4 mm, diameter = 12 mm) embedding identical quantities of **1** ($0.155 wt\%$) with or without the NCs ($2 wt\%$), as well as of a massive $Bi_4Ge_3O_{12}$ (BGO) crystal and a commercial plastic scintillator (Kuraray SCSF-3HF). BGO is an optimal scintillator material suitable for radiation detectors in various fields from medical equipment to high energy physics, owing to the high atomic number of its constituents and its high density leading to a good stopping power for high energy

rays. Moreover, due to their intrinsic character, the optical and scintillation properties of commercial BGO are independent of the specific supplier, making it one of the most reliable standard scintillator materials. The intrinsic emission of BGO is peaked at 480 nm and exhibits a decay time of ∼300 ns at room temperature, with absolute light output (defined as the number of photons emitted in one microsecond time window after the absorption of one gamma photon) close to 9000 ph/MeV [145]. The emission from the SCSF-3HF plastic scintillator is peaked at 534 nm with decay time of ∼7 ns and light yield of 8500-10500 ph/MeV) [153].

In agreement with Figure 3.5f the radioluminescence spectrum of both nanocomposites is dominated by the emission of **1** with a minor contribution by the NCs in the blended case, possibly due to some residual phase separation. Crucially, the radioluminescence of the hybrid nanocomposite in nearly 30-fold more intense than that embedding pure **1**, which quantitatively demonstrates the effectiveness of the high-Z sensitization strategy. Even more remarkably, the radioluminescence intensity of such a nanocomposite is comparable to that of the commercial BGO crystal and plastic scintillator. Considering the very fast decay time of the nanocomposite emission (as discussed later in more detail) and assuming that no significant slow scintillation tails are present, this suggests that the light yield of the NC:**1** PMMA nanocomposite should be comparable to ∼9000 ph/MeV of the two commercial counterparts. It worth noticing that, with respect to the commercial plastic scintillator based on the green-emitting 3-hydroxyflavone molecule, the NC:**1** PMMA nanocomposite has the technological advantage that efficient and fast scintillation (see below) is obtained in the red spectral region, where common scintillation crystals, such as BGO, LYSO or LuAG are fully transparent. This opens to the possibility of realizing heterostructured detectors simultaneously featuring fast-timing and calorimetric ability, by coupling nanocomposites presented here to massive scintillation crystals [120], without optical losses due to reabsorption of the red scintillation light. To test the long-term stability of the nanocomposite scintillator, the side-by-side radioluminescence measurements are repeated on the same sample as in Figure 3.6a after storage in air for over six months. The radioluminescence spectra reported in the bottom panel of Figure 3.6a show essentially identical performance as a freshly made nanocomposite indicating no degradation of the material. In addition to shelf stability, the radioluminescence performance of the nanocomposite scintillator is stable over time also under continuous X-ray irradiation. This is shown in Figure 3.6b where is reported the spectrally integrated radioluminescence intensity vs. irradiation time for increasing dose rate. Even for high total absorbed dose of over 800 Gy, the radioluminescence intensity retains

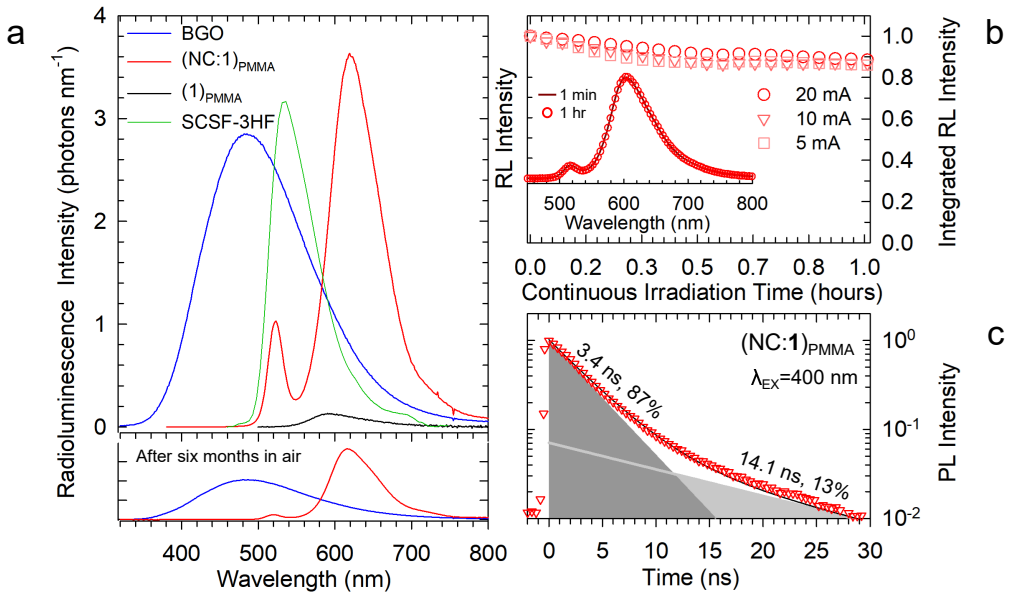

Figure 3.6: ***a)*** *Radioluminescence spectra of two PMMA nanocomposites containing either pure 1 (0.15 wt%, black line) or a binary mixture of* ***1*** *and CsPbBr3 NCs (0.15 wt% and 2.0 wt%, respectively, red line) under X-ray irradiation (30 kV, 20 mA). The radioluminescence spectra of a high quality commercial BGO crystal (grown by the Bridgman technique at the Shonan Institute of Technology, blue line) and of a plastic scintillator (Kuraray, SCSF-3HF, green line), collected in the same excitation and collection geometry. The radioluminescence intensity of the CsPbBr3–****1****–PMMA nanocomposite is comparable to that of the commercial scintillators under low-energy X-ray excitation. Bottom panel, radioluminescence spectra of the same sample after storage in air for six months compared to the same BGO crystal, showing comparable performance to the as-made nanocomposite.* ***b)*** *Integrated radioluminescence intensity of the same hybrid NC–****1****–PMMA nanocomposite as in 'a', measured for up to one hour of continuous X-ray irradiation at increasing dose rates (20 kV, I = 5 mA, 10 mA, 20 mA) corresponding to total absorbed doses of* 2.3×10^2, 4.1×10^2 *and* 8.1×10^2 *Gy (calibration performed using crystalline quartz as the absorbing medium). Inset: normalized radioluminescence spectra collected for the largest dose rate after one minute and one hour of continuous exposure, showing no variation of the RL profile.* ***c)*** *Photoluminescence decay curve at 605 nm of the same sample as in 'a' under selective NC excitation at 400 nm. The fitting curve to a double exponential decay function is shown as a black line, with lifetimes* τ_1 *= 3.4 ns (87% of the signal) and* τ_2 *= 14.1 ns (13% of the signal).*

>85% of the initial value for continuous irradiation as long as one hour, and the radioluminescence spectrum shows no modification upon prolonged X-ray exposure (Figure 3.6b, inset). It can be further noticed that the radioluminescence trend is independent on the dose rate and shows saturation of the signal in approximately 25 minutes, after which it remains constant. This suggests that the effect could be due to fast activation of traps rather than to degradation of the material.

The emission of scintillation light has been also evaluated for charged alpha par-

ticles. In these experiments, the same PMMA nanocomposites used for the radioluminescence experiments described above were faced to a 6×6 mm^2 Si photomultiplier (SiPM) composed of 14400 single pixels. When photons interact with this device, a number of cells proportional to the number of photons are activated, resulting in a current signal proportional to the number of activated cells. An operational amplifier converts this anode current into a voltage which enables one to evaluate the number of activated SiPM cells and thereby to quantify the number of detected photons. After performing calibration measurements described in the Methods section 3.2.2, the PMMA nanocomposites were faced towards the SiPM surface. To excite the light emission, two sources of ionizing radiation have been used. The first is a ^{241}Am source that emits alpha particles with energy of 5.5 MeV. It also emits X-rays with energies ranging from 11 to 26 keV and γ-rays of 60 keV, but since the probability of interaction for alpha particles is much higher with respect to X- and γ-rays, the scintillation signals detected were ascribed to the alpha particles interacting with the nanocomposite. Were also used ^{224}Ra and its radioactive daughters, as described in Section 3.2.2. The energies of the alphas emitted in the decay of such implanted nuclei range from 4 to 10 MeV. As a result, is measured a maximum light emission of 1000 photons per alpha event. Knowing that the alpha maximum energy was 10 MeV and that the total efficiency of light collection of the system is ∼13%, a light emission of at least 1000 ph/MeV for alpha particles can be evaluated.

A further relevant aspect of our systems is the very fast emission lifetime exhibited by **1** upon sensitization via the NCs. This is shown in Figure 3.6c, where is reported the photoluminescence decay curve of the 605 nm emission by the same NC:**1** hybrid PMMA nanocomposite as in Figure 3.6a under selective UV excitation of the NCs at 400 nm, which is significantly above the bandgap of the NCs. The kinetics of the sensitized luminescence is double exponential with fast component with lifetime τ_1 = 3.4 ns accounting for over 85% of the signal (consistent to the photoluminescence lifetime of pure **1** in PMMA, Figure 3.5d) followed by a slower decay with lifetime τ_2 = 14.1 ns responsible for the remaining luminescence. The decay time of the dominant fast emission is definitely faster than that characteristic of 5d-4f allowed radiative transitions of Ce or Pr ions in different hosts (of the order of tens of ns) [115]. Among presently known fast scintillators with decay time comparable or lower than 1 ns, cross-luminescent materials like BaF_2 have poor efficiency and moreover their emission lies in the UV region, where detectors quantum efficiencies are low [154, 155]; the same considerations hold for Cerenkov emitters. On the other hand, $PbWO_4$, an intrinsic scintillator emitting in the visible which became very popular due to its applications

in high energy physics [146], has decay time of a few ns, but the emission is strongly quenched and of very poor efficiency, preventing the use of this material in applications different from high energy physics. Therefore, the fast timing observed here together with the radioluminescence data in Figure 3.6a and 3.6b indicate that our hybrid nanocomposite scintillators effectively combine efficiency and operational stability with strong interaction with ionizing radiation and a fast emission kinetics.

Scintillator Prototype

Finally, to experimentally validate our strategy for mitigating reabsorption losses in large size plastic scintillators, the team fabricated prototype devices (0.5 cm × 0.7 cm × 15 cm) that utilize our hybrid PMMA nanocomposite ([**1**]= 0.155 *wt*%, [NC]=2.0 *wt*%) as active layer (thickness 300 μm) on top of an optical grade PMMA waveguide.

Figure 3.7a presents photographs of one of these devices under room (top) and near-ultraviolet (inset) illumination at 400 nm; the latter image illustrates how the photoluminescence of **1** sensitized by the NCs on one end of the PMMA slab is guided towards its other end. Figure 3.7b shows the absorption spectrum of the waveguide measured for light incident at a normal angle onto the nanocomposite layer. The same figure also presents radioluminescence spectra collected at one of the waveguide edges (0.7 × 0.5 cm^2) using identical X-ray excitation as that used for the measurements in Figure 3.6a with the irradiated spot positioned at different distances d from the device edge. In order to evaluate the losses caused by reabsorption without parasitic contributions due to photon escape, the spectra are normalized to their low energy amplitude at ∼640 nm, so that the spectral distortion of the radioluminescence directly accounts for light reabsorption by the active layer and the polymer waveguide. The calculated emission spectra obtained using Monte Carlo ray-tracing simulation are reported in Figure 3.7b and nearly perfectly resemble the experimental data. In these calculations, we specifically used the absorption and emission profiles of the NC:**1** blend as well as the photoluminescence efficiency of **1** ($\Phi_{PL,1}$ = 78±5%) embedded into the nanocomposite. As expected, given the very small spectral overlap between the absorption profiles of the blend and the respective radioluminescence, both the experimental and the theoretical emission spectra show only a minor drop on their high-energy side. Figure 3.7c reports the integrated radioluminescence intensity extracted from the spectra in Figure 3.7a and 3.7b, which enables one to evaluate the losses due exclusively to reabsorption in our devices. The data show a small drop (∼25%) due to reabsorption in 12 cm that is faithfully predicted by the Monte Carlo ray-tracing

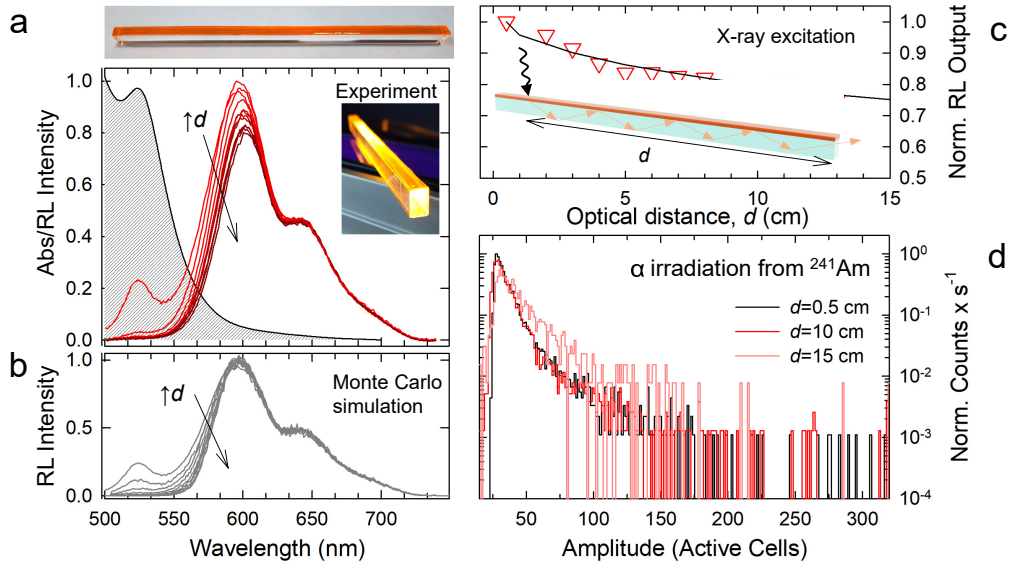

Figure 3.7: ***a)*** *Top, photograph under ambient illumination of a proof-of-concept plastic scintillator consisting of a PMMA waveguide coated with a 300-μm-thick layer of NC–**1**–PMMA nanocomposite (2.0 wt% and 0.15 wt%, respectively). The photograph of the same device under 400 nm UV illumination is reported in the inset of the bottom panel. Bottom, optical absorption spectrum (black shaded line, measured at normal angle with respect to the active layer) and radioluminescence spectra (normalized to their value at 640 nm) collected at the edge of the slab when the X-ray irradiation spot is located at increasing distances d (0.5–13 cm) from the edge, as schematically depicted in panel 'c'.* ***b)*** *Radioluminescence spectra versus d calculated through a Monte Carlo ray-tracing simulation using the absorption and emission profiles and $\Phi_{PL,1} = 78 \pm 5\%$ of the NC–**1** blend in PMMA* ***c)*** *Integrated radioluminescence intensity for the experimental (triangles) and simulated (black line) spectra. The black undulated arrow represents the ionizing radiation impinging on the device surface, the red arrows represent the propagating scintillation light.* ***d)*** *Amplitude of scintillation signals measured by a Si photomultiplier optically coupled to the edge of the scintillator waveguide when an alpha ^{241}Am source is located at different distances, d, from the waveguide edge.*

simulation, which further suggests that the emission quantum yield of **1** is preserved under X-ray irradiation. As a final demonstration of the potential of this approach, the light output of our device has been measured by coupling to a calibrated Silicon photomultiplier under irradiation by 5.5 MeV α-particles emitted by ^{241}Am source positioned at increasing d from the device edge. Figure 3.7d reports the amplitude of the scintillation signals evaluated as the number of SiPM cells that detect a light signal simultaneously. The independence of the spectral shape from d confirm essentially reabsorption-free waveguiding of scintillation light. I wish to point out that the absence of the full energy alpha peak in Figure 3g can be ascribed to several factors, among

which the most important are the non-uniform concentration of the NCs within the active layer and the partial loss of the alpha kinetic energy in air before hitting the active layer.

3.2.4 Conclusions

Here is realized and presented the first example of efficient, fast and nearly reabsorption-free plastic scintillator using $CsPbBr_3$ perovskite NCs as high-Z sensitizers for a fast emitting organic dyad featuring a large Stokes shift between its absorption and luminescence spectra that ensures minimal reabsorption losses. Plastic nanocomposites embedding individual and blended systems are fabricated using PMMA as host material. Efficient sensitization by the NCs is demonstrated in solution under selective optical excitation and, most crucially, in the PMMA nanocomposites under X-ray irradiation resulting in nearly 30-fold enhancement of the sensitized radioluminescence intensity with respect to the dyad alone. Remarkably, such a performance is comparable to the emission by commercial scintillators (a $Bi_4Ge_3O_{12}$ crystal and a SCSF-3HF plastic scintillator) under X-ray excitation, as highlighted by side-by-side radioluminescence experiments. Finally, prototype devices were fabricated and tested by depositing an active layer of our hybrid nanocomposite on top of an optical grade PMMA waveguide. Light propagation measurements under X-ray excitation, corroborated by Monte Carlo simulations demonstrate minimal reabsorption losses for large size device. This capability is confirmed by scintillation waveguiding measurements using ^{241}Am isotopes as a source of α-particles, experimentally demonstrating the ability of our test-bed device to effectively detect charged particles with nearly no reabsorption losses.

3.3 Understanding Trapping Processes in LHPs with Different Dimensionality

I start this chapter discussing the limiting factors affecting the scintillation efficiency in LHPs and possibly unlock their full potential in radiation detection or conversion schemes. This is done by combining PL and RL experiments as a function of temperature (T), side-by-side to thermally-stimulated luminescence (TSL), and low-temperature AG measurements to investigate the trapping and detrapping processes involved in the scintillation of $CsPbBr_3$ perovskite nanostructures of increasing dimensionality, namely NCs, nanowires (NWs), NSs, along with the respective BSC. In order to explore the role of surface and bulk defects through control of the surface-to-volume ratio (S:V), with minimal spurious effects due to particle quantum confinement, nanostructures larger than the excitonic Bohr radius of $CsPbBr_3$ ($a_B = 3.5$ nm) have been specifically selected. [107] RL experiments between 10 and 320 K revealed the emergence, for $T < 70$ K, of an intragap luminescence band due to radiative recombination of excitons in shallow traps in any of the investigated systems. Continuous-wave (CW) and time-resolved PL experiments showed comparable emission trends, indicating that X-ray irradiation does not produce photo-generated defects in any LHP system and pointing to the thermal exchange between shallow trapped and BE excitons. Differently from RL and PL experiments where the investigated timescale is comparable to the lifetime of the BE excitons, TSL and AG allow to probe the delayed-emission of detrapped carriers from deep centers and, notably, also the dynamics of non-radiative traps, thus providing a complementary experimental tool to RL and PL for a comprehensive analysis of the trapping and detrapping processes in both deep and shallow trap states. TSL and AG experiments at cryogenic temperature revealed a strong correlation between the system dimensionality and the detrapping mechanism from deep non-radiative traps. Specifically, the TSL glow curve of the BSC - and similarly, but with lower intensity for the NWs and NSs - shows an intense peak at $T = 112$ K marking the thermal activation of exciton detrapping which is not observed in the lower dimensional NCs. Finally, AG measurements at $T = 10$ K combined with TSL shed light onto the nature of the prolonged TSL decay common to all investigated LHP materials whose emission energy matches the low-T intragap RL and PL, revealing that in all nanostructures the main detrapping pathway is a-thermal tunneling towards a trapped excitonic state. Altogether these results point out that, despite their defect tolerant band structure, [133] the BE exciton/carriers in LHPs are substantially im-

pacted by traps that are likely associated with surface defects. In addition to that, lowering the S:V ratio leads to a progressive emergence in NWs and NSs of the signatures of a deep localized state possibly placed inside the particle volume that becomes the dominant trapping channel in BSC. Such a deeper understanding of the defect physics in LHPs offers valuable guidelines for future realization of efficient LHP based radiation detectors.

3.3.1 Samples Description

All samples have been synthetized in the laboratories of the *Istituto Italiano di Tecnologi*a (IIT) in Genoa (IT) with the collaboration of Dr. Liberato Manna's research group. Specifically, the $CsPbBr_3$ NCs were synthesized by a colloidal procedure similar to the one reported by Protesescu et al. [107] $CsPbBr_3$ NWs were synthesized by a colloidal procedure reported in Ref. [108] with the difference being that the synthesis was carried out in air and without any pre-dried chemicals or solvents. Rectangular $CsPbBr_3$ NSs were synthesized by an evolution of the synthesis reported by Shamsi et al. [109]; a 4 mL $PbBr_2$ solution (0.725 g of $PbBr_2$ were dissolved in 10 mL of 1-octadecene (ODE) together with 5 mL of oleylamine (OLA) and 5 mL of oleic acid (OA) at 100 °C) was mixed with 2 mL of ODE and 0.5 mL of an as-prepared Cs-OA precursor (325 mg of Cs_2CO_3 dissolved in 5 mL of OA by a heat gun).

After adding 250 µL of 2-propanol (IPA), the solution was stirred using a vortex for 30 s. Then the turbid greenish solution was transferred to a glass Petri dish and placed in the microwave oven (Panasonic NN-E201WM) at high power (700 W) for 5 min. Next, the reaction mixture was slowly cooled to room temperature by the water bath. To collect the NSs, 3 mL of toluene was added to the crude solution; then the mixture was centrifuged at 2000 rpm for 4 min. After centrifugation, the supernatant was discarded and the NSs were redispersed in 3 mL of toluene. $CsPbBr_3$ single crystals were grown following the work by Saidaminov et al. [156] Typically, CsBr (3 mmol) and $PbBr_2$ (6 mmol) were stirred in dimethyl sulfoxide (DMSO) (3 mL) for one hour. Then the solution was filtered and the filtrate was transferred into a vial that was placed in a heating metallic block at 60 °C. The temperature was gradually increased. Upon reaching 100 °C, undesired yellow and orange crystals appeared. The solution was filtered, and the filtrate was transferred into a new vial preheated at 100 °C, and left undisturbed for 3 h. The formed crystals were washed with hot DMSO.

In all nanostructures, the particle dimensions are larger than the exciton Bohr radius of $CsPbBr_3$ (a_B = 3.5 nm), [107] resulting in a weak quantum confinement

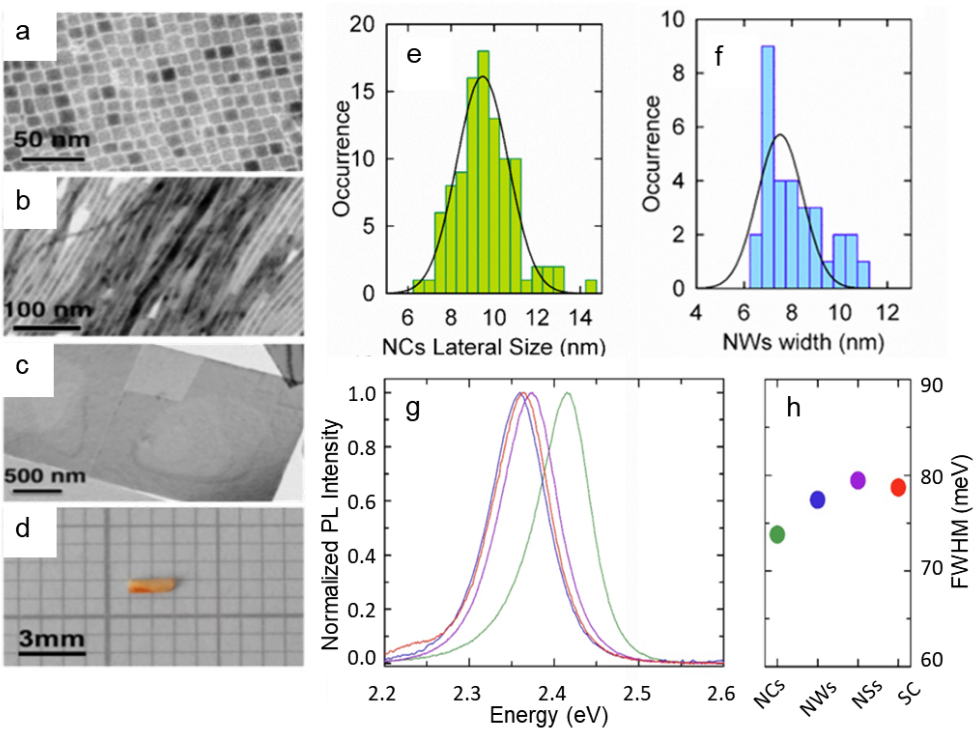

Figure 3.8: *Transmission electron microscopy images (TEM) of $CsPbBr_3$* ***a)*** *NCs,* ***b)*** *NWs and* ***c)*** *NSs together with* ***d)*** *a picture of the investigated SC. Statistical analysis of* ***e)*** *the lateral size of 100 NCs and* ***f)*** *the width of 30 NWs. The black curves are the results of the fitting procedure with Gaussian curves.* ***g)*** *Normalized PL spectra of NCs (green), NWs (blue), NSs (purple) in toluene solution together with the PL spectrum of the SC and* ***h)*** *respective FWHM values.*

effect. Specifically, the average lateral size of the NCs is 9 ± 2 nm, the NWs are 11 ± 1 nm wide and over 500 nm long and the NSs are 20 ± 2 nm thick with lateral size up to 1 μm, as extracted from the transmission electron microscopy (TEM) images (Figure S1, Supporting Information). Accordingly, the PL spectra at 300 K of all nanostructures in toluene solution (Figure 3.8) are characterized by an almost negligible blue-shift of the PL peak with respect to the BSC (∼2.38–2.42 eV vs ∼2.36 eV), featuring the characteristic narrow full width at half maximum (FWHM) values (< 80 meV) typical of $CsPbBr_3$ perovskite materials. [107] The PL quantum yield (Φ_{PL}) of the NCs, NWs, and NSs amounts to 10±2%, 10±2%, and 20±4% respectively. The BSC shows Φ_{PL} < 1%, consistent with the large exciton diffusion length in perovskite single crystals leading to a more dominant effect of nonradiative trapping compared to nanostructures. Excluding quantum confinement effects allow one to focus on the impact of the S:V by decreasing the dimensionality of the systems. Specifically, moving from the BSC, where the effect of the surface is negligible (S:V = 6×10^{-6} nm^{-1}) to the NSs (S:V

$= 2 \times 10^{-3}$ nm^{-1}) the contribution of the surface becomes dominant in NWs (S:V = 0.1 nm^{-1}) and NCs (S:V = 0.7 nm^{-1}).

3.3.2 Experimental Details

Spectroscopic Studies

For the optical and radiometric measurements, the nanostructures were processed into films of comparable thickness (∼5 µm) by drop-casting solutions of the same concentration. The thickness or the BSC was ∼ 0.5 mm. The PL were excited at 3.06 eV using a pulsed diode laser and the emitted light was collected with a charged coupled device. Time-resolved PL was collected with a time resolution of ∼600 ps. Nanostructured $CsPbBr_3$ crystals were deposited on a silica substrate by drop-casting from diluted toluene solutions. Temperature-controlled PL measurements were performed by mounting the samples in the variable temperature insert of a split-coil cryo-magnet with direct optical access. Φ_{PL} measurements were carried out in an integrating sphere by exciting the sample with a CW diode laser at 3.1 eV. A detailed description of the apparatus is reported in Section 2.2.2.

Ionizing Radiation Measurements

The samples were exposed to ionizing radiation using an X-ray tube operated at 30 kV and 30 mA, as described in Section 3.2.2. The penetration depth of the X-rays used in the experiments was approximately 2 μm (considering an attenuation factor of 5600 cm^{-1} at the employed energy), which was lower than the thickness of any of the samples. Therefore, reabsorption effects were considered to be comparable for all investigated systems.

Thermally-Stimulated Luminescence and After Glow Measurements

Wavelength-resolved Thermally-Stimulated Luminescence (TSL) at cryogenic temperatures are carried out by using the same detection system as for RL measurements. Cryogenic TSL measurements are performed in the 10-300 K interval, with a heating rate of 0.1 K/s, after X-ray irradiation up to 450 Gy for casted $CsPbBr_3$ films or bulk SC. The dose values for X-ray irradiations were obtained by comparison with a calibrated ^{90}Sr-^{90}Y beta radioactive source and using optically stimulated luminescence emission from quartz crystalline powder (100-200 μm grains). Wavelength-resolved

AG measurements are carried out by monitoring the luminescence emission at constant temperature ($T = 10$ K) as a function of the delay time after the suppression of the X-ray irradiation: the samples are irradiated with the same doses used for TSL experiments. The relative trap density is extracted from the TSL measurement, acquired in the same experimental conditions for all the samples, by normalizing the TSL glow curve for the LY dependence on temperature of different samples: this procedure allows to isolate the contribution of traps to the TSL signal from the contribution due to the temperature-dependent recombination efficiency of emissive centers. The *initial rise method* is used for the evaluation of the trap depth energy (ΔE_T). When the initial rising portion of the TSL glow curve is displayed against T^{-1}, an exponential behavior is expected due to the Arrhenius-like dependence of the TSL signal versus temperature at the beginning of the trap emptying. The thermal energy of the trap level can thus be evaluated by the expression

$$I(T) = I_0 e^{-\frac{\Delta E_T}{k_B T}} \tag{3.1}$$

where $I(T)$ is the TSL intensity, and k_B the Boltzmann constant [156,157]. The above equation is an approximation of the more complex relation between TSL intensity, temperature, and trap parameters, which is valid in the initial portion of the glow peak (up to ∼10% of the maximum intensity). The lifetime of a trap, responsible for the delayed emission, can be calculated with the formula

$$\tau_T = \frac{1}{s} e^{-\frac{\Delta E_T}{k_B}} \tag{3.2}$$

where s is the frequency factor that is related to the temperature of the maximum TSL peak T_M and to the heating rate β by

$$s = \frac{\beta \Delta E_T}{k_B T_M^2} e^{\frac{\Delta E_T}{k_B T_M}} \tag{3.3}$$

3.3.3 Results

Temperature-Controlled Radioluminescence Experiments

I start the discussion with RL and PL measurements as a function of temperature for all nanostructures and the BSC. The normalized RL spectra of all systems versus T

are reported in Figure 3.9a; the respective PL spectra are shown in Figure 3.10a for the NCs and Figures S3–S5, Supporting Information, for the other samples.

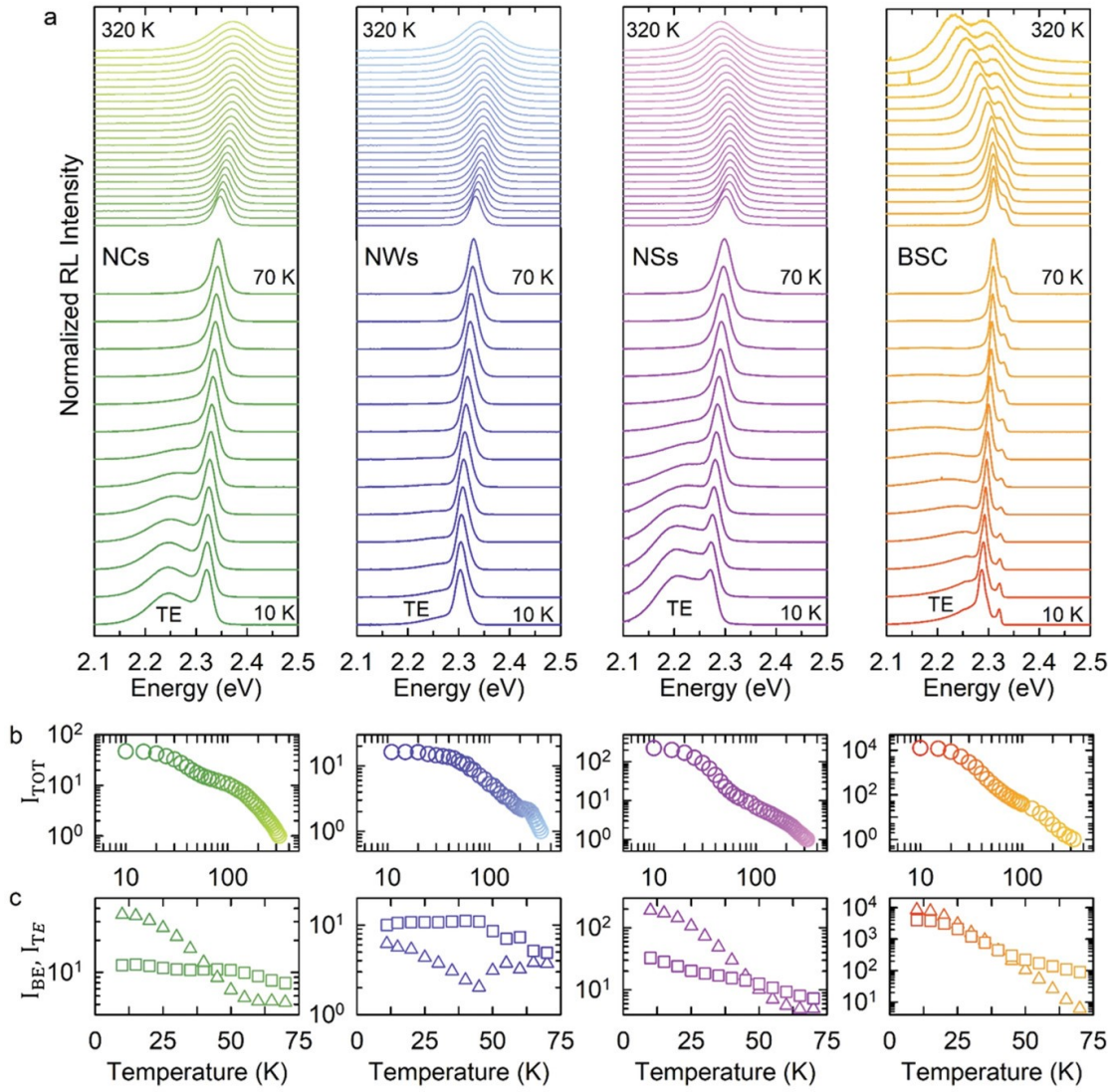

Figure 3.9: *RL of $CsPbBr_3$ nanostructures and single crystal.* **a)** *Normalized RL spectra as a function of temperature from 10 (bottom) to 320 K (top) for $CsPbBr_3$ NCs (green), NWs (blue), NSs (violet), and BSC (orange). The curves have been offset for clarity.* **b)** *Total integrated RL intensity (I_{TOT}) as a function of temperature and* **c)** *weight of the BE (I_{BE}, squares) and TE (I_{TE}, triangles) integrated RL intensities calculated with respect to I_{TOT}. I_{BE} of the BSC takes into account the evolution of both spectral components detected at room-T. I_{TOT} is normalized to its value at 320 K. All samples were excited by a continuous distribution of X-rays produced by Bremsstrahlung with maximum energy at 32 keV.*

At room temperature, all nanostructures show a single RL peak (at 2.37, 2.35, and 2.30 eV for NCs, NWs, and NSs respectively) due to the recombination of BE excitons nearly matching the respective PL excited at 3.06 eV. The BSC shows a single peak PL

(Figure S2, Supporting Information) and a structured RL (Figure 3.9d) profile with two spectral components respectively at 2.23 and 2.29 eV, consistently with previous reports on lead-based perovskite BSCs and thin films with different compositions of the A-site cations. [95, 130, 158–163] To date, no general agreement on the nature of such spectral structure has been reached in the literature. Possible origins include biexciton recombination, [159] phonon replica, [161] bulk versus surface recombination, [95, 162] re-absorption and selfabsorption effect, [158, 163] and recombination of exciton bound to a halide vacancy. [160] More recently, this effect has been assigned to polar distortion of the $PbBr_6$ octahedrons at high temperature, giving rise to indirect tail states below band-gap due to dynamical Rashba splitting effect. [159]

Upon reducing the temperature, for all systems, is observed a progressive spectral narrowing (25–90 meV) of the excitonic peak due to the gradual suppression of homogeneous broadening [127, 160, 164, 165] and the typical redshift of the exciton position at low T. [127, 165, 166] Nonetheless, whereas the exciton peak of the NCs shows monotonic redshift for $T<$ 250 K (∼50 meV from 300 to 5K), the RL of higher dimensional systems is characterized by an initial blue-shift (NWs +5 meV, NSs +19 meV, BSC + 80 meV, and +40 meV) approaching $T=$ 70 K that is overtaken by a 20–80 meV redshift at lower temperatures. Such a non-monotonic trend of the band-gap energy can be rationalized by the competition between electron-phonon coupling and temperature-induced changes in the lattice potential of LHP materials [165–167] whose effect is enhanced in higher dimensional samples. More interestingly for this study, as highlighted in Figure 3.9a, for $T <$ 70 K an additional broad (FWHM∼40–70 meV) sub-bandgap emission redshifted with respect to the BE emission peak (70 meV NCs, 59 meV NSs, 32 meV NWs, 15 meV BSC at 10 K) progressively emerges in both the RL and PL spectra of all systems, which can be ascribed to the radiative recombination of trapped excitons (TE) in a manifold of shallow traps, in agreement with previous PL [126–129] and RL [130] studies. The observation of such a TE-RL band for both the BSC and related nanostructures featuring much larger S:V suggests that similar defects are found in both the bulk and the surfaces of $CsPbBr_3$ systems. In Figure 3.9b is reported the temperature dependence of the total integrated RL intensity (I_{TOT}). The same analysis of the PL data is reported in Figure 3.10b for the NCs while, the other samples are not reported as they show essentially identical trends as the RL data for all investigated systems. In all cases, I_{TOT} grows by at least a factor of ten with decreasing temperature from 320 to 10 K.

By monitoring the BE and TE emissions separately as quantified in Figure 3.9c, where is reported the weight of their RL integrated intensity (I_{BE}, I_{TE}), can be noticed

that for all systems, the BE emission grows and reaches saturation when the temperature is decreased from 320 to 70 K. On the other hand, for $T < 70$ K the increase of I_{TOT} is mostly due to the growth of the TE-RL intensity, which becomes the dominant contribution in the case of NCs, NSs, and BSC. The NWs follow a similar trend as the other systems, although with a markedly lower contribution by the TE at low T.

Temperature-Controlled Steady-state and Time-Resolved Photoluminescence Experiments

To understand the origin of the thermal behavior of the BE and the TE recombination channels, I performed CW and time-resolved PL experiments in the 5–300 K temperature range. Since all investigated $CsPbBr_3$ systems showed very similar PL versus T trends, I focused my discussion on the NCs as a representative example.

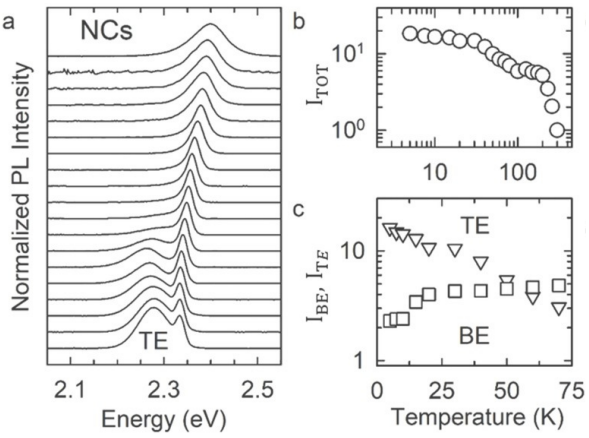

Figure 3.10: *CW and time-resolved PL of $CsPbBr_3$ NCs between 5 and 300 K.* ***a)*** *PL spectra as a function of temperature from 5 (bottom) to 300 K (top).* ***b)*** *Total integrated PL intensity (I_{TOT}) as a function of temperature and* ***c)*** *weight of the BE- (I_{BE}, squares) and TE- (I_{TE}, triangles) integrated PL intensities between 5 and 70 K.*

In Figure 3.10a is reported the PL spectra of the NCs between $T = 5$ K and $T = 300$ K. Consistent with the RL data, the room temperature PL spectrum is dominated by the BE emission at 2.4 eV. Upon cooling, the PL gradually intensifies (Figure 3.10b), and the PL spectrum undergoes very similar narrowing and redshift as observed for the RL. For $T < 70$K, a broad TE emission identical to the RL shown in Figure 3.9a arises and becomes progressively dominant, as quantified in Figure 3.10c where is reported the weight of the BE- and TE-PL integrated contributions. The close match between the PL spectra and the respective RL profiles, as well as the trends of their intensity versus T, indicate that the shallow defects responsible for the TE emission were not generated upon X-ray irradiation.

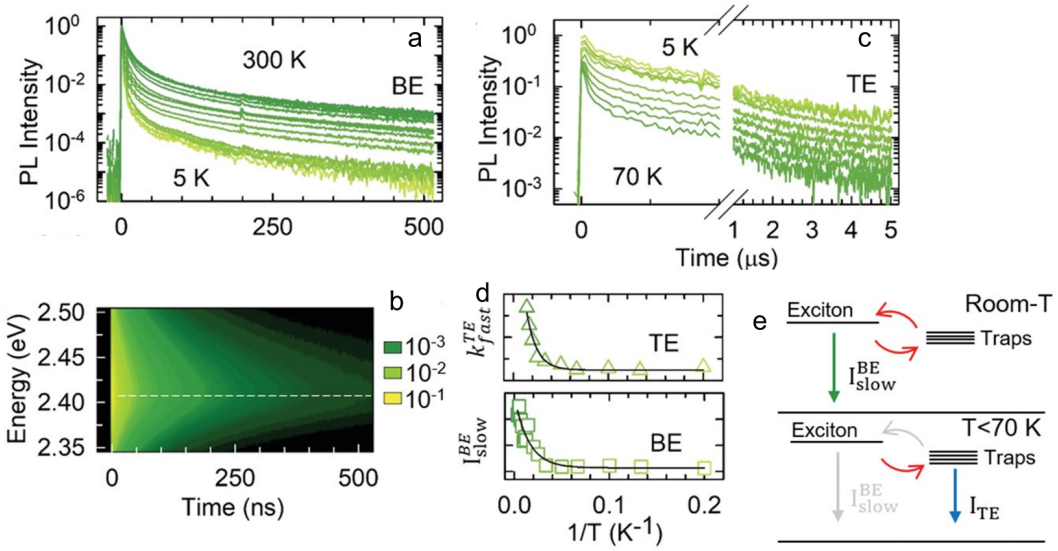

Figure 3.11: ***a)*** *Normalized PL decay curves of the BE-PL as a function of the temperature from 300 to 5 K.* ***b)*** *Contour plot of the spectrally-resolved BE-PL decay at 300 K.* ***c)*** *TE-PL decay curves as a function of the temperature between 5 and 70 K. PL decay curves are collected at BE- and TE-PL maxima. The data are normalized for the time zero TE-PL intensity at 5 K.* ***d)*** *Temperature dependence of the decay rate of the fast TE-PL component (k^{TE}_{Fast}) and the relative weight of the slow component of the BE-PL decay curves (I^{BE}_{Slow}), together with their respective fit using Equations 3.4 and 3.5.* ***e)*** *Schematic depiction of the T-dependent dynamics. At room-T the TE can repopulate the BE via thermally assisted detrapping, giving rise to a delayed component in the BE-PL emission I^{BE}_{Slow} (green arrow). For $T < 70$ K, the detrapping is progressively inhibited leading to the direct emission from the TE states I_{TE} (blue arrow) and consequent decrease of I^{BE}_{Slow}. All samples were excited at 3.06 eV.*

In Figure 3.11a is reported the PL time-decay curves of the BE between 5 and 300 K, showing a fast component with effective lifetime $\tau^{BE}_{Fast} = 6$ ns (accounting ∼80% of the signal at room temperature) followed by a long-lived tail with decay time $\tau^{BE}_{Slow} \sim 150$ ns. In order to clarify the origin of the delayed-PL, in Figure 3.11b is reported the contour plot of the spectrally-resolved PL-decay of the NCs at 300 K, showing essentially the same emission profile over the entire decay time and thus confirming that the fast and the long-lived component originate from the same exciton state. Notably, the fast component of the BE progressively accelerates with decreasing temperature according to the bright nature of the triplet excitonic states in LHP nanostructures, [167] in stark contrast to τ^{BE}_{Slow} that remains essentially constant throughout the whole temperature range. Consistent with previous reports, [91, 143] the fast component of the PL decay can be ascribed to recombination of photoexcited BE excitons and the longer-lived one to delayed emission of thermally regenerated BE excitons by detrapping from shallow-

trap states. To assess whether such trap states are also involved in the TE emission observed under both photo and X-ray excitation, I analyzed the temperature evolution of the TE decay dynamics. The TE-PL decay curves (Figure 3.11c) are featured by an initial faster contribution with lifetime $\tau_{Fast}^{TE} \sim 100$ ns at 5 K followed by a μ-second long decay component. The fast recombination channel of the TE states is assigned to the non-radiative recombination of TE by thermally assisted detrapping to the BE state, while the µ-second component corresponds to the direct radiative recombination of the TE when no transfer of carriers takes place. Accordingly, upon lowering the temperature, the decay rate of the fast TE-PL component (k_{Fast}^{TE}) drops (Figure 3.11d), in compliance with the idea of progressively inhibited detrapping by back-transfer to the BE state. Consistently, such a decrease in fast k_{TE} is accompanied by a concomitant decrease of the relative weight of the slow decay contribution of the BE-PL (I_{slow}^{BE}) due to re-populated BE excitons (Figure 3.11d), strongly supporting the picture of the thermally driven interchange taking place between the two states, as depicted in Figure 3.11e. According to this picture, I evaluated the detrapping energy E_{DT} by fitting the temperature dependence of I_{slow}^{BE} and k_{fast} TE respectively with the expressions

$$I_{slow}^{BE} = I_0 e^{-\frac{E_{DT}}{k_B T}} \tag{3.4}$$

$$k_{fast}^{TE} = k_0 + k_1 e^{-\frac{E_{DT}}{k_B T}} \tag{3.5}$$

both consistently yielding E_{DT} = 6–8 meV. The same analysis carried out for the NWs (not reported in figure) leads to an activation energy of only 2 meV, suggesting that even at cryogenic temperature the detrapping is highly efficient in this system. This aspect could originate from the peculiar behavior of NWs to merge into larger structures, affecting the coordination of surface sites and defects, and could explain the lower contribution of the TE emission in NWs compared to the other samples. Finally, I point out that the energy shift between the BE-PL and the TE-PL at 5K (∼50 meV) is much higher than the activation energy of the back-transfer, suggesting that the radiative recombination of TE takes place from the bottom of a manifold of states.

Thermally Stimulated Luminescence and Low-T After Glow

Next, I procede in the analysis by performing TSL and low-T AG measurements for all investigated systems, as described in the experimental section of this chapter. TSL and AG are powerful techniques largely employed in the field of scintillation and dosimetry,

as they specifically probe the dynamics of detrapping processes from defect states. More in details, a typical TSL experiment consists of two steps. First, the sample is exposed to prolonged X-ray irradiation at a given temperature to populate trap states in the bandgap that are stable at the chosen temperature. Successively, the irradiation is interrupted, and the sample is progressively heated using a linear heating rate while monitoring the delayed emission due to carrier detrapping. This allows one to correlate the temperature at which a specific TSL peak is detected with trap parameters like trap depth (ΔE_T) and attempt-to-escape frequency (or frequency factor) s. In AG measurements, X-ray irradiation is performed analogously but the sample is kept at a constant temperature during the whole acquisition of the delayed emission.

In Figure 3.12a is reported the contour plots of the spectrally resolved TSL intensity of all investigated samples as a function of temperature. All systems exhibit a broad (1.7–2.5 eV) monotonic TSL emission extending over a wide range of temperatures. For the BSC, such a monotonically decreasing TSL signal is superimposed to an intense TSL peak emerging at 112 K. A closer look at the contour plot of the NSs and the NWs reveals an analogous, yet substantially weaker, signal emerging at $T = 112$ K. In order to resolve the spectral contribution to the TSL contour plot, in Figure 3.12b are reported the TSL spectra integrated over two temperature intervals, namely $T < 90$ K and 90 K $< T <$ 130 K. The low-T TSL spectra of all systems are substantially similar, with a main narrow peak at ∼2.25 eV that matches the TE-RL and PL discussed in Figure 3.9 and Figure 3.10. Interestingly, the BE emission is lacking in all systems while a low-energy shoulder extending to 1.5 eV (TE'), whose relative intensity increases with the system dimensionality, is detected altogether with TE above 90 K, in the region of the 112 K peak. Upon heating, TE' intensifies, with the higher dimensional system showing the largest growth, resulting in a featureless TSL spectrum at 1.9 eV dominating the spectrum of the BSC. Such features, namely the presence of a sharp peak and of an additional emission center below 2 eV, and their strong anticorrelation with S:V, suggest the existence of different trap-center recombination paths that will be discussed in detail in Figure 3.13.

Once analyzed the spectral composition of the emitting centers, I proceeded to investigate the kinetics of the detrapping mechanisms. In Figure 3.12c is reported the spectrally integrated TSL intensity as a function of the temperature (commonly referred to as "glow curves") for all investigated samples. Since in TSL experiments temperature and time are linearly correlated, one can map the decay of the TSL intensity as a function of time, as shown in Figure 3.12c. Consistent with the respective TSL contour plots, the glow curves of the nanostructures decrease monotonically with temperature

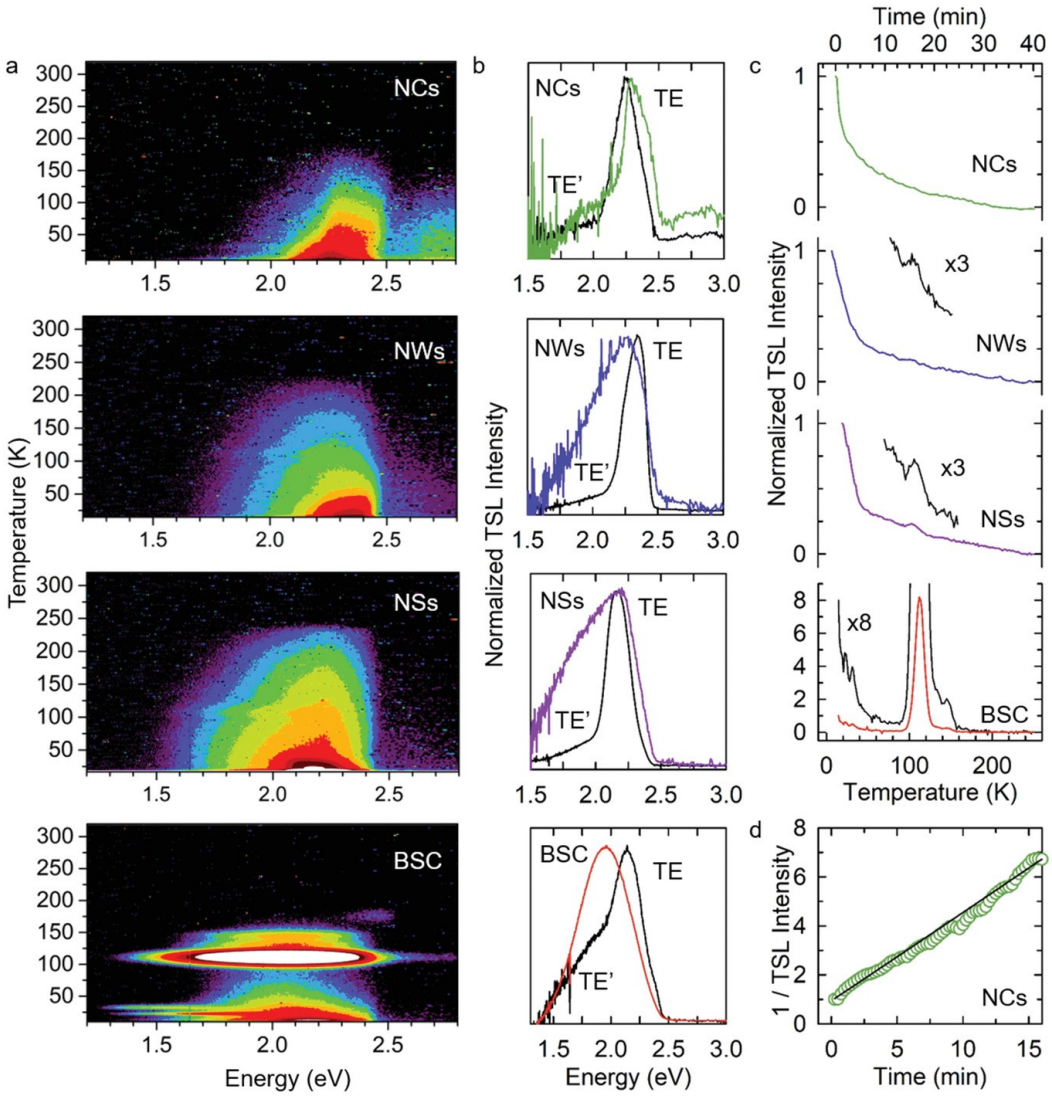

Figure 3.12: *TSL of $CsPbBr_3$ nanostructures and single crystal.* ***a)*** *Contour plots of the spectrally resolved TSL intensity as a function of temperature in the 10–320 K range of all investigated samples.* ***b)*** *Normalized spectra of the TSL intensity integrated for $T < 90K$ (black curve) and between 90 and 130 K (colored curve).* ***c)*** *Glow curves of all investigated samples normalized for their initial value at $T = 10$ K. The black insets in Figure are a magnification of the glow curve to highlight the TSL peak of NWs and NSs and the initial monotonic decay of the BSC.* ***d)*** *Inverse of the TSL intensity of NCs as a function of the time-delay after the suppression of irradiation. The black line is the result of the fitting to Equation 3.6.*

(time) and the NWs and NSs show an additional peak at 112 K (insets in Figure 3.12c), corresponding to the rise of TE' in the TSL spectra in the 90–120K temperature range. According to the above discussion, the BSC shows essentially the same monotonic behavior of the nanostructures with an additional peak at 112 K, almost ten times

more intense than the underlying TSL intensity trend, followed by a weaker peak at 135 K. The emergence of TSL peaks in glow curves is the typical signature of a thermally activated detrapping process. [157] Specifically, the rise of the TSL corresponds to the onset of carrier release from a trap. Once a significant portion of the traps has been emptied, the TSL signal starts to decrease, leading to a typical peak feature in the glow curve. Before investigating the energetics of the TSL peaks, I analyze the monotonic decay of the TSL intensity common to all samples. I choose to focus on the NCs, since no TSL peaks are detected in their glow curve. In Figure 3.12d is reported the inverse of the TSL intensity in the first 15 min after suppression of the irradiation (10–100 K), showing a clear linear trend with time. Notably, such a linear behavior is the typical signature of direct a-thermal tunneling of trapped carriers from a distribution of trap-center distances. [30, 168–170] In this case, the release of carriers is not mediated by the material bands, but it is instead due to direct tunneling from the trap state to an excited state of the luminescent center positioned at the same energy. Accordingly, data can be fitted using the expression,

$$I(t) = A(t + t_0)^{-p} \tag{3.6}$$

that yields $p = 1.01 \pm 0.06$ for NCs, in excellent agreement with a-thermal tunneling release of carriers. [169]

Moreover, in order to further confirm the presence of a-thermal tunneling, AG measurements are performed at T= 10 K on NSs and BSC, where the thermal contribution is more pronounced. In Figure 3.13a are reported the spectrally integrated TSL intensity together with the AG intensity as a function of time for the NSs and BSC. Both samples show prolonged delayed emission at constant T= 10 K, definitely proving the presence of an a-thermal detrapping channel. Accordingly, fitting the AG decays with Equation 3.6 yields p = -0.90 ± 0.01 for NSs and p = -0.99 ± 0.02 for the BSC, and the AG spectra (Figure 3.13b) show constant shape with time for both systems. Notably, the low-temperature TSL spectra (Figure 3.12b) closely resemble the AG spectra, except for the low-energy contribution responsible for the TSL peaks of the AG curves. It must be highlighted that the trap transferring via tunneling is situated at the same energy of the excited state of the emitting center, since tunneling occurs exclusively between isoenergetic states.

Finally, I focus on the energetics of the trap associated with the TSL peak at T= 112 K mostly observed for the BSC. To this aim, the AG contribution is subtracted from the glow curve of the BSC and calculated ΔE_T and its τ_T at room-T by the

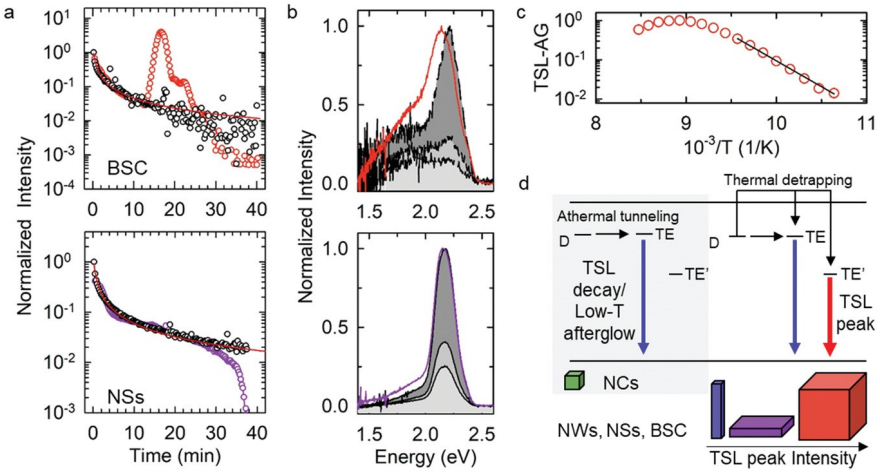

Figure 3.13: ***a)*** *TSL intensity (red and purple circles) and AG intensity (black circles) of BSC and NSs as a function of the delay-time after suppression of the irradiation, together with the fit (red lines) of the AG intensity using Equation 3.6.* ***b)*** *Low-T TSL spectra (colored curves) together with the AG spectra for increasing delay-time of BSC and NSs at t = 0, t = 1.5, and t = 3 min.* ***c)*** *Arrhenius plot and fit (black line) of the 112 K TSL peak of BSC.* ***d)*** *Schematic depiction of the detrapping mechanisms observed in TSL and AG experiments. All samples are characterized by a monotonic TSL decay (blue curve) that is assigned to a-thermal tunneling accordingly to low-T AG measurements. Such a mechanism is the unique detrapping channel in NCs, in contrast to higher-dimensional systems where an additional thermal activated detrapping mechanism takes place, leading to progressively more intense TSL emissions (red arrows) being the dominant feature in the TSL glow curve of the BSC.*

so-called *initial rise method*, as described in the experimental section 3.3.2. [157, 171] In Figure 3.13c is reported the Arrhenius plot of the TSL amplitude in the region of interest with the respective fit, leading to $\Delta E_T = 260$ meV, a value much larger than the thermal energy at room-T. Combining Equations 3.2 and 3.3 is obtained $s = 1010$ s^{-1} and $\tau_T = 2.6$ μs at room-T, a value substantially exceeding the typical exciton recombination time of LHPs. Altogether the combined use of TSL and low-T AG experiments reveals a substantial difference in the ultra-slow detrapping mechanisms of NCs compared to higher dimensional systems, as schematically depicted in Figure 3.13d. In NCs, trapped carriers are mostly released via a-thermal tunneling to the same TE state observed in RL and PL experiments, leading to a monotonic decay of the TSL intensity and AG. An additional thermal detrapping channel gives rise to a TSL peak whose intensity is progressively enhanced in NWs and NSs, becoming the dominant feature of the TSL of the BSC. At variance with tunneling, characterized mostly by the selective TE emission, thermal detrapping brings carriers in delocalized states from which they can recombine evenly at two emission centers, namely TE and TE' responsible for the low energy band below 2 eV. The presence of a TE' below 2 eV

also at 10 K might be due to weak thermal liberation of traps also at this temperature, which is obviously strongly enhanced when the temperature gets close to 112 K. The observed sharp decrease of the TSL just after the TSL peak at 112 K (see Figure 3.13) suggests that the same kind of trap is responsible for both a-thermal tunneling and TSL peak at 112 K, this last peak representing the thermally-assisted liberation of carriers leading to their complete depletion. Due to the much stronger dependence of trap-center distance in tunneling phenomena with respect to thermally assisted ones, the more pronounced relative intensity of tunneling with respect to thermal liberation in nanostructures with respect to BSC points to a greater spatial correlation between traps and emission centers in nanostructures, that are more defective due to their high $S:V$. Finally, such a picture even suggests the possibility to probe the defectivity level of nanostructures prepared by different synthesis methods by monitoring the relative weight of tunneling with respect to thermal liberation in TSL recombination.

3.3.4 Conclusions

In summary, it has been performed a comparative and in-depth investigation of the trapping and detrapping mechanisms of excitons in $CsPbBr_3$ perovskites of increasing dimensionality. The results reveal that all systems show detrapping physics related to shallow localized states due to surface defects. RL and PL measurements at various temperatures shed light on the thermal equilibrium between photogenerated excitons and localized shallow states in all investigated systems leading to delayed emission due to BE re-population following detrapping. Such a detrapping process is characterized by a thermal onset of a few meV (5.6 meV for NCs), leading to direct emission from the TE for $T<$ 70K and resulting in a broad intragap RL and PL at low T. Interestingly, I further observe a prolonged TSL intensity decay common to all samples. This evidence combined with AG experiments allows one to assign such a prolonged luminescence to a-thermal tunneling detrapping, that appears as the principal detrapping mechanism in $CsPbBr_3$ nanostructures. Nevertheless, for NWs and NSs a TSL peak at $T=$ 112 K emerges due to an additional temperature-activated detrapping channel from a deeper state ($\sim$260 meV) with a room temperature lifetime of 2.6 μs. Such results offer valuable insights for understanding and control of traps in the scintillation of LHP materials and highlight NCs as arguably superior candidates as scintillator materials compared to higher dimensional analogs, where the suppression of defects needs to be operated both on the surface and at a volume level.

3.4 Extreme γ-ray Radiation Hardness and High Scintillation Yield in $CsPbBr_3$ Nanocrystals

Having assessed the main trapping and detrapping mechanisms affecting the scintillation performance in $CsPbBr_3$ nanostructures, in this section I will demonstrate, for the first time, that $CsPbBr_3$ nanocrystals exhibit exceptional radiation hardness for ^{60}Co γ-radiation doses as high as 1 MGy. The scintillation efficiency is, however, found to be limited by trapping in shallow defects. Crucially, side-by-side spectroscopic and scintillation experiments coupled to thermally stimulated luminescence (TSL) and after-glow (AG) measurements indicate, in full agreement with my previous results on a different set of $CsPbBr_3$ NCs, that the scintillation emission of standard $CsPbBr_3$ NCs is dominated by shallow defects likely accumulated onto the NC surfaces and populated via a-thermal tunneling from isoenergetic trap states. Crucially, I show that post synthesis fluorination of the NC surfaces passivates such traps, resulting in scintillation process determined by band-to-band exciton recombination with high spectral purity and strongly enhanced efficiency at any irradiation dose. Interestingly, the suppression of shallow defects in fluorinated $CsPbBr_3$:F NCs unveils the presence of isolated deeper trap states, not observed in standard $CsPbBr_3$ NCs but commonly found in LHP bulk crystals featuring low intrinsic trap density [98,130,143], which give rise to an intragap TSL band activated by thermal liberation of trapped carriers. These findings therefore bridge our knowledge of the scintillation physics of massive and nanoscale LHP and demonstrate that the low trap density characteristic of LHP massive solids can be realized also in nanoscale systems. This provides valuable guidelines for highly efficient and radiation hard detection designs produced via chemical methods, which substantially strengthen the potential of LHP nanostructures in real-world radiation detection schemes for high-energy physics, nuclear batteries, as well as in space-grade solar cells where high radiation hardness is critical for successful and long-running operation.

3.4.1 Samples Description

All the NCs used in this study have been produced by the group of Prof. Liang Li from the *School of Environmental Science and Engineering*, Shanghai Jiao Tong University (Shanghai, PRC). For the synthesis of standard $CsPbBr_3$ NCs was followed a hot-injection procedure as described by Liu et. al [172]. $PbBr_2$ (0.734 g, 2 mmol), 1-octadecene (20 ml), oleic acid (5 ml) and oleylamine (5 ml) were added to a three-neck flask and degassed at 120 °C for 1 h under vacuum. The flask was then filled with

argon and heated to 180 °C until the $PbBr_2$ and dissolved completely. Subsequently, the pre-heated cesium-oleate precursor (1 ml) was injected swiftly into the flask to react for 10 s before the flask was immersed in an ice-water bath. The products were centrifuged with MeOAc and re-dispersed in toluene, and the supernatant was obtained as the $CsPbBr_3$ NC solution. So obtained NCs are stocked in dried powders form and redispersed in hexane solutions for spectroscopic investigations.

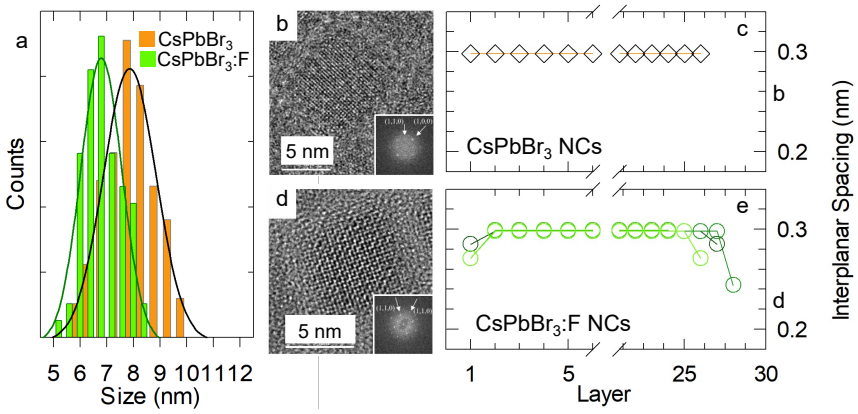

Figure 3.14: ***a)*** *Size distributions of $CsPbBr_3$ NCs (7.8 ± 0.9 nm) – green histogram – and $CsPbBr_3$:F NCs (6.9 ± 0.8 nm) – orange histogram – as extracted from Figure 3.17. Aberration-corrected STEM images and corresponding interplanar spacing vs. layer position of a $CsPbBr_3$ NC* ***(b, c)*** *and representative set of $CsPbBr_3$:F NCs* ***(d, e)****.*

For the synthesis of F-treated $CsPbBr_3$:F NCs 1:1 molar ratio of didodecyl dimethylammonium bromide (DDABr) and NaF were dissolved in toluene and ultra-pure water, respectively. These solutions were then mixed under sonication for 30 min for complete exchange of the bromide anions with fluoride anions. Subsequently, the milky-looking mixture was centrifuged and the toluene solution containing the didodecyl dimethylammonium fluoride (DDAF) precursor was obtained. A certain amount of DDAF solution was added to the $CsPbBr_3$ toluene stock solution (1 ml) with stirring for 30 min at room temperature before the mixture was centrifuged with methyl acetate. The sediment was re-dispersed in toluene for centrifugation again and then the supernatant was collected as the $CsPbBr_3$:F NCs solution before being dried and stocked as powders similarly to $CsPbBr_3$ NCs.

NC size distributions in Figure 3.14a illustrate the average size of $CsPbBr_3$ (7.8 ± 0.9 nm) reducing to 6.9 ± 0.8 nm after DDAF treatment. This is due to the formation of about one monolayer of $CsPbBr_3$:F with slightly shorter interplanar distances than the

inner particle core due to the smaller ionic radius of fluorine with respect to bromine, as highlighted by the aberration corrected scanning transmission electron microscopy (STEM) images reported in Figure 3.14. Specifically, spacing of the atomic planes in untreated NCs is constant across the whole particle section at 0.298 nm, which corresponds to the (2 0 0) direction of cubic $CsPbBr_3$ (0.2915 nm, JCPDS card no. 54-0752), while in F-treated $CsPbBr_3$:F NCs the outer NC layer contracts to 0.245∼0.280 nm approaching the interplanar distance in the (2 0 0) direction of $CsPbF_3$ (0.240 nm, JCPDS card no. 22-1075). Therefore, the outer lattice contraction can be ascribed to the presence of a fluorine-rich layer resulting from the occupation of surface bromine vacancies or even the exchange with shallow bromine ions.

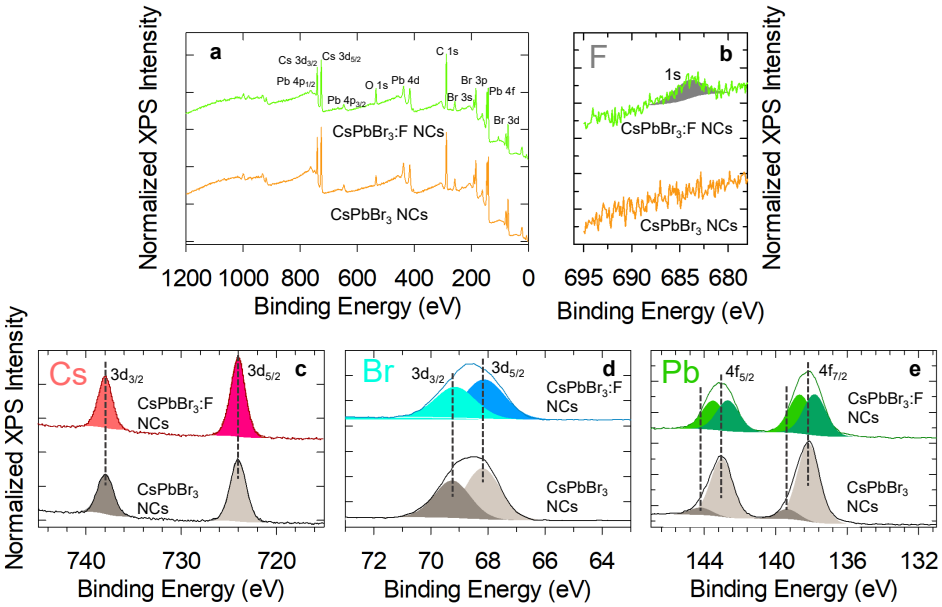

Figure 3.15: ***a)*** *XPS survey spectra of untreated $CsPbBr_3$ NCs (orange line) and $CsPbBr_3$:F NCs (green line).* ***b-e)****High-resolution XPS spectra for NC elemental constituents before and after the DDAF treatment as indicated in the panels.*

X-ray photoelectron spectroscopy (XPS) measurements corroborates the presence of a fluorine-rich surface layer on DDAF treated NCs identifying the chemical state of all elements in $CsPbBr_3$ and $CsPbBr_3$:F NCs. In Figure 3.15a are shown the XPS survey spectra of untreated $CsPbBr_3$ NCs (orange line) and $CsPbBr_3$:F NCs (green line). More interestingly, high-resolution XPS spectra in Figure 3.15b provide complementary indications to EDS measurements (discussed in Table 3.1) confirming the presence of fluorine ions in treated NCs. Similarly, the analysis of the chemical shift for the other NC elemental constituents provides valuable insights on the effects of DDAF treatment

in terms of their chemical environment and coordination after fluorine incorporation. Specifically, no significant shifts in binding energies are observed for Cs (3.15c) and Br (3.15d) 3d core levels before and after fluorination, except for a slight increase in full width at half maximum (FWHM). On the other hand, the Pb XPS spectra shown in Figure 3.15e reveal noticeable differences between standard and treated NCs. In both cases, the peaks of the Pb 4f core levels feature two components ascribable to Pb cations located on the NC surface or inner layers, respectively peaking at 143.3 eV and 138.1 eV, and at 144.6 eV and 139.2 eV. In standard $CsPbBr_3$ NCs, the contribution from outer – and possibly under coordinated – Pb cations dominates the XPS spectrum with nearly eight-fold intensity with respect to the NC core lead. After the introduction of the DDAF, the ratio between the two states of Pb changes, with the contribution of surface Pb matching that of inner Pb. This effect can be ascribed to the NC surface reconstruction with fluorine anions occupying the surface Br- vacancy sites.

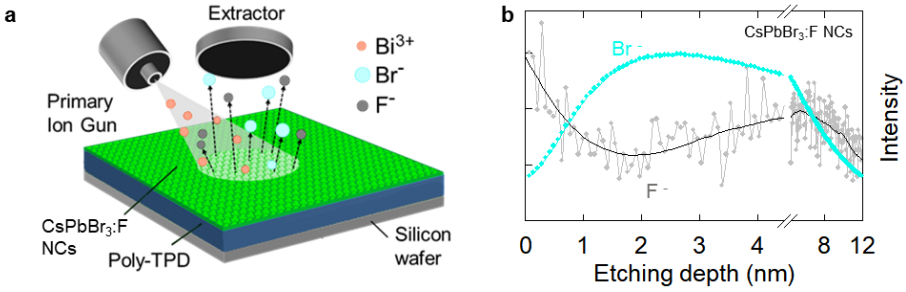

Figure 3.16: ***a)*** *Schematical representation of a time-of-flight secondary-ion mass spectroscopy setup etching a thin layer of NCs.* ***b)*** *In depth profile of fluorine and bromine anions for F-treated $CsPbBr_3$:F NCs*

Independent proof to the formation of fluorine-rich surfaces in $CsPbBr_3$:F NCs is provided by time-of-flight secondary-ion mass spectroscopy (TOF-SIMS) operating in dynamic mode. For these measurements, a nearly single particle layer (∼10 nm) of $CsPbBr_3$:F NCs is deposited onto a low-roughness Poly-TPD film and sputtered with Bi3+ primary cations, as schematically depicted in Figure 3.16a. The depth of the etching process is calibrated through Atomic Force Microscopy. In full agreement with our structural and spectroscopic analysis, the signal intensity due to fluorine ions is maximum at the sample surface and drops steeply in the first 2 nm of the depth profile in Figure 3.16b. Nearly perfect anticorrelation was found for the signal of bromine ions, which were released mostly from the inner particle layers, thus corroborating the picture that the DDAF treatment modifies the particle surfaces leaving the $CsPbBr_3$ core unaltered.

Sample	Cs/at%	Pb/at%	Br/at%	F/at%	F/Br
$CsPbBr_3$:F NCs	16.5	19.78	58.77	4.95	0.08423
	20.16	18.43	57.17	4.23	0.07399
	16.21	20.38	59.06	4.36	0.07382
	21.84	21.21	52.87	4.08	0.07717
	17.95	21.32	55.46	5.27	0.09502
Mean	**18.5±2.4**	**20.2±1.2**	**56.7±2.6**	**4.6±0.5**	**0.081±0.009**

Table 3.1: *Energy-Dispersive Spectroscopy (EDS) of $CsPbBr_3$:F NCs for the elemental analysis of Cs, Pb, Br and F. The experimental repeatability is verified by analyzing five locations within the same sample.*

3.4.2 Experimental Details

Optical Spectroscopies

Optical Absorption and steady-state PL measurements of NCs were measured in hexane solution with a Cary 50 UV–Vis and a Varian Cary Eclipse spectrophotometer, respectively. Photoluminescence quantum yield measurements were performed in an integrating sphere on non-irradiated NCs dispersed in hexane solution; the emitted light was dispersed with a spectrometer and detected with a charge-coupled device similarly to Section 2.2.2. The same solutions were spin-casted on quartz substrates and were mounted in the variable temperature insert of a closed cycle He cryostat with optical access for transient PL measurements. Time-resolved PL were carried using the setup described in Section 2.2.2 with a time resolution of ∼400 ps. The same casted NCs are mounted in a different He cryostat, equipped with an optical window and an X-ray excitation source to perform, in parallel, steady-state temperature-controlled PL and RL measurements in the 10-290 K interval. For PL studies the samples were excited by a frequency tripled pulsed Nd:YAG laser source at 3.49 eV (355 nm) operated at 10 kHz; the X-ray excitation and RL detection apparatus is the same described previously in Section 3.2.2.

Radioluminescence Measurements

The samples were excited by unfiltered X-ray irradiation tube operated at 20 kV, similarly to Section 3.2.2. Cryogenic RL measurements are performed in the 10-290 K interval. The acquisition system is the same as for temperature-controlled PL measurements. Thermally-Stimulated Luminescence (TSL), and After Glow (AG) experiments are described in Section 3.3.2.

Light-Yield Calculation

The light-yield (LY) is obtained by direct comparison of the RL response of NCs powders uniformly compacted in a cylindrical volume and commercial 1 mm thick $Bi_4Ge_3O_12$ (BGO) bulk single crystal used as reference scintillator, with a well-known LY of 8000-10000 photons/MeV [173]. The thickness of powder samples has been evaluated by direct measurements of their mass and density, with an uncertainty of ± 2 μm, and is largely greater than X-rays penetration depth, taking into account the X-ray linear attenuation coefficient of 1020 cm^{-1} at the mean X-ray energy of 7.2 keV of the continuous distribution due to Bremsstrahlung emission [174]. This approach leads to an experimental uncertainty of 30%. The temperature dependence of the LY is extrapolated from the room temperature measurement, by using the RL response curve as a function of temperature, because of the absence of any slow scintillation tail.

3.4.3 Results

Room-Temperature PL and RL Measurements

Here I start the discussion looking at the optical and scintillation properties of either standard $CsPbBr_3$ NCs and F-treated $CsPbBr_3$:F NCs at room-temperature. In agreement with previous reports [172], resurfacing does not modify the lattice electronic structure of the particle core, as testified by the XRD spectra in Figure 3.17c and the nearly identical optical absorption and photoluminescence profiles of the standard and treated NCs (Figure 3.17d,e) and substantially increases the PL quantum yield (Φ_{PL}) from 48$\pm$5% to 90$\pm$7%, owing to the elimination of carrier trapping in Br vacancies acting as electron trapping sites [172]. Consistently, the PL dynamics of $CsPbBr_3$:F NCs is substantially slower than for the standard NCs (Figure 3.17f).

Most importantly for the study, fluorine resurfacing has important benefits for the scintillation properties of LHP NCs. As shown in Figure 3.17d, the RL spectrum of the standard $CsPbBr_3$ NCs is significantly red shifted from the corresponding PL ($\sim$65 meV), indicating that in these NCs the RL originates from shallow defects (hereafter referred to as D_S) which can be directly populated by X-ray excitation. As highlighted in Figure 3.17e, the fluorine resurfacing passivates such shallow defects resulting in essentially perfect energy resonance between the RL and the respective PL peaks and in substantially increased scintillation light yield (LY). Specifically, side-by-side measurements in identical experimental conditions of X-ray excited RL of our NCs and of a commercial $Bi_4Ge_3O_12$ (BGO) bulk crystalline scintillator used as reference (LY=8000-

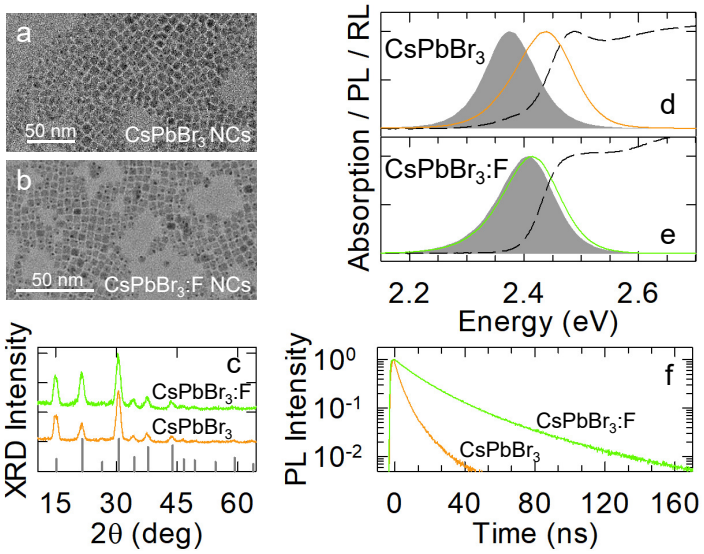

Figure 3.17: *TEM images of* **a)** *$CsPbBr_3$ and* **b)** *$CsPbBr_3$:F NCs.* **c)** *Respective XRD patterns ($CsPbBr_3$ NCs in orange and $CsPbBr_3$:F NCs in green). Optical absorption (dashed black line), PL (solid line) and RL (shaded area) spectra of* **d)** *$CsPbBr_3$ NCs and* **e)** *$CsPbBr_3$:F.* **f)** *Normalized PL decay curves measured at the respective at PL maxima for $CsPbBr_3$ NCs (orange) and $CsPbBr_3$:F NCs (green).*

10000 photons/MeV) [173] show comparable RL intensity for the BGO and the fluorinated NCs which exceed by a factor ∼6 the RL intensity of standard NCs (Figure 3.18a). Considering the fast decay time of the NCs and the absence of slow scintillation tails (see later in this section), this roughly quantifies the LY of $CsPbBr_3$:F NCs in ∼8500 photons/MeV and LY∼1500 photons/MeV for standard NCs, which makes resurfaced NCs comparable to commercial massive scintillators. We further notice that the effect of surface fluorination is larger on the LY (6-fold enhancement) than on the respective Φ_{PL} (2-fold enhancement), which is consistent with the fact that the RL in standard NCs is mostly due to shallow defects whereas the RL $CsPbBr_3$:F NCs, as well as the PL in either systems, emerge from the recombination of BE excitons.

Extreme Radiation-Hardness Measurements

As anticipated above, despite important progress in LHP-based scintillators, the stability of the LY under prolonged exposure to radiation – commonly referred as radiation hardness – has never been reported beyond a few kGy [103, 175–179]. To investigate the effects of extreme γ-ray radiation levels on both standard and surface treated

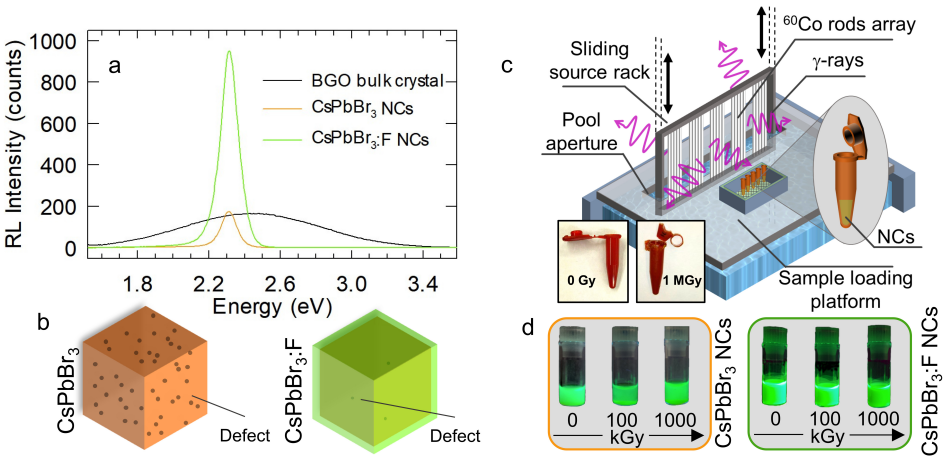

Figure 3.18: ***a)*** *RL spectra of commercial $Bi_4Ge_3O_12$ (BGO) bulk crystalline scintillator used as reference (black line), standard $CsPbBr_3$ NCs (orange line), and F-treated $CsPbBr_3$:F NCs (green line) collected in the same experimental condition as described in the Experimental section.* ***b)*** *Schematic sketch of LHP NCs before and after surface passivation with F^- anions showing almost complete suppression of surface trap states.* ***c)*** *Sketch of the pool-type γ-ray plant used to deliver radiation doses up to 1 MGy. Below, photographs of the sample vials before and after exposure to the maximum γ-ray dose showing substantial radiation damage.* ***d)*** *Photographs of $CsPbBr_3$ NCs (left) and $CsPbBr_3$:F NCs (right) in hexane solution when excited at 3.40 eV (365 nm) at three representative doses showing no appreciable variation of the PL intensity.*

$CsPbBr_3$ NCs, in collaboration with the Calliope facility (schematically depicted in Figure 3.18c), the NC powders have been exposed to uniform irradiation by a ^{60}Co γ-source at a constant dose rate of 3.40 kGy/hour and monitored their optical and scintillation properties at increasing cumulative doses up to as much as 1 MGy. Fundamentally, as shown in Figure 3.19a 3.19b (see also in Figure 3.18d), the PL and RL spectra of both the standard and the fluorinated $CsPbBr_3$ NCs are substantially identical at any γ-ray dose, indicating that the NCs retain their optical properties up to 1 MGy, even when the polypropylene vials become brittle and fragment when handled (inset of Figure 3.18c). The RL of the fluorinated and standard NCs respectively retain their BE-exciton and D_S origin independent from the delivered dose, suggesting that exposure up to 1 MGy of γ-ray does not create further defects (as further confirmed by the TSL data reported later in this chapter), and indicating that the synthetic procedures and surface passivation are the key factors in determining the presence or the absence of trapping centers in $CsPbBr_3$ NCs. For the untreated $CsPbBr_3$ NCs, it can also be noticed the progressive emergence of an absorption tail at about 2.35 eV with dose, which matches the bandgap energy (2.38 eV) of bulk $CsPbBr_3$ [180,181] and

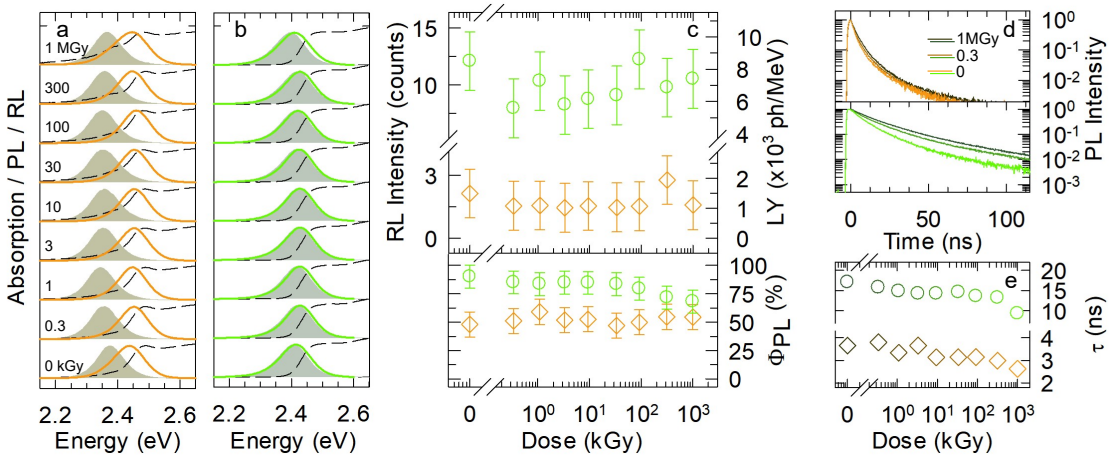

Figure 3.19: *Optical absorption (dashed lines), PL (solid lines) and RL (shaded areas) spectra of* **a)** *standard $CsPbBr_3$ NCs and* **b)** *$CsPbBr_3$:F NCs at increasing cumulated γ-ray doses from 0Gy to 1MGy (bottom to top). The spectra have been normalized at emission maxima and respective absorption edge and shifted vertically for clarity.* **c)** *LY and respective relative RL intensity (top panel) and Φ_{PL} (bottom panel) of $CsPbBr_3$ NCs (orange diamonds) and $CsPbBr_3$:F NCs (green circles) as a function of the cumulated dose.* **d)** *Normalized PL decay curves at 0 Gy, 0.3 MGy and 1 MGy, for $CsPbBr_3$ NCs (top panel) and $CsPbBr_3$:F NCs (bottom panel).* **e)** *Effective PL lifetimes for $CsPbBr_3$ NCs (orange diamonds) and $CsPbBr_3$:F NCs (green circles) as a function of cumulated dose, extracted as the time after which the intensity drops by a factor of e. Error bars are within the size of the data points.*

is ascribed due to the agglomeration of the NCs into larger particles also leading to enhanced light scattering, as will be discussed in Figure 3.20.

Possibly more importantly, as displayed in Figure 3.19c, the scintillation efficiency of both types of NC is found to be constant up to irradiation doses as large as 1 MGy, thus demonstrating the suitability of LHP NCs as stable active materials for application in harsh environments involving extreme levels of γ-radiation [96, 182]. The evolution of Φ_{PL} of both standard and resurfaced $CsPbBr_3$:F NCs (bottom panel of Figure 3.19c) confirms the marginal impact of γ-ray exposure also on the optical properties of both systems, with standard $CsPbBr_3$ NCs retaining Φ_{PL} ~45% up to 1 MGy, and $CsPbBr_3$:F NCs showing Φ_{PL}>70% even at the highest dose (corresponding to over 75% of the initial PL efficiency). Complementary indications of the stability of the NCs come from time-resolved PL measurements with increasing dose (Figure 3.19d and 3.19e) showing nearly constant dynamics in $CsPbBr_3$ NCs and a slight acceleration in F-treated NCs for 1MGy dose, still remaining substantially slower and more efficient that the standard counterparts. The essential independence of the LY with dose of the standard NCs further suggests that the radiation-induced agglomeration has negligible

impact on the actual scintillation performance.

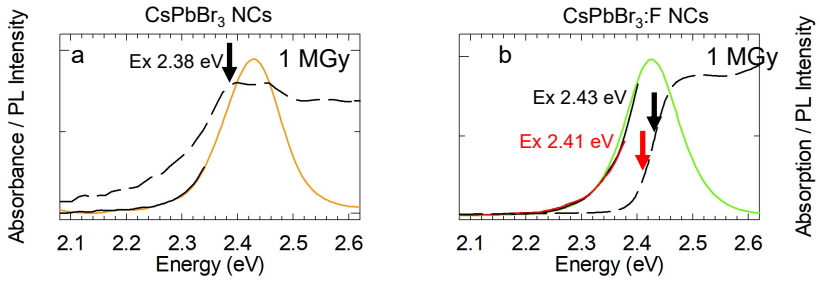

Figure 3.20: *Optical absorption (dashed lines) and photoluminescence (solid lines) spectra of the most γ-irradiated (1 MGy dose) $CsPbBr_3$ NCs (a) and fluorinated $CsPbBr_3$:F NCs (b) after being stored in air at 0°C for six-months. PL spectra are collected selectively exciting NC well above the band edge at 3.1 eV (solid orange 'a' and green lines 'b') and at sub-BE energies (as indicated in panels) to emphasise the presence of emitting sub-populations of NC clusters.*

As shown in Figure 3.20a after being stored in air at 0°C for six-months the untreated $CsPbBr_3$ NCs essentially retain their absorption edge at 2.46 eV followed by a low energy tail due to light scattering from large aggregates of both NCs and detached organic ligands. Notably, the absorption feature at 2.38 eV, attributed to bulk-like aggregates, intensified during storage indicating that the exposure to high γ-doses induced the formation of NC sub-populations with larger sizes to mitigate the radiation-induced destabilization of untreated NC surfaces over a long period of time. Selectively exciting NC aggregates at 2.38 eV, the collected PL spectrum perfectly matches the low energy shoulder of PL peak when exiting the whole system well above the BE at 3.06 eV. The same analysis for F-treated $CsPbBr_3$:F NCs in Figure 3.20b show the superior shelf stability of resurfaced NCs compared to standard counterparts, perfectly retaining their absorption profile and PL emission even when excited below the BE to disclose the presence of larger emissive NC sub-populations.

Temperature-Controlled RL and PL Measurements

To gather deeper insights into the scintillation and trapping mechanism and on the effect of surface fluorination, I performed RL and PL measurements as a function of temperature in the 10-290 K range. Here are presented the NCs at the edges of the irradiation range, namely 0 Gy and 1 MGy, representing the two extremes of this radiation hardness study. In Figure 3.21a and 3.21b is reported the evolution with temperature of the PL and RL of $CsPbBr_3$ NCs both non-irradiated and after 1 MGy γ-exposure. Consistently with the room temperature data shown in Figure 3.17, the PL is peaked

at 2.44 eV and is due to the recombination of BE excitons, whereas the RL originates from D_S. Upon cooling, the BE-PL red-shifts (∼50 meV between 290 K and 10 K) as a result of lattice expansion [127, 165, 166], and an intragap emission consistent with the D_S-RL spectrum emerges and gradually structures into a manifold of nearby peaks below $T = 150$ K. After γ-exposure it can be observed only a slight spectral broadening of both BE- and D_S- emissions, likely due to increased disorder following prolonged exposure to γ-ray. As highlighted by the vertical ticks in Figure 3.21a, the RL spectra of the standard NCs follow a nearly identical trend with temperature as the lowest energy contribution of the respective D_S-PL, further confirming that the same shallow defect states participate in both the PL and scintillation processes. Most importantly and in stark contrast to the standard $CsPbBr_3$ NCs, the fluorinated $CsPbBr_3$:F NCs show matching PL and RL spectra dominated by the recombination of BE excitons at any temperature for both the pristine and the irradiated sample and only a minor contribution by D_S emission emerging at cryogenic temperatures. To further clarify the role of D_S state in the excitonic recombination mechanism, in Figure 3.21e is quantified the relative weights of the BE and D_S contributions to the total PL intensity of $CsPbBr_3$ NCs as a function of temperature. The same analysis for the PL and RL trends of both samples is reported in Figure S8. In agreement with previous results (see 3.3), the BE- and D_S-PL intensities show clear anticorrelation, indicating that such states are in thermal equilibrium, with the D_S contribution being dominant at cryogenic temperatures (>75% of the total PL intensity) due to suppressed thermal detrapping to the BE (see scheme in Figure 3.21m). Time-resolved PL experiments (Figure 3f) corroborate this picture showing, at $T = 300$ K, a fast decay component (τ^{BE}_{Fast}= 1.9±0.4 ns, measured as the time after which the PL intensity has dropped by a factor e) due to the recombination of BE excitons, followed by a long-lived tail (τ^{BE}_{Slow} ∼100 ns) resulting from the delayed emission of thermally regenerated BE excitons by detrapping from D_S. Upon lowering T, τ^{BE}_{Fast} progressively accelerates, according to the bright nature of the triplet excitonic states in LHP NCs [167], and τ^{BE}_{Slow} remains essentially constant while its relative weight (I^{BE}_{Slow}) decreases. We estimate the detrapping energy (E_{DT}) by fitting the temperature dependence of I^{BE}_{Slow} with the expression $I^{BE}_{Slow} = I_0 e^{(-E_{DT})/(k_B T)}$ where I_0 is a scaling factor and k_B is the Boltzmann's constant (Figure 3g). Through this approach, I obtain $E_{DT} = 68\pm7$ meV, which matches well the energy difference between the BE and D_S emission peaks. The D_S-PL decays in Figure 3h return the complementary picture of the thermal interplay between D_S and BE states showing a non-exponential dynamics with a fast contribution at 150 K (τ^{Ds}_{Fast} = 50-150 ns) which matches τ^{BE}_{Slow} and is thus ascribed to D_S undergoing detrap-

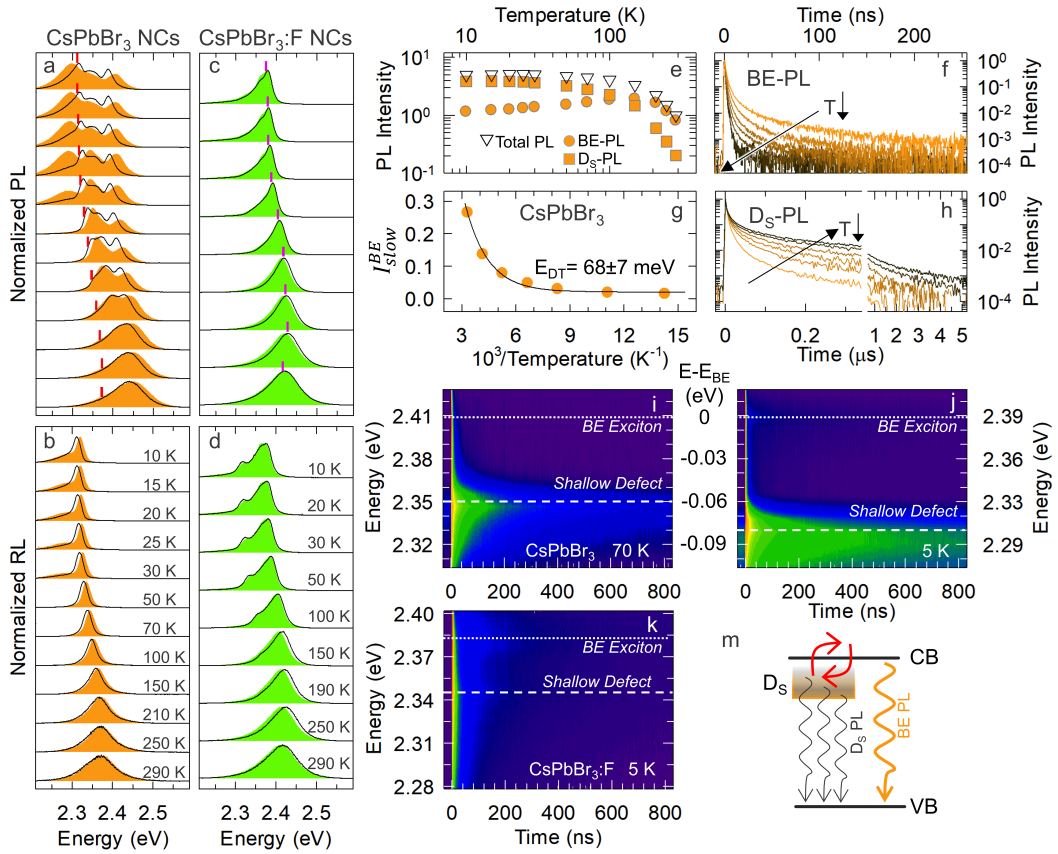

Figure 3.21: ***(a)*** *PL* ***(b)*** *and RL spectra of $CsPbBr_3$ NCs as a function of temperature (from 290 K to 10 K from bottom to top). In both panels, the solid lines correspond to pristine non-irradiated NCs whereas filled areas correspond to 1 MGy-irradiated NCs. The vertical red ticks in 'a' highlight the spectral position of the corresponding RL maximum from panel 'b'.* ***c,d)*** *Same as 'a' and 'b' for $CsPbBr_3$:F NCs.* ***e)*** *Normalized spectrally integrated total PL intensity as a function of temperature (triangles) and relative weights of the BE (circles) and D_S (squares) contributions for standard $CsPbBr_3$ NCs.* ***f)*** *Normalized BE-PL decay curves of $CsPbBr_3$ NCs as a function of decreasing temperature as indicated by the black arrow.* ***g)*** *Temperature dependence of the slow component of the BE-PL decay curves from panel 'f' expressed as its relative weight over the total decay. The fit to equation along with the text is shown as a black line.* ***h)*** *Normalized D_S-PL decay curves of $CsPbBr_3$ NCs as a function of decreasing temperature in the 8-150 K range as indicated by the black arrow. Contour plot of the spectrally resolved PL decay of $CsPbBr_3$ NCs at 70 K* ***(i)*** *and 5 K* ***(j)****; the energy axes are graphically aligned to the respective BE energy showing both the absolute energy and relative to the BE position (E-EBE). The spectral position of the BE and the D_S emission peak is displayed with dotted and dashed lines, respectively* ***k)*** *Contour plot of the spectrally resolved PL decay of F-treated $CsPbBr_3$:F NCs at 5 K.* ***m)*** *Schematic depiction of the T-dependent equilibrium between the BE and D_S emission in standard $CsPbBr_3$ NCs.*

ping to the BE, followed by a temperature-independent μs-lived tail consistent with the radiative emission from sub-populations within the D_S manifold not subjected to

thermal liberation. Upon cooling, the fast contribution becomes gradually weaker due to suppressed thermal detrapping and the slow decay tail concomitantly grows. We finally notice that, within the proposed scheme of thermally assisted detrapping of a manifold of D_S states, one would expect that the spectral difference between the BE and D_S contributions gradually increase with decreasing temperature, as the thermal budget for detrapping deeper D_S states is no longer available. The contour plot of the spectrally resolved PL decay of the $CsPbBr_3$ NCs at $T = 70$ K and $T = 5$ K (Figure 3.21i and 3.21j respectively) confirm this picture showing that the energy difference between the BE and the D_S emissions increases from 60 meV to nearly 80 meV upon cooling. On the other hand, the same analysis for the fluorinated $CsPbBr_3$:F NCs (Figures 3.21k) shows exclusively the fast recombination of the BE exciton with a negligible contribution from residual D_S states, thus further confirming that the fluorine treatment effectively suppresses surface defects responsible for delayed emission and efficiency losses under optical and X-ray excitation.

Thermally-Stimulated Luminescence and After-Glow Measurements

Finally, to assess the effects of exposure to very high levels of ionizing radiation and surface fluorination on the dynamics of trap-related phenomena and to investigate the possible involvement of long-lived nonradiative trap states not detected by RL and PL experiments, we performed thermally stimulated luminescence (TSL) and low-T afterglow (AG) measurements. Fundamentally, side-by-side experiments on pristine and 1 MGy-irradiated samples (Figure 3.22) of both standard and fluorinated NCs reveal no noticeable effect on neither systems upon prolonged exposure to γ-rays, further confirming the exceptional radiation hardness of LHP NCs.

Deeper comparison between the TSL data for the standard and the fluorine treated NCs further unveils substantial differences between their (de)trapping mechanisms. Specifically, the TSL contour plots and spectra of the standard $CsPbBr_3$ NCs evidence one emission band at 2.3 eV closely matching the respective RL emission ascribed to radiative defects (Figure 3.22a). The glow curve representing the evolution of the TSL intensity as a function of temperature and time (since in TSL experiments temperature and time are linearly correlated, see the Experimental Section 3.3.2) is reported in 3.23a for the pristine and irradiated samples, together with the respective AG decay curves (obtained by monitoring the emission over time at T=10 K after turning off X-ray excitation). The AG spectrum matches closely the corresponding TSL indicating that both emissions have the same defect origin as the RL. Most interestingly, the TSL

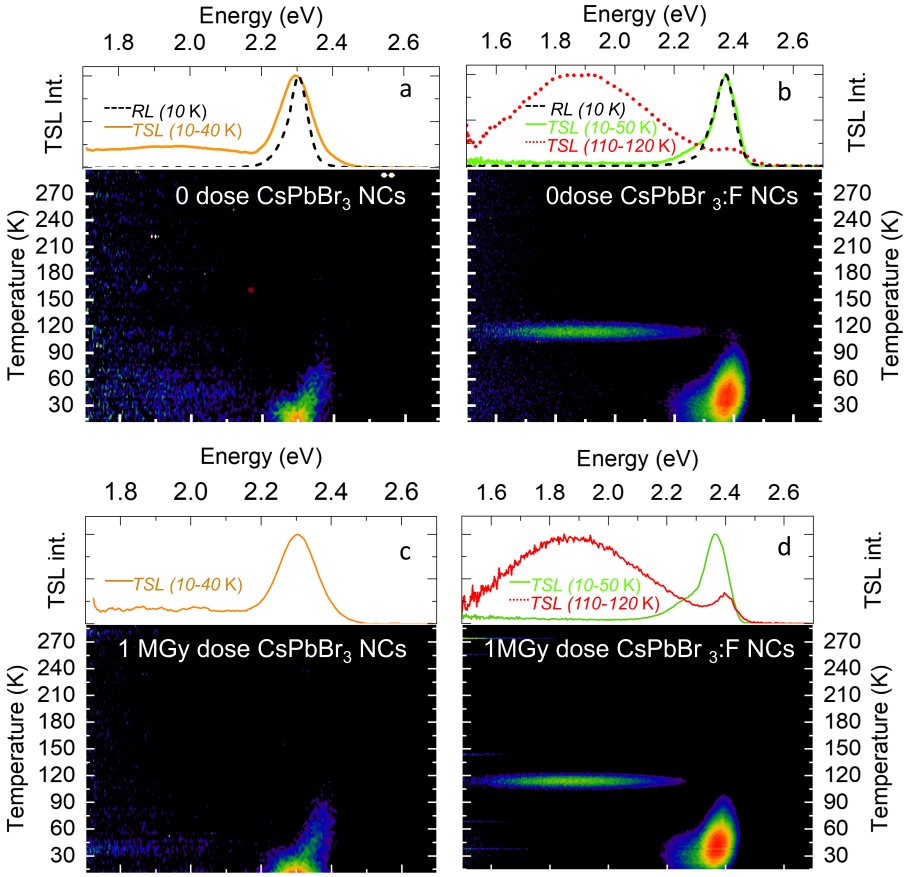

Figure 3.22: *Contour plot of the spectrally-resolved TSL intensity as a function of temperature in the 10 – 300 K range for non-irradiated $CsPbBr_3$ NCs* **(a)** *and for most γ-irradiated $CsPbBr_3$ NCs* **(c)**, *obtained after X-ray irradiation at 10 K. Top panel: Normalized TSL spectrum integrated between 10 K and 80 K (orange line) together with RL spectrum at T = 10 K (dashed black line).* **b,d)** *Same as 'a, c' for $CsPbBr_3$:F NCs. In top panel of 'b', the green and dark red curves represent the normalized TSL emissions related to BE and intragap deep defects respectively. The same color scheme applies to panel 'd'.*

and AG time traces are essentially identical to each other and well modelled with the power-law function $I(t) = A(t + t_0)^{-p}$ with $p \sim 1$. This, together with the absence of any TSL peak in Figure3.22a which excludes thermal contributions to the detrapping mechanism and consistent with the μs-long lifetime of the shallow defect-related PL, suggests that the slow AG emission originates from the release of carriers by a-thermal tunneling from a distribution of distances among isoenergetic non-radiative shallow trap states [169] (indicated as T_S in the scheme in Figure 3.23b) that mediate the gradual population of emissive shallow defects (D_S in the nomenclature used for Figure 3.21) clustered at the NC surfaces [170].

In stark contrast, the TSL contour plots of $CsPbBr_3$:F NCs and related spectral and

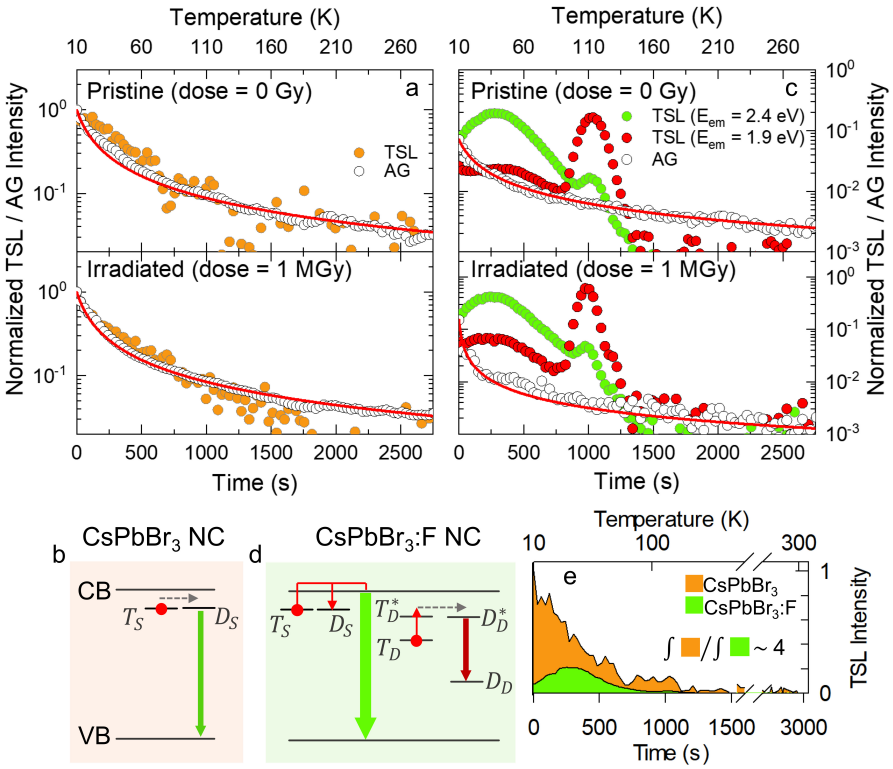

Figure 3.23: ***a)*** *Normalized glow curve (orange circles) extracted from Figure 3.22a (top panel) and 3.22c (bottom panel), and respective isothermal AG intensity at 10 K (white circles) for pristine non-irradiated (top panel) and 1 MGy γ-irradiated (bottom panel) $CsPbBr_3$ NCs as a function of temperature and delay-time after suppression of the irradiation. The fitting curve of the AG intensity to a power-law function is shown as red line.* ***b)*** *Schematic depiction of the liberation of electrons in shallow traps (T_S) towards isoenergetic emitting defects (D_S) via a-thermal tunnelling.* ***c)*** *Same as 'a' for $CsPbBr_3$:F NCs.* ***d)*** *Schematic depiction of the detrapping mechanisms in $CsPbBr_3$:F NCs showing thermal liberation of electrons from shallow traps (T_S) to the BE and from deep trap states (T_D) to deep intragap emitting centers (D_D).* ***e)*** *Comparison between the TSL intensity of standard and fluorinated $CsPbBr_3$ NCs corrected for the respective LY at different temperatures. The integral over temperature (time) of each curve is proportional to the respective trap concentration, which confirms the substantially lower trap density in $CsPbBr_3$:F NCs.*

thermal analysis (Figure 3.22b and 3.23c) show two distinct TSL features, a dominant band edge emission at 2.4 eV (with a minor shoulder at 2.3 eV at low temperatures due to residual surface defects) and a broad intragap emission at 1.9 eV emerging at $T = 112$ K and indicating the presence of deep defect states not observed in standard NCs.

Importantly, for the $CsPbBr_3$:F NCs the TSL glow curve and AG profile corresponding to the band edge emission are markedly different to each other: the AG decay follows a power-law function with p 1 similar to the standard NCs, whereas the

TSL features a broad low-temperature peak extending from $T = 20$ K to $T = 70$ K (Figure 3.23c) indicating thermal liberation of shallow traps to the band edge occurring even at low temperatures with a negligible contribution from detrapping by a-thermal tunnelling (see the scheme in Figure 3.23d). This corroborates the picture of effective suppression of surface defect states posited by fluorine resurfacing, leading to high PL quantum yield and light yield, as well as to substantially reduced spatial correlation between shallow traps and emissive centers. To further support this interpretation, we extracted the relative density of shallow traps in standard and $CsPbBr_3$:F NCs from the integrated intensity of the TSL profiles corrected for the respective temperature dependent light yield (see Methods). As shown in 3.23e, this semi-quantitative analysis highlights that the defect density is roughly four times lower in fluorinated NCs, in remarkably good agreement with the ca. 5-fold higher light yield of $CsPbBr_3$:F NCs with respect to the standard counterparts and consistent with the negligible effect of detrapping by a-thermal tunnelling. Finally, the sharp TSL peak at $T = 112$ K and its corresponding broad emission at 1.9 eV indicate complete depletion of a further deep trap state (indicated as TD in 3.23d) by thermally assisted tunneling, which is the dominant detrapping mechanisms observed in LHP bulk crystals with low intrinsic trap density [98, 130, 143], as discussed in Section 3.3. Therefore, the defectiveness of fluorinated $CsPbBr_3$:F NCs resembles that of LHP bulk crystals, and is characterized by isolated energetically deep defect states that trap carriers which, following heating, recombine with a specific intragap emission center. Consistently, the trap depth, Δ_{ET} = 260±40 meV (for the non-irradiated sample), extracted by the initial rise method matches closely the value recently obtained in $CsPbBr_3$ single crystals (Δ_{ET} = 260 meV) [143]. The same analysis on the 1 MGy-irradiated sample yields a comparable Δ_{ET} = 300±45 meV, further confirming the negligible effect of extreme irradiation also on deep trap states. In both cases, the trap lifetime at $T = 295$ K is found to be 1-3 μs, which is orders of magnitude longer than luminescence lifetime. The corresponding mechanistic scheme is depicted in Figure 3.23d, showing the initial thermal excitation of carriers trapped in deep traps ($T_D \rightarrow T_D^*$) followed by tunneling to the excited state of a deep emissive center (D_D^*) from where emission occurs, leading to the one-to-one correlation of the TSL dynamics. Therefore, the whole body of spectroscopic and scintillation data suggest that in standard $CsPbBr_3$ NCs shallow trap states likely related to bromine vacancies capture and slowly release electrons via a-thermal tunneling to spatially connected emissive centers responsible for delayed emission. Because of the relatively large concentration of such defects, electron trapping in shallow defects is the main competitive channel to radiative exciton decay in $CsPbBr_3$ NCs and deep traps

typically found in bulk crystals play a minor role. Fluorine treatment removes such shallow defects, boosts the scintillation efficiency, and makes it possible to detect the spectroscopic signature of deeper defects common to bulk crystals, which cannot be emptied except by providing the necessary thermal budget and have negligible effect on the emission efficiency of F-treated NCs that approaches unity.

3.4.4 Conclusions

In summary, we performed an in-depth spectroscopic investigation on the effect of extreme levels of γ-ray doses – across six orders of magnitude, up to 1 MGy – on $CsPbBr_3$ perovskites NCs both standard and resurfaced with F^- ions. Our results reveal that both systems retain their whole initial scintillation efficiency even after 1 MGy of γ-dose demonstrating, for the first time, the suitability of this class of materials as high-Z functional materials for application in harsh environments with severe levels of γ-radiations. Side-by-side optical and scintillation spectroscopies show the presence of shallow surface defects that are nearly completely suppressed by post synthetic fluoride treatment. This results in efficient scintillation dominated by the radiative recombination of band edge excitons, ultimately demonstrating that the low trapping losses characteristic of massive LHP solid can be realized in nanoscale particles with scintillation performance matching that of commercial inorganic scintillators.

3.4.5 Appendix

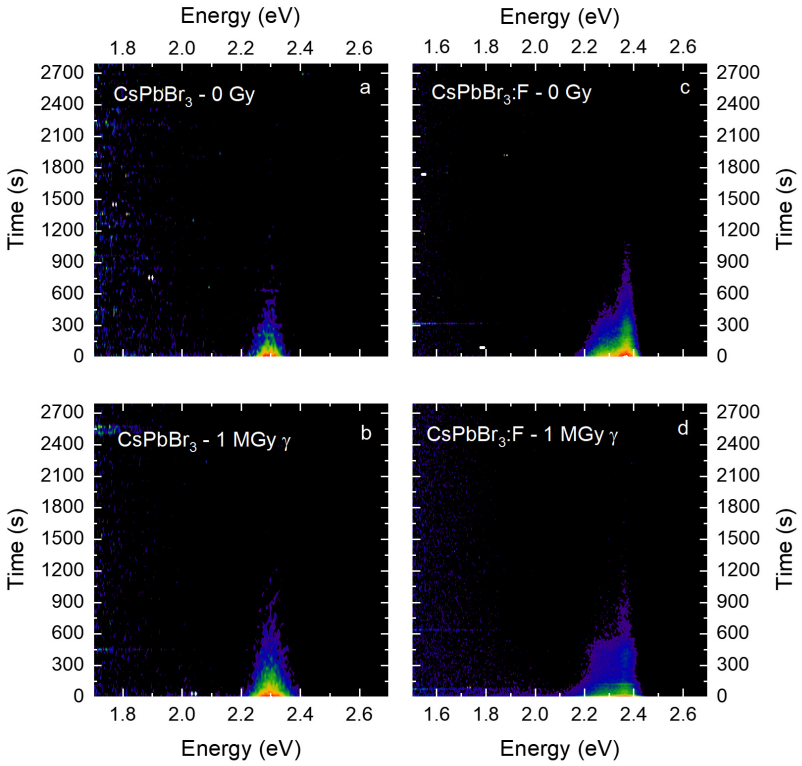

Figure 3.24: ***a)*** *Contour plot of the spectrally-resolved isothermal decay of AG intensity at 10 K as a function of time for non-irradiated $CsPbBr_3$ NCs, obtained after X-ray irradiation.* ***b)*** *Same as 'a' for 1 MGy-irradiated $CsPbBr_3$ NCs.* ***c)*** *Same as 'a' for non-irradiated fluorinated $CsPbBr_3$:F NCs.* ***d)*** *Same as 'b' for 1 MGy-irradiated fluorinated $CsPbBr_3$:F NCs.*

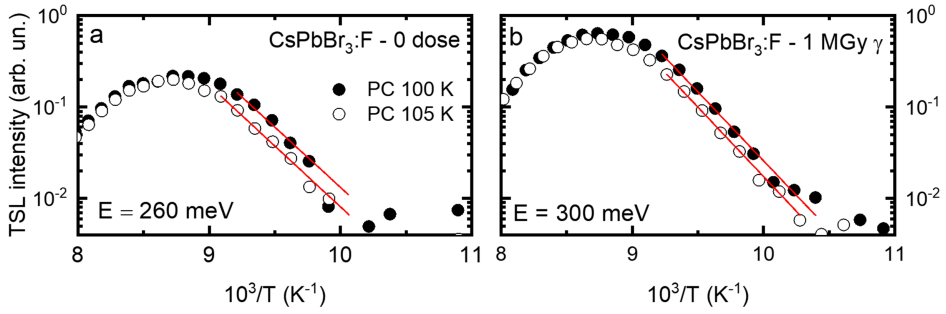

Figure 3.25: ***a)*** *Arrhenius plot and fit (red solid lines) of the 112 K TSL peak of non-irradiated $CsPbBr_3$:F NCs after X-ray irradiation at 10 K and partial cleaning at 100 K (full symbols) and 105 K (open symbols).* ***b)*** *Same as 'a' for 1 MGy-irradiated $CsPbBr_3$:F NCs*

Chapter 4

Beyond Lead Halide Perovskites: Sb-doping Activates Efficient Stokes-Shifted Emission in Double Perovskites Nanocrystals

Nanocrystals (NCs) of lead halide perovskites have attracted a significant interest in recent years and are promising candidate materials for various optoelectronic applications. [132, 183–188] However, given the intrinsic toxicity of lead, which constrains the use of such materials in commercial devices, the scientific community is now seeking for alternative stable lead-free metal halide perovskite compounds with comparable optical properties. [189, 190] The most promising candidates in this context are the so-called double perovskites (DPs), also termed elpasolites, having general formula $A_2B^+B^{3+}X_6$*, characterized by a 3D perovskite structure made of alternating* $[B^+X_6]$ *and* $[B^{3+}X_6]$ *corner-sharing octahedra with* A^+ *ions occupying the voids in between. [189–192] The different combinations of possible* A^+*,* B^+ *and* B^{3+} *ions create a richness of structures, making the elpasolites family particularly interesting from a chemistry and a materials science point of view, [191] as well as for technological applications in photovoltaics, [193–195] artificial lighting and photon management. [196]*

4.1 State of the Art

In the last couple of years, various DP materials featuring interesting optical properties have been synthesized at the nanoscale, comprising Cs_2AgBiX_6 (X=Cl, Br, I),

$Cs_2AgInCl_6$, $Cs_2NaInCl_6$, $Cs_2NaBiCl_6$ and Cs_2AgSbX_6 NCs (X=Cl, Br). [197–210] Unluckily, all these systems feature a weak PL emission due to the fact that they have either an indirect bandgap (Cs_2AgBiX_6, Cs_2AgSbX_6) or a direct bandgap characterized by a parity forbidden transition ($Cs_2AgInCl_6$) or by a parity allowed transition albeit with a weak oscillator strength (Cs_2NaInX_6, Cs_2NaBiX_6). [190–192, 205, 211–213] As a result, the interplay between radiative and non-radiative processes make the excitonic photophysics of these materials significantly more complex than for the case of lead halide perovskites. This calls for specific multidisciplinary investigations to trace rational guidelines for their optimization. In turn, the control and the design of highly performing DP materials has great technological implications, as it will enable us to ripe the benefits of their intrinsically broad and largely Stokes shifted luminescence that makes them particularly appealing for heavy-metal free single-component white light emitting diodes [196] and for transparent luminescent solar concentrators for building integrated PV applications [214].

In order to enhance the PL emission of double perovskites, different strategies have been already pursued which involved doping, alloying, or both [190, 195, 196, 199, 203, 205, 206, 208, 215–224]. Among the different dopants, Sb^{3+} cations are particularly interesting, as they confer highly efficient optical emission properties to bulk DPs. [225–231] For example, several works have demonstrated that Sb-doping of $Cs_2NaInCl_6$ DP bulk crystals yields a bright, broad (full width at half-maximum of 80 nm) emission centered at ∼450 nm with a PL quantum yield (Φ_{PL}) of ∼80%. [225,227,230] Similarly, Noculak et al. synthesized both $Cs_2NaIn_{1-x}SbxCl_6$ and $Cs_2KIn_{1-x}SbxCl_6$ powders, exhibiting blue and green emission, respectively, with Φ_{PL} as high as ∼90%. [228] Sb^{3+} cations were found to be efficient dopants also for other metal halides, such as the so-called "0D" structures: here the metal halide octahedra are isolated from each other (Figure 4.1). [232–237] In this regard, various non-luminescent or weakly luminescent 0D host bulk materials (Cs_2SnCl_6, Rb_3InCl_6, Cs3InCl$_6$, and their hydrated counterparts) were reported to show bright PL emission, with Φ_{PL} values typically reaching ∼90% when doped with Sb^{3+} cations. [233–236, 238]

As a general trend, Sb-doped DPs and 0D materials are all characterized by identical near-UV absorption features that have been attributed to electronic transitions within the [$SbCl_6$] octahedra, which are considered to act as sensitizers in a host matrix that is transparent to light at the band edges (due to parity-forbidden transitions). [225–229, 233–236, 238] The absorption from [$SbCl_6$] octahedra resembles an atomic-like excitation influenced by spin–orbit coupling, featuring a peak at high energies (∼280 nm, ascribed to the $^1S_0 \rightarrow {}^3P_2$ transition) and a doublet at lower energies (in the

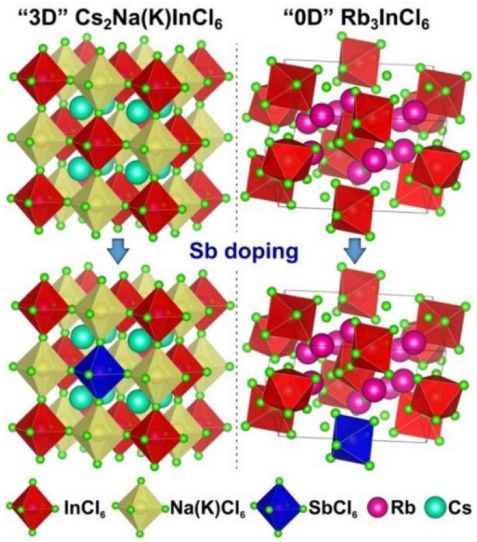

Figure 4.1: *Sketch of the crystal lattices of undoped and Sb-Doped "3D" double perovskites and "0D" NCs presented in this section*

300–400 nm range, corresponding to the parity-allowed, spin-forbidden $^1S_0 \rightarrow {}^3P_1$ and $^1S_0 \rightarrow {}^3P_0$ transitions). [225–229, 233–237] In emission, the $[SbCl_6]$ octahedra act also as recombination centers by undergoing a large structural reorganization, as evidenced by the substantial Stokes shift. Recently, Zhang et.al [239] demonstrated that the isolated $[SbCl_6]^{3-}$ octahedra are the only optically active centers in emission because the local arrangement of the Rb^+ ions around the octahedra limits the elongation of the Sb–Cl bonds upon excitation, helping to confine the self-trapped exciton in them. Accordingly, the different coordination environments probed by the Sb^{3+} cations determines the Stokes-shift of each system; so far have been reported Stokes-shift of ∼0.91 eV in Sb-doped $Cs_2NaInCl_6$, 2.1 eV in Sb-doped $Rb_2InCl_5{\cdot}H_2O$, 1.29 eV in Sb-doped Rb_3InCl_6, and 1.19 eV in Sb-doped Cs_2KInCl_6. [228]

4.2 Sb-Doped Metal Halide Nanocrystals: A 0D versus 3D Comparison

In this section I will introduce the spectroscopic investigation of new Sb doped metal halide systems in NC form aimed at understanding their emission characteristics. In particular, I want to elucidate the role of the connectivity of metal halide octahedra and its influence on the optical properties of Sb-doped materials at the nanoscale. We synthesized both undoped and Sb-doped NCs of $Cs_2NaInCl_6$, Cs_2KInCl_6 (two different

DP materials) and Rb_3InCl_6 (a 0D system) and carried out optical and computational analyses on them. In absorption, both 3D and 0D systems behave very similarly, while most differences lie in their emission features. The Sb-doped "0D" Rb_3InCl_6 NCs tend to have a markedly higher Φ_{PL} (∼40%) than the corresponding Sb-doped "3D" DP ($Cs_2NaInCl_6$ and Cs_2KInCl_6) NCs (∼15–18%), although both present values are well below those of the bulk crystal counterparts. Also corroborated by computational analysis here will be suggested that, in the 0D case, the isolated [$SbCl_6$] octahedra form self-trapped excitons (STEs) that are less likely to migrate to a defect-rich surface of the NCs, dominated by under-coordinated halide ions (which will be proved to be the main source of traps). This behavior contrasts with the DP case, where [$SbCl_6$] octahedra are interconnected with [Na(K)Cl_6] and [$InCl_6$] octahedra (hence STEs are more likely to migrate to the surface), rendering them more prone to non-radiative losses. In all these materials, the (large) Stokes shift was found to depend strongly on the lattice cage that surrounds the [$SbCl_6$] octahedron. Our computational analysis on the origin of such shift found that in the DPs the large size of the K^+ ion causes a more marked structural rearrangement in the excited state than the corresponding smaller Na^+ ion, indicating that, by changing the type of B^+ ions, the emission wavelength can be, in principle, tuned on-demand.

Motivated by their intense PL and large Stokes shifts, I tested our NCs as re-absorption-free scintillators for high-energy radiation detection. Both DP systems feature intense X-ray radioluminescence (RL), closely matching their respective PL, with negligible overlap with the corresponding absorption profile and nearly perfect radiation hardness for almost 500 Gy of cumulative delivered dose. The 0D NCs had instead a main RL at ∼4 eV (originating from the host lattice) overlapping with their absorption and were not studied further. The applicability of these DP systems in real re-absorption-free plastic scintillator detectors was finally simulated via Monte Carlo ray-tracing calculations, revealing essentially perfect waveguiding performance in large-area devices compatible with real-world applications. This result suggests a new, still unexplored materials design concept for Stokes shift engineering that exploits Jahn–Teller distortions upon photo-excitation of dopant-related emissive centers, with great potential for light management technologies based on wavelength-shifting waveguides.

4.2.1 Samples Description

Synthesis of Sb-Doped DP NCs

The synthesis of material has been carried out by the team of Dr. Liberato Manna from the *Italian Institute of Technology* (Genoa, IT). In a typical synthesis, Cs_2CO_3(0.25 mmol), Na(Ac)(0.25 mmol), $In(Ac)_3$(0.25 mmol), 4 ml dioctyl ether (DOE), 1.2 ml oleic acid (OA) and 0.6 ml oleylamine (OLAM) were mixed in a 20 ml vial under N_2. Then, the system was heated on a hotplate up to 140 °C and at that temperature a solution of 220 μL benzoyl chloride (Bz-Cl) in 0.5 ml of degassed DOE was swiftly injected into the vial. Immediately after the injection, the reaction was cooled down by an ice-water bath. Then, 3 ml of hexane was added to the solution, which was then centrifuged at 4000 rpm for 5 min, and the supernatant was discarded. The precipitated NCs were redispersed in 3 mL of hexane, and centrifuged at 5500 rpm for 5 min. The precipitated NCs were discarded and the supernatant was precipitated by adding 3 ml ethyl acetate and centrifuged at 4000 rpm for 5 min. The precipitated NCs were dispersed in 1.5 ml of hexane and centrifuged at 5500 rpm for 5 min. The supernatant was stored in a vial for further characterizations. All the washing procedures were carried out under inert atmosphere. Sb-doped $Cs_2NaInCl_6$ NCs were obtained by the same protocol, but adding different amounts of antimony(III) acetate - $Sb(Ac)_3$ - while keeping all the reaction parameters fixed. The Sb/In feed ratio was varied from 0.5% to 1%, 5%, 10%, 20% obtaining Sb content varying from 0 to 8.0% (atomic% with respect to In) as emerged from elemental analyses based on energy-dispersive spectroscopy in the scanning electron microscope (SEM-EDS) and on inductively coupled plasma optical emission spectroscopy (ICP-OES) (Tables 4.1). The undoped and Sb-doped Cs_2KInCl_6 NCs were synthesized using the same method employed for the undoped and Sb-doped $Cs_2NaInCl_6$ NCs with minor modifications: Na(Ac) was replaced by K(Ac), 0.175 mmol of $In(Ac)_3$ were used, and all the other reaction parameters were kept constant. The Sb/In feeding amount was varied from 0.25% to 1%, 5%, 10%, 20%. SEM-EDS and ICP-OES results are reported in Table 4.2.

Transmission electron microscopy analysis indicates that the Sb-doped $Cs_2NaInCl_6$ NCs have a mean size around 20 nm, while the Sb-doped Cs_2KInCl_6 NCs are smaller, with a mean diameter around 13 nm. X-ray powder diffraction (XRD) characterization of the NC samples indicated that they all exhibit a DP cubic structure. Specifically, the XRD patterns of $Cs_2NaInCl_6$ NCs well match with the bulk DP $Cs_2NaInCl_6$ structure reported by Noculak et al. [228] (Figure 4.2g), albeit with slightly larger lattice parameters (a = 10.533 Å in this work and a = 10.514 Å in the work of Noculak et al.).

Sb/In precursors ratio (%)	SEM-EDS composition	Sb/In (%)
0	$Cs_{2.09}Na_{0.94}InCl_{6.07}$	0
0.5	$Cs_{2.14}Na_{0.96}InSb_{0.01}Cl_{6.18}$	0.3
1	$Cs_{2.24}Na_{0.95}InSb_{0.01}Cl_{6.17}$	0.7
5	$Cs_{2.17}Na_{1.05}InSb_{0.04}Cl_{6.30}$	3.2
10	$Cs_{2.20}Na_{1.04}InSb_{0.05}Cl_{6.30}$	4.9
20	$Cs_{2.15}Na_{0.94}InSb_{0.08}Cl_{6.17}$	8.0

Table 4.1: *Composition of Sb-doped $Cs_2NaInCl_6$ NCs measured by SEM-EDS and ICP-OES analyses. The stoichiometry of the samples was expressed in relation to the quantity of In, which was assumed to be 1.*

Sb/In precursors ratio (%)	SEM-EDS composition	Sb/In (%)
0	$Cs_{2.39}K_{0.92}InCl_{6.73}$	0
0.25	$Cs_{2.33}K_{0.84}InCl_{6.49}$	0.1
1	$Cs_{2.40}K_{0.92}InCl_{6.71}$	0.9
5	$Cs_{2.20}K_{0.99}InCl_{6.63}$	1.6
10	$Cs_{2.31}K_{0.95}InSb_{0.01}Cl_{6.73}$	3.3
20	$Cs_{2.34}K_{0.99}InSb_{0.05}Cl_{6.74}$	6.3

Table 4.2: *Composition of Sb-doped Cs_2KInCl_6 NCs measured by SEM-EDS and ICP-OES analyses. The stoichiometry of the samples was expressed in relation to the quantity of In, which was assumed to be 1.*

Given the absence of known DP Cs_2KInCl_6 crystal structures, in the case of Cs_2KInCl_6 NCs the whole-powder-pattern decomposition technique was employed, based on the Pawley algorithm, [240] which indicated that these samples possess a cubic crystal structure (space group $Fm\bar{3}m$) with the cell parameter $a = 10.871$ Å (Figure 4.2h). Compared to the bulk reflections of the DP $Cs_2NaInCl_6$ material, the diffraction peaks of Cs_2KInCl_6 NCs are slightly shifted to lower 2θ angles owing to the difference between the ionic radii of Na^+ and K^+ (102 pm for Na^+ and 138 for K^+). It is interesting to note here that bulk Cs_2KInCl_6 crystals tend to crystallize in a tetragonal structure, [228] thus adopting a lower symmetry with respect to our cubic NCs. In both DP systems ($Cs_2NaInCl_6$ and Cs_2KInCl_6), the introduction of Sb did not result in a shift of the XRD peaks, most likely due to the fact that Sb^{3+} and In^{3+} cations have similar ionic radii (80 pm for In^{3+} and 76 pm for Sb^{3+}). [241]

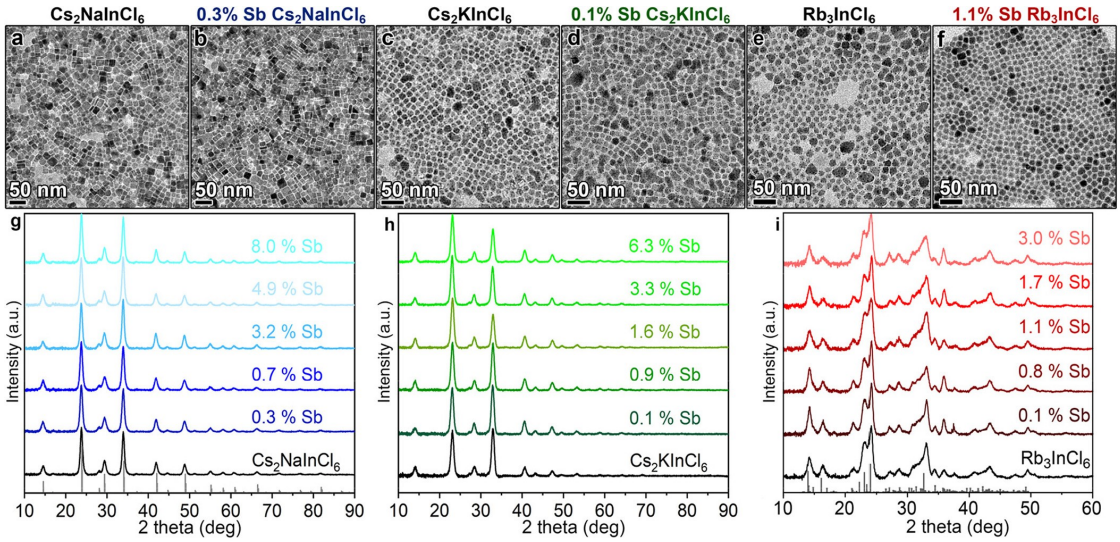

Figure 4.2: *Bright-field TEM images of* ***(a)*** *undoped and* ***(b)*** *0.3% Sb-doped $Cs_2NaInCl_6$ NCs;* ***(c)*** *undoped and* ***(d)*** *0.1% Sb-doped Cs_2KInCl_6 NCs; and* ***(e)*** *undoped and* ***(f)*** *1.1% Sb-doped Rb_3InCl_6 NCs. XRD patterns of* ***(g)*** *$Cs_2NaInCl_6$,* ***(h)*** *Cs_2KInCl_6, and* ***(i)*** *Rb_3InCl_6 NC samples containing different Sb doping amounts. The gray bars in 'g' and 'i' are the bulk reflections of the cubic DP $Cs_2NaInCl_6$ and Rb_3TlCl_6 (ICSD number 300228) crystal structures, respectively.*

Synthesis of '0D' Sb-Doped Rb_3InCl_6 NCs

The synthesis of Sb-doped "0D" Rb_3InCl_6 NCs has been adapted from the 3D DPs above with slight modifications. In a typical synthesis, Rb_2CO_3 (0.375 mmol), $In(Ac)_3$((1-x)*0.25 mmol), $Sb(Ac)_3$(x*0.25 mmol), 4 ml DOE, 1.2 ml OA, 0.6 ml OLAM were mixed in a in a 20 ml vial under N2. Then, the system was heated on a hotplate up to 140 °C and at that temperature a solution of 220 µl Bz-Cl in 0.5 ml of degassed DOE was swiftly injected into the vial. Immediately after the injection, the reaction was cooled down by an ice-water bath. The washing and precipitation steps were similar to those employed for Sb doped $Cs_2Na(K)InCl_6$ NCs except for the use of 6 ml (rather than 3 ml) of ethyl acetate. Here, the x values were selected as 0.1%, 5%, 10%, 10% and 20%, respectively. The Sb content varies from 0 to 3.0% (atomic% with respect to In), as emerged from SEM-EDS and ICP-OES elemental analyses (Table 4.3). The size of these NCs was around 14 nm, as indicated by TEM (Figure 4.2e and 4.2f). The XRD pattern of such NCs could not be indexed with the monoclinic (space group C_2/c) Rb_3InCl_6 structure recently reported by Majher et al. [234] On the other hand, was found a good match with the monoclinic Rb_3TlCl_6 structure (ICSD no. 300228) belonging to the P121/c1 space group (Figure 4.2i). The XRD pattern of our NC samples was characterized by peaks that are slightly shifted toward higher 2θ angles

with respect to those of Rb_3TlCl_6, consistent with the smaller ionic radius of In^{3+} compared with Tl^{3+} ions (88 pm for Tl^{3+} and 80 pm for In^{3+}). [241]

Sb/In precursor ratio (%)	SEM-EDS composition	Sb/In (%)
0	$Rb_{2.49}InCl_{5.92}$	0
1	$Rb_{2.37}InCl_{5.96}$	0.1
5	$Rb_{2.47}InCl_{6.16}$	0.8
10	$Rb_{2.31}InCl_{6.16}$	1.1
15	$Rb_{2.44}InCl_{6.05}$	1.7
20	$Rb_{2.41}InCl_{6.12}$	3.0

Table 4.3: *Composition of Sb-doped Rb3InCl$_6$ NCs measured by SEM-EDS and ICP-OES analyses. The stoichiometry of the samples was expressed in relation to the quantity of In, which was assumed to be 1.*

4.2.2 Experimental Details

Optical Measurements

The absorption spectra were recorded using a Varian Cary 50 ultra violet-visible absorption spectrophotometer. The steady-state PL and PL excitation (PLE) spectra were measured on a Varian Cary Eclipse spectrophotometer. Time-resolved PL experiments were conducted exciting the samples with a frequency tripled pulsed Nd:YAG laser at 3.49 eV collecting with the setup described in detail in Section 2.2.2. The PL efficiencies were measured at room temperature comparing the PL intensity, under steady-state excitation at 3.87 eV, of an hexane dispersion of NCs, and the emission from Quinine Sulfate dissolved in 0.5 M H_2SO_4 used as standard reference material. [242]

Radioluminescence Measurements

The radioluminescence studies are conducted on 0.7% Sb-doped $Cs_2NaInCl_6$ NC, 0.9% Sb-doped Cs_2KInCl_6 NC and 0.8% Sb-doped Rb3InCl$_6$ NC samples using the experimental setup described in Section 3.2.2.

Monte Carlo Ray-Tracing Simulations

Simulations have been run in collaboration with Glass To Power Spa similarly to the methods described in section 2.2.2. For this specific study adjustments were made as follows. Inside the scintillator material, for each ray, the inverse transform sampling

method is applied to randomly generate the length of the optical path before absorption by the NCs. Path lengths follow the exponential attenuation law determined by the wavelength-dependent absorption cross section, $\sigma(\lambda)$, and the NC concentration (N(λ),), via an attenuation coefficient, k(λ)= k(λ)N(λ). Since the mean path length, given by the inverse attenuation coefficient, is always much greater than the average distance between NCs, there is no need to keep track of an explicit position of each NC, so the nanocomposite material (PMMA + NCs) can be considered within the effective medium approach, i.e., as a uniform material with the attenuation coefficient defined above. Once a photon is absorbed by a NC, the subsequent fate of the excitation (i.e., reemission or nonradiative relaxation) is again determined by the Monte Carlo sampling according to the emission quantum yield. The direction of reemission is distributed uniformly and the reemission wavelength is determined using the rejection sampling applied to the accurate NC luminescence spectrum obtained from experiment. The ultimate fate of each photon is either loss due to nonradiative recombination or escape from the scintillator via one of the interfaces.

4.2.3 Results

Density Functional Theory

First, to provide insights into the electronic structure of Sb-doped 3D and 0D systems, the NanoChemistry group from the *Istituto Italiano di Tecnologia* in Genoa (IT), performed density functional theory (DFT) calculations. The model starts from the assumption that the [$SbCl_6$] octahedron is electronically isolated in both materials: in the 0D by virtue of the crystal structure, and in the 3D because it is surrounded by six wide bandgap [B^+Cl_6] octahedra [$B^+ = Na^+, K^+$]. Calculations return the electronic structure of the $[SbCl_6]^{3-}$ system with a local O_h symmetry which is found in both the DP and 0D lattices, with the Cs or Rb ions not participating to the band edges. With this small model system, we were able to include, in a simple way, also the spin–orbit coupling contribution, thus providing a clear understanding of the absorption features of the sensitizing centers, namely the [$SbCl_6$] octahedra.

In Figure 4.3, we show that the spin-free relativistic calculations at the DFT/PBE level of theory give a HOMO–LUMO gap of 3.76 eV, whereas the inclusion of spin–orbit coupling splits the t_{1u} triply degenerate LUMOs into doubly degenerate e1/2u (3.46 eV) and quadruply degenerate $u_{3/2u}$ (3.91 eV) molecular orbitals (MOs). Upon excitation from the $e_{1/2g}$ doubly degenerate HOMO, 12 possible excitations are possible, as depicted on the right side of Figure 4.3. Here we labeled the transitions also according

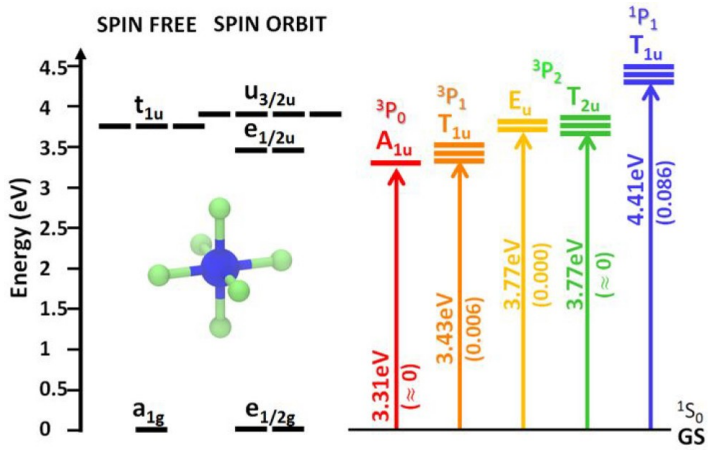

Figure 4.3: *HOMO and LUMO levels of an ideal $[SbCl_6]^{3-}$ complex featuring an O_h symmetry and calculated at the DFT/PBE level of theory (left) using a spin-free relativistic approximation and (center) including the spin–orbit coupling effects. (right) Lowest spin–orbit coupled electronic transitions with the associated energies and oscillator strengths named according to the free ion (top) and the O_h symmetry (bottom).*

to the atomic symmetry, which helps to draw a comparison with an atomic-like description. The order of the transitions is the same as in the atomic case for Sb^{3+}, although the presence of σ-antibonding interactions between the 5s of Sb and the 3p of Cl ions decreases dramatically the HOMO–LUMO gap by 5 eV and also reduces the differences among the states. Then, the transitions from the ground state to A_{1u} ($^3P_0$) and T_{1u} ($^3P_1$) have very low oscillator strengths because are mostly spin-forbidden (singlet to triplet), with selection rules that are only a little relaxed in the presence of spin–orbit coupling, suggesting that these systems will still retain long emission lifetimes.

Optical Measurements

On these grounds, I investigated the photophysics of the synthesized NCs via side-by-side optical spectroscopy experiments. In Figure 4.4a, is reported the Tauc plot of the optical absorption spectrum of undoped $Cs_2NaInCl_6$ NCs, showing the clear signature of a direct forbidden band gap at 2.9 eV, in agreement with previous reports on bulk analogues. [197, 225] These NCs exhibit no appreciable PL, consistent with the very low oscillator strength of the intrinsic edge-to-edge transition. [243] A similar optical behavior was seen in Cs_2KInCl_6 NCs, which had a slightly larger energy gap (3.0 eV, Figure 4.4b). The presence of Sb dopants in either DP host introduces two sharp features in the absorption profile at 3.90 and 3.72 eV (Figure 4.4c and 4.4d) and activates a broad, largely Stokes-shifted PL at 2.73 and 2.44 eV for the Sb-doped $Cs_2NaInCl_6$

and Cs_2KInCl_6 NCs, respectively. Notably, both the optical absorption profiles and the PL energies are essentially independent from the Sb content. This supports the hypothesis that the NCs' photoexcitation and radiative relaxation processes are caused by transitions of individual [$SbCl_6$] octahedra, in agreement with the STEs commonly invoked to explain the optical behavior of Sb-doped DPs bulk crystals. In emission, this effect would also account for the large Stokes shift connected with a Jahn–Teller lattice rearrangement (more details along with the text). [225]

The PL excitation (PLE) spectra collected at the PL maxima (dashed lines in Figure 4.4c and 4.4d) support this scenario by demonstrating that the PL originates from the radiative relaxation of $SbCl_6$ excited states. The Φ_{PL} at different Sb contents is almost constant for both sets of DP NCs (Figure 4.4e and 4.4f), slightly decreasing from ∼15–18% for the lowest Sb doped sets of NCs to ∼11% for the highest doped set of NCs. This is consistent with the very weak dependence of the PL decay dynamics of either systems on the Sb content, as reported in Figure 4.4g and 4.4h. The PL decay dynamics evidence a long-lived single exponential luminescence decay with lifetimes of ∼1.6 μs for Sb-doped $Cs_2NaInCl_6$ and ∼2.7 μs for Sb-doped Cs_2KInCl_6 NCs. The initial very fast component (∼8 ns), common to the whole sets of NCs, is due to the PL from the surfactants under UV excitation. In both cases, the PL lifetime is compatible with a partially spin-forbidden transition undergoing a slight acceleration with increasing Sb content, in accordance with the respective Φ_{PL} trend (Figure 4.4e and 4.4f).

Notably, by comparing Sb-doped $Cs_2NaInCl_6$ and Cs_2KInCl_6 NCs, it appears that the latter exhibit slower recombination rates and are also characterized by an initial multi-exponential decay component which is consistent with a higher lattice disorder, induced, most likely, by a more pronounced structural distortion in the excited state. This, in turn, accounts for the larger Stokes shift between the absorption and PL spectra. A similar behavior has been reported by Nokulak et al. for bulk crystals of the same compositions. [228]

Having assessed the optical properties of the DPs NCs, I then studied the photophysics of undoped and Sb-doped "0D" Rb_3InCl_6 NCs. The undoped system shows an optical behavior similar to that of the DP NCs just discussed, with a direct forbidden band gap at 3.6 eV (Figure 4.5a) and no appreciable PL. The incorporation of Sb dopants introduces the characteristic double-absorption feature at 3.9 and 3.7 eV, whose optical excitation turns on the PL at 2.45 eV (Figure 4.5b). The PLE spectra confirm this picture, indicating that also in Sb-doped Rb_3InCl_6 NCs the transient distortion of the [$SbCl_6$] octahedra is responsible for the large Stokes shift between the

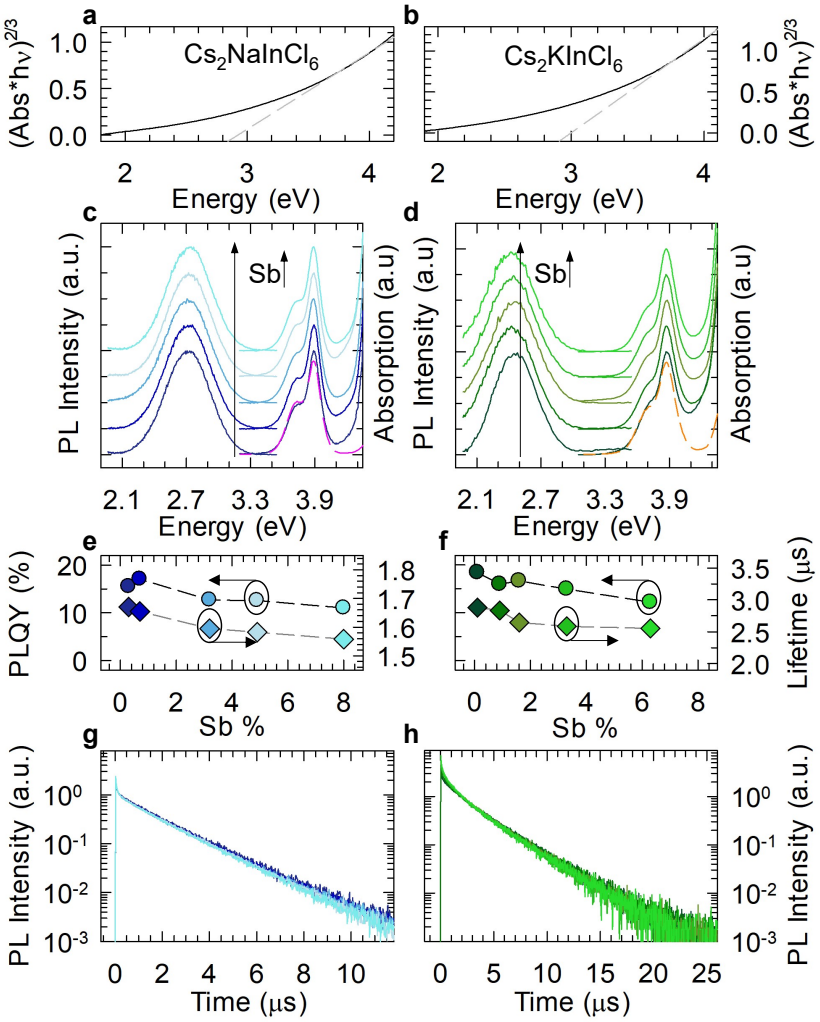

Figure 4.4: *Tauc plot for undoped $Cs_2NaInCl_6$* ***(a)*** *and Cs_2KInCl_6* ***(b)*** *NCs. Gray dashed lines represent the fit with the theoretical absorption profile of a semiconductor with a direct forbidden energy gap; the intercept with the abscissa axis corresponds to the semiconductor's forbidden gap energy.* ***c, d)*** *Absorption and PL spectra for Sb-doped $Cs_2NaInCl_6$ 'c' and Sb-doped Cs_2KInCl_6 'd' NCs with increasing Sb content, from bottom to top. PL excited with 3.87 eV (320 nm). Representative normalized PLEs obtained for PL maxima are reported as dashed lines.* ***e)*** *Absolute Φ_{PL} (circles) and PL lifetimes (diamonds) extracted from 'g' as a function of the incorporated Sb amount for Sb-doped $Cs_2NaInCl_6$ NCs.* ***f)*** *Same as 'e' for Sb-doped Cs_2KInCl_6 NCs. Lifetimes are extracted from 'h'.* ***g, h)*** *Normalized PL decay after the fast initial drop (at 500 ns for 'g' and 2 µs for 'h') using 3.49 eV (355 nm) pulsed excitation modulated at 2 kHz.*

absorption and PL spectra and that the overall optical behavior is independent from the incorporated Sb amount. Overall, based also on DFT calculations (Figure 4.3), can be concluded that the observed double-absorption peak characterizing both Sb-doped DP and Sb-doped 0D systems can be ascribed to the allowed transitions T_{1u} ($^3P_1$) at

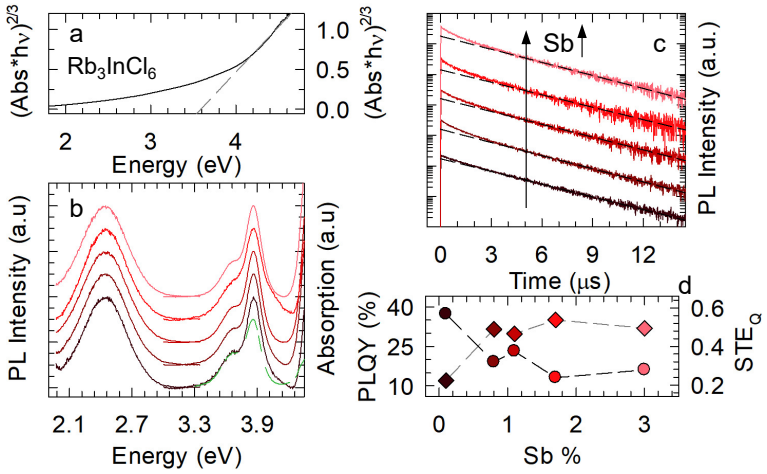

Figure 4.5: ***a)*** *Tauc plot for the undoped Rb_3InCl_6 NCs. The gray dashed lines represent the fit with the theoretical absorption profile of a semiconductor with a direct forbidden energy gap; the intercept with the abscissa axis corresponds to the semiconductor's forbidden gap energy.* ***b)*** *Absorption and PL spectra for the set of Sb-doped Rb_3InCl_6 NCs with increasing Sb concentration from the bottom to the top. PL excited with 3.87 eV (320 nm). A representative normalized PLE obtained for PL maxima is reported as a green dashed line.* ***c)*** *Set of normalized PL decays after the fast initial drop at 2 μs using 3.49 eV (355 nm) pulsed excitation modulated at 2 kHz. The Sb concentration increases from bottom to top. The black dashed lines are the fit with a single-exponential decay function excluding the first 3 μs.* ***d)*** *Absolute Φ_{PL} (circles) and the relative intensity of the STE_Q contribution (diamonds) - extracted from 'c' - as a function of the Sb amount.*

high energies (3.9 eV) and A_{1u} ($^3P_0$) at lower energies (3.7 eV). Notably, the computed oscillator strength for the lowest T_{1u} ($^3P_1$) transition ($f = 0.006$) corresponds to a radiative lifetime of 0.2 μs, in fair agreement with the observed lifetimes. The 0D systems with the lowest Sb content exhibited a Φ_{PL} of ~37%, nearly a factor of 2 higher than that of the DP NCs discussed earlier (Figure 4.5d). By increasing the Sb content, the Φ_{PL} decreased to ~14%, which is comparable to the highest value found for the DP systems, in line with the gradual activation of a concentration quenching channel, bringing the excitation closer to quenching centers. This picture is corroborated by time-resolved PL data (Figure 4.5c). Specifically, 0.1% Sb-doped NCs featured a nearly perfect single-exponential decay, with lifetime $\tau = 3.1$ μs. This component remained unvaried with increasing the Sb content which, on the other hand, caused the gradual growth of a faster decay component with $\tau = 0.9$ μs lifetime, ascribed to non-radiative quenching. Consistently, the relative weight of such a contribution (labeled STE_Q) to the total PL decay nearly perfectly anti-correlates with the respective

Φ_{PL} (Figure 4.5d), further supporting the hypothesis that such a kinetic effect is the signature of non-radiative quenching.

Overall, my optical analyses indicated that the optical features of both systems (DP and 0D) were very similar, with the main two differences being (*i*) the three sets of NCs studied ($Cs_2NaInCl_6$, Cs_2KInCl_6, and Rb_3InCl_6) all feature different Stokes shifts and (*ii*) the Φ_{PL} of our NCs are always much lower than their bulk counterparts, however with the 0D NCs performing considerably better than the DPs.

Further Modeling Refinements and Insights

To tentatively rationalized such findings, further computational efforts were made including the whole lattice for both the 3D ($Cs_2NaInCl_6$ and Cs_2KInCl_6) and 0D (Rb_3InCl_6) systems in the computational model; this is done by applying a 2×2×2 replication of their unit cells. The inherent variational nature pf DFT calculations prevents one from exploring energy states other than the lowest excited state for a given multiplicity of spins, and therefore from observing the optically active Sb states. To overcome this problem, the electronic structure of both the 3D and 0D systems is qualitatively followed while systematically elongating the axial Sb–Cl bonds, i.e., the bond that is partially broken upon photoexcitation, as it involves the occupation of just one of the three-fold-degenerate 5p(Sb)–3p(Cl) antibonding molecular orbitals. This models ultimately accounts for the Jahn–Teller distortion, i.e., the rupture of the t_{1u} degeneracy, and could extrapolate Stokes shift energies in the range of 1.1–1.3 eV, in agreement with the experiments. Larger Stokes shift observed for the K case could also stem from secondary distortion effects, like octahedron tilting, because the lattice cannot accommodate a full stretch of the Sb–Cl bond due to the larger size of K ions compared to Na.

This models also returns a picture of realistic loss mechanisms. Specifically, one can speculate that the photo-generated holes are transported from the $SbCl_6$ centers to the surface within the emission lifetime, thus providing an efficient channel of non-radiative recombination. While a precise estimate of the density of surface defects characterizing these systems would be extremely challenging, the optical analysis presented so far suggest that both 0D and 3D NCs could be characterized by a similar density of trap states, since at high doping levels the Φ_{PL} values for all systems tend to similar values. The visible difference in Φ_{PL} between the 0D and the 3D NC systems at low doping levels can then be ascribed to the fact that, in the 0D NCs, the hole carrier has to hop from one octahedron to another in order to reach a surface trap state, whereas in the 3D

NCs the connection between octahedra enhances the electron–phonon coupling effect via lattice vibrations, thus accelerating the non-radiative decay. In 0D NC systems, at higher doping levels the probability of a dopant to be closer to the NC's surface is statistically higher, meaning a higher chance for the STEs to reach a trap state, and thus to contribute to an overall lower Φ_{PL}. One can also speculate that an increase in NC size would not only lower the surface/volume ratio, thus the overall density of defect states, but also the probability of STEs reaching such traps, attaining eventually the Φ_{PL} values characterizing bulk systems. Calculation details are reported in Ref. [244].

Scintillation Measurements

To test the potential suitability of both Sb-doped DP and 0D perovskite NCs as re-absorption-free scintillator materials, I tested their radioluminescence (RL) emission and stability under prolonged continuous irradiation with soft X-rays and calculated the waveguiding properties of plastic scintillators embedding such NCs using Monte Carlo ray-tracing simulations. The RL spectra for 0.7% Sb-doped $Cs_2NaInCl_6$ and 0.9% Sb-doped Cs_2KInCl_6 NCs were dominated by peaks at ∼2.7 and ∼2.4 eV, respectively, which very well resembled the respective PL emissions (Figure 4.6a and 4.6c), thus indicating that the interaction with ionizing radiation creates the same excited states as UV optical excitation. Interestingly, the RL evidenced two additional minor spectral contributions at ∼2.1 and ∼4.2 eV, common to both samples, which can be attributed to the DP host matrix and possibly originating from the [$InCl_6$] octahedra present in both DP structures. The observation of such signals confirms the particular sensitivity of the RL technique to detect even minority emissions that are generally overlooked in PL experiments. The RL stability of these materials is presented in Figure 4.6b and 4.6d. For these experiments, the NC samples were exposed to continuous X-ray irradiation (dose rate of 0.5 Gy/s) up to almost 500 Gy of cumulated delivered dose. Remarkably, the RL intensities retained their initial value while the accumulated dose was increased, suggesting the absence of either competitive shallow traps for the Sb emissive excited states or damage to the NCs under prolonged exposure to X-rays. In stark contrast to the 3D DP systems, the RL spectrum of 0D 0.8% Sb-doped Rb_3InCl_6 NCs in Figure 4.6e was dominated by the host emissions at ∼2 and ∼4.2 eV (dashed gray line), while the Sb-related RL at 2.45 eV gave a minor contribution. Also in this case, the prolonged exposure to X-rays did not affect the RL intensity (Figure 4.6f).

Overall, the RL analyses indicate that only Sb-doped DPs NCs are promising candidates for scintillation applications, since most of their RL emission does not overlap

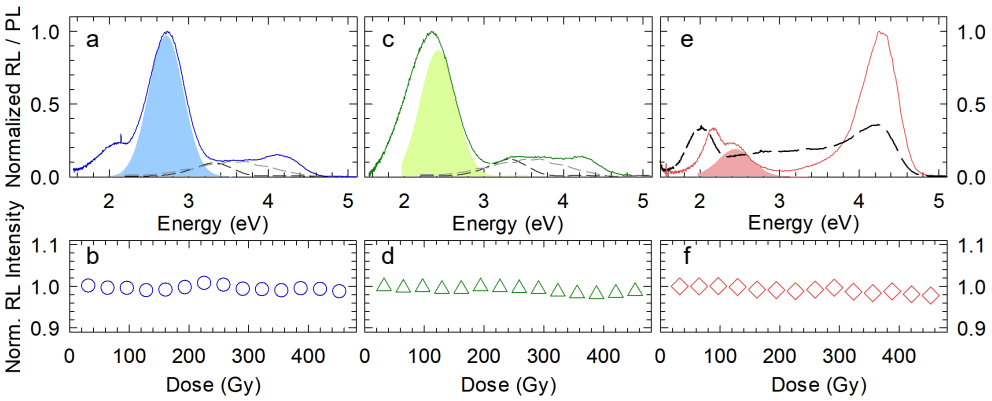

Figure 4.6: *RL spectra (solid lines) at room temperature excited using soft X-rays for representative samples of* ***(a)*** *0.7% Sb-doped $Cs_2NaInCl_6$,* ***(c)*** *0.9% Sb-doped Cs_2KInCl_6, and* ***(e)*** *0.8% Sb-doped Rb3InCl$_6$ NCs. The corresponding PL spectra from Figure 4.4 and 4.5 are shown as shaded curves. In* ***(a)*** *and* ***(c)****, the RL spectra of oleic acid and oleylamine are shown as black and gray curves, respectively. The dashed gray line in* ***(e)*** *is the RL spectrum of undoped Rb3InCl$_6$ NCs.* ***b, d, f)*** *Corresponding integrated RL intensities at increasing cumulative dose up to 500 Gy, with a dose rate of 0.5 Gy/s. Data are normalized to the initial value, and each data point represents the integral of the RL emission spectrum in the 1.8-3.0 eV range.*

with their absorption. We therefore simulated the waveguiding performance and expected quantum efficiency of square nanocomposite plastic scintillators (1 cm thick, lateral size from 10 × 10 cm to 2 × 2 m) made of poly(methyl methacrylate) (PMMA) embedding 10 *wt*% of $Cs_2NaInCl_6$ or Cs_2KInCl_6 NCs doped with Sb (0.7% and 0.9%, respectively). For the calculations, was used an emission quantum yield of 20%, consistent with the measured Φ_{PL}, and PMMA was chosen for its substantially higher transparency in the visible spectrum with respect to any other available polymer processable by the cell-casting method, which is necessary for producing optical-grade plastic waveguides. [32]

The absorption spectra of the nanocomposites (computed along the waveguide thickness) are reported in Figure 4.7a and 4.7b, showing, in both cases, the absorption edge of the NCs below ∼420 nm and the absorption overtones of the vibrational modes of the polymer matrix above 540 nm. The RL spectra emitted by the edges of the two scintillators are also reported for increasing device size (Figure 4.7a and 4.7b, dark to light colored lines), showing, for both NC systems, very small spectral overlap with the respective low-energy tail of the absorption spectrum. This results in negligible losses, due to re-absorption by the NCs, as quantified in Figure 4.7i and 4.7l, where is reported the evolution of the device quantum efficiency (QE, evaluated as the number of photons emitted from the waveguide edges divided by the number of

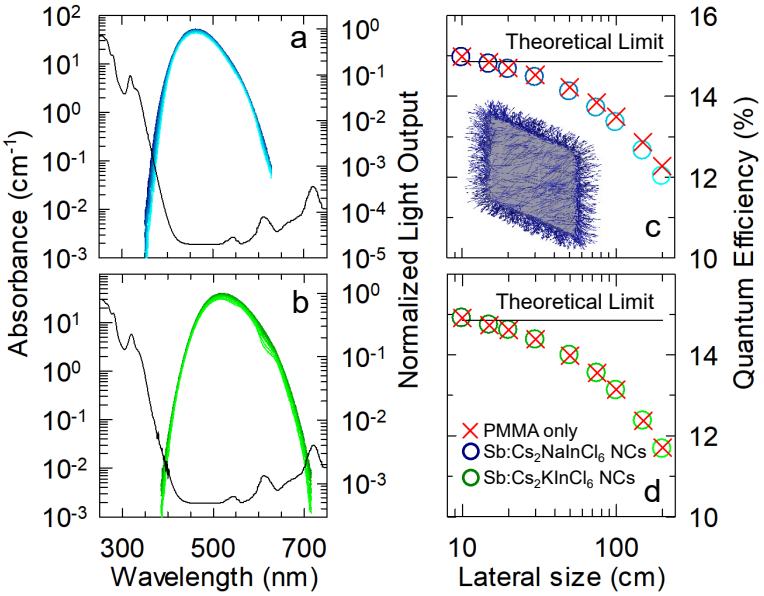

Figure 4.7: *Monte Carlo ray-tracing simulation of the RL spectra as a function of increasing device size (10 × 10 × 1 cm^3 to 2 × 2 m^2 × 1 cm, 10 wt%, from dark to light colored lines) calculated considering the experimental Φ_{PL} of 20% of* ***(a)*** *0.7% Sb-doped $Cs_2NaInCl_6$ and* ***(b)*** *0.9% Sb-doped Cs_2KInCl_6 NCs.* ***c, d)*** *Respective spectrally integrated RL intensities (circles) vs device size showing near-perfect coincidence with the trend, considering solely the re-absorption effect by the PMMA matrix (red crosses). Inset in (c): Visualization of Monte Carlo ray-tracing simulation for a plastic scintillator embedding Sb-doped $Cs_2NaInCl_6$.*

excitons generated inside the device upon exposure to high-energy radiation) with the waveguide size. In order to decouple NC and matrix effects, the same figure also shows the trend of the QE, considering exclusively the re-absorption of the propagating RL by PMMA, and the theoretical limit for waveguides embedding the same NCs content, but neglecting matrix effects (Figure 4.7i and 4.7l). Interestingly, for any scintillator size, the QE of the actual device (where the effect of both the NCs and the matrix is taken into account) closely matches the case considering exclusively PMMA, thus confirming the nearly perfect suppression of re-absorption in these DP systems. We further notice that, while K-based NCs suffer even lower re-absorption losses than the Na-based counterparts, the overall waveguiding properties of the two devices are nearly identical due to the stronger resonance between the RL of the Sb:Cs_2KInCl_6 NCs and the low-energy vibrational modes of the matrix. In either case, such a loss may be further suppressed by using fluorinated polymers. [32]

4.2.4 Summary

To summarize, in this section I reported the optical investigation of colloidal nanocrystals of Rb_3InCl_6 (0D) metal halide and of $Cs_2NaInCl_6$ and Cs_2KInCl_6 (3D) double perovskites and their doping with Sb^{3+} cations. All the Sb-doped nanocrystal systems show consistently lower PL than their bulk counterparts, a behavior that is ascribed to deep trap states originated by surface under-coordinated halide ions. Sb-doped "0D" Rb_3InCl_6 nanocrystals exhibit a higher Φ_{PL} compared to the Sb-doped "3D" $Cs_2NaInCl_6$ and Cs_2KInCl_6 ones. This finding is attributed to the different connectivity of metal halide octahedra characterizing 0D and 3D structures: isolated octahedra in the 0D structure reduce the exciton diffusion, thus minimizing non-radiative decay. The applicability of the systems as scintillator materials is assessed via RL measurements and corroborated by Monte Carlo ray-tracing simulations, highlighting their potential for re-absorption-free plastic scintillators of very large size. The excellent waveguiding capability found for these DP nanocrystals is particularly important for any light management technology based on wavelength-shifting waveguides and suggests a new, still unexplored route for Stokes shift engineering exploiting Jahn–Teller distortion upon photo-excitation. This study demonstrates once again that doping of various nanoscale metal halide systems can uncover interesting physics and deliver materials that can be useful in technological applications. The surface remains of paramount importance in all these systems, due to the much reduced tolerance compared to lead halide perovskites, and future synthetic strategies should aim to shore up this issue, for example, with proper ligand functionalization and/or growth of a large-bandgap inorganic shell similarly to what have been done for F-treated $CsPbBr_3$ NCs in Section 3.4.

Chapter 5

Conclusions and Further Work

The work reported in this thesis concerns the spectroscopic investigation of excitonic recombination mechanisms in colloidal semiconductor nanocrystals (NCs) and it is oriented towards the development of novel paradigms for real-world nanotechnologies. Thanks to the wide range of optical experiments and precious collaborations undertaken over the years of study our conclusions have been published in relevant scientific journals, contributing to the advancement of the community of materialist by tackling the open questions I presented in the previous chapters. My research mainly dealt with two topics of actual technological relevance: *i*) the investigation of the origin of the Stokes-shifted emission in ternary I-III-VI_2 chalcogenides such as $CuInS_2$ and $AgInS_2$, and *ii*) the employment of perovskites nanostructures in radiation detection or energy conversion schemes by introducing new strategies for near-zero auto-absorption losses and NC surface passivation which significantly boosted their technological potential.

I first proved through the combination of optical and magneto-optical experiments on a set of stoichiometric $CuInS_2$ NCs of different size the intrinsic origin of photoluminescence (PL), also supporting the valence-band model theoretically introduced by Dr. Alexander Efros and co-workers [34]. Specifically, the valence band (VB) features a low-energy odd parity hole sublevels of p-type symmetry separated by a splitting energy, Δ_{EO}, from higher-lying even parity hole levels, whose wavefunctions have s-type contributions. As a result of the parity selection rules, the absorption spectrum is dominated by the optical transition between the even hole VB sublevel and the $1S_e$ electron in conduction band. On the other hand, the PL arises from the parity-forbidden radiative transition of the $1S_e$ electron into the odd VB state, resulting in an intrinsically Stokes shifted luminescence proportional to Δ_{EO}. In this thesis, a combination

of ultra-fast transient transmission (TT) and steady state PL experiments revealed that the quadratic decrease (k_{RAD}) of the global Stoke-shift with the particle radius a, while via temperature-controlled time resolved PL experiments I extracted the purely radiative decay rate of our NCs finding, in perfect agreement with the model, that k_{RAD} linearly scales with a^2. The absence of intragap defect states is consistent with magnetic circular dichroism (MCD) experiments showing no *sp-d* exchange features due to paramagnetic Cu^{2+} states found in Cu-deficient NCs. Finally, the spectroscopic signature of further excitonic fine structure, visible below 50 K, is reported for the first time.

As the global Stokes-shift inversely scales with the squared particle's radius, this imposes a tradeoff between the extended solar spectrum harvesting of large nanoparticles and the reduced auto-absorption losses for smaller sizes. The impact of such results have been evaluated for technologically relevant case of large-area luminescent solar concentrators (LSC) where the optical performances of the waveguide is pivotal for the overall device performance. A Monte Carlo ray-tracing simulations, in collaboration with Glass To Power Spa, provided rational guidelines for the fabrication of a working LSC prototype embedding stoichiometric $CuInS_2$ NCs with optimal size in a PMMA polymeric matrix. The so fabricated device features no chromatic distortion of transmitted light and is thus suitable for architectural integration. Finally, thorough characterization of such a device revealed optical grade quality of the matrix and efficient NC emission, leading to an optical power efficiency as high as 6.8%, corresponding to the highest value reported to date for large-area LSC devices.

These results are then extended to another class of less investigated material, the $AgInS_2$ NCs, also featuring a heavy-metal-free composition and extremely large Stokes shifts which opens to numerous optoelectronic and photonic technologies also in biological environments. Here, combined MCD spectroscopies and temperature-dependent PL experiments corroborates the picture of the intrinsic origin of Stokes shifted PL also in $AgInS_2$ NCs, in agreement with the VB model [34]. More detailed insights into the structure of the absorption spectrum and the carrier dynamics are obtained by ultra-fast TT spectroscopy using a spectrally selective pump which unveiled the photohole localization mechanisms into the the odd-substate occurring in the pico-seconds timescale. Finally, spectro-electrochemical investigations reveals that surface electron trapping is the main nonradiative loss channel, that can be suppressed via electrochemical passivation of electron traps or by lowering the temperature to 3.5 K, leading to PL efficiencies close to unity.

Then I dedicated my research activities to the characterization of lead-halide perovskites (LHPs) nanostructures for ionizing radiation detection. To unlock their full potential as reliable and cost-effective alternatives to conventional scintillators, LHP urge to conjugate high scintillation yields with fast emission lifetime, Stokes-shifted emission to mitigate reabsorption losses in large/thick detectors, and emission stability over prolonged exposure to high doses of ionizing radiation. In this thesis these issues were addressed by performing, for the first time, a comprehensive study on $CsPbBr_3$ using radioluminescence (RL) and PL measurements side-by-side to thermally-stimulated luminescence (TSL) and afterglow experiments.

In continuity with the work done on LSCs with near zero self-absorption, first, has been tackled the technological problem of producing efficient and fast scintillators for large-area detectors. To do this $CsPbBr_3$ NCs are employed as high-Z sensitizers for a conjugated organic dye designed so as to exhibit a large Stokes shift and a fast emission lifetime also when embedded in a polymeric matrix. Efficient sensitization by the NCs is demonstrated in solution under selective optical excitation and, most crucially, in the PMMA nanocomposites under X-ray irradiation resulting in nearly 30-fold enhancement of the sensitized radioluminescence intensity with respect to the dyad alone. This approach, corroborated by Monte Carlo simulations, leads to the fabrication of the first example of low reabsorption, fast and efficient perovskite plastic scintillator showing performance approaching high-quality commercial plastic and bulk crystals scintillators both in terms of scintillation yield and emission lifetimes. Their applicability in real-world scenarios were also demonstrated by scintillation waveguiding measurements using ^{241}Am isotopes as α-particles sources, experimentally demonstrating the ability of our approach to detect charged particles over large surfaces with nearly no reabsorption losses.

To boost the light yield of LHPs and unlock their full potential, I performed an in-depth investigation of the scintillation mechanisms of $CsPbBr_3$, also as a function of the dimensionality of the particles (i.e. of the surface-to-volume ratio). A comprehensive study of temperature-controlled RL and PL measurements side-by-side to TSL and afterglow experiments on $CsPbBr_3$ revealed that all systems are found to be affected by shallow defects in thermal equilibrium with the band-edge exciton. This results in delayed intragap emission following detrapping via a-thermal tunneling. TSL further unveils the existence of additional, minor temperature-activated detrapping pathways from deeper trap states, whose effect grows with the material dimensionality, becoming the dominant process in bulk crystals. Overall, these results offered valuable insights for understanding and control of traps in the scintillation of LHP materials, and reaffirmed

the crucial role of surface defects, thus paving the way for future research oriented toward ionizing radiation detection applications.

Finally, with a view to systematically boost emission yield and to extend the use of $CsPbBr_3$ NCs in harsh environments, is demonstrated that post-synthetic resurfacing with fluorine ions passivates trap states at the NC surface leading to a ∼500% enhancement of the scintillation yield now matching with commercial bulk scintillator crystals. The extreme stability of $CsPbBr_3$ NCs was also tested in terms of radiation hardness for ^{60}Co γ-radiation doses as high as 1 MGy, the highest values reported so far for this class of NCs. Specifically, the PL and RL spectra of both standard and fluorinated $CsPbBr_3$ NCs are substantially identical at any γ-ray dose, across six orders of magnitude, indicating that the NCs retain their optical properties and no radiation-induced defects emerges up to 1 MGy dose. More importantly, the scintillation efficiency and the PL quantum yield of both types of NCs were found to be constant up to the highest irradiation dose. Trap-related phenomena were investigated trough TSL and afterglow measurements confirming that both NCs sets reveal no noticeable effect upon prolonged exposure to γ-rays. A deeper comparison between standard and F-treated NCs unveils substantial differences between their (de)trapping mechanisms with the $CsPbBr_3$:F NCs having a trap density ∼4-times lower than standard counterparts which make it possible to observe residual, very minor, deeper defects previously found in bulk crystals, which cannot be emptied except by providing the necessary thermal budget. These findings therefore bridge our knowledge of the scintillation physics of massive and nanoscale LHP and demonstrate that the low trap density characteristic of LHP massive solids can be realized also in nanoscale systems. This provides valuable guidelines for highly efficient and radiation hard detection designs produced via chemical methods, which substantially strengthen the potential of LHP nanostructures in real-world radiation detection schemes for high-energy physics, nuclear batteries, as well as in space-grade solar cells where high radiation hardness is critical for successful and long-running operation.

In the last chapter the spectroscopic investigation of novel class of lead-free double perovskite (DP) - emerging as environmental friendly alternative to conventional $CsPbX_3$ (X = Cl, ,Br, I) NCs - was reported. Specifically, the role of the connectivity of metal halide octahedra and its influence on the optical properties of Sb-doped materials was elucidated comparing $Cs_2NaInCl_6$ NCs, Cs_2KInCl_6 NCs (two different DP materials) and Rb_3InCl_6 NCs (a 0D system) at different Sb-dopant content. Optical absorption measurement revealed the dominant character of Sb atomic centers in

both 3D and 0D systems, while most differences lie in their emission features. The Sb-doped “0D” Rb_3InCl_6 NCs show a markedly higher Φ_{PL} (∼40%) than the corresponding Sb-doped “3D” DP ($Cs_2NaInCl_6$ and Cs_2KInCl_6) NCs (∼15–18%), although both present values well below those of the bulk crystal counterparts. This behavior has been explained in terms of different octahedra connectivity in the NC lattice with the "0D" case characterized by isolated [$SbCl_6$] octahedra limiting the self-trapped excitons (STEs) migration to defect-rich NC surface. In all these materials, the Stokes shift was found to depend strongly on the lattice cage that surrounds the [$SbCl_6$] octahedrons indicating that, as supported by computational insights, the emission wavelength can be (in principle) tuned on-demand by changing the type of B^+ ions.

Finally, motivated by their intense PL and large Stokes shifts, Sb-doped DP NCs were testes as re-absorption-free scintillators. RL measurements revealed intense scintillation emissions, closely matching their respective PL, retained up to 500 Gy of cumulative delivered dose. The applicability of DP systems was finally simulated via Monte Carlo ray-tracing calculations, promising essentially perfect waveguiding performance in large-area devices. The 0D NCs had instead a main RL originating from the host lattice which overlaps with their absorption profile making then unsuitable for large-area detectors. This result suggests a new, still unexplored materials design concept for Stokes shift engineering that exploits Jahn–Teller distortions upon photoexcitation of dopant-related emissive centers, with great potential for light management technologies based on wavelength-shifting waveguides.

List Of Publications

Here are the publications I worked on, indicating the personal contribution made for each. Items are listed from the most recent. Further unpublished contributions, under review at the time of the Thesis submission, have not been included.

1. Understanding Thermal and A-Thermal Trapping Processes in Lead Halide Perovskites Towards Effective Radiation Detection Schemes, *Rodà C.; Fasoli M.;* ***Zaffalon, M. L.****; Cova, F.; Pinchetti, V.; Shamsi, J.; Abdelhady, A. L.; Imran, M.; Meinardi, F.; Manna, L.; Vedda, A.; Brovelli, S.*, Advanced Functional Materials, 31, 43, 2104879, 2021.

   Performed steady-state and time-resolved optical spectroscopic measurements in a controlled temperature regime in the range 300 - 5 K. The collected data were analyzed demonstrating the thermal interplay between the band edge exciton and the shallow trap states.

2. Optical and Magneto-Optical Properties of Donor-Bound Excitons in Vacancy-Engineered Colloidal Nanocrystals, *Carulli, F.; Pinchetti, V.;* ***Zaffalon, M. L.****; Camellini, A.; Rotta Loria, S.; Moro, F.; Fanciulli, M.; Zavelani-Rossi, M.; Meinardi, F.; Crooker, S. A; Brovelli, S.*, American Chemical Society Nano letters, 21, 14, 6211-6219, 2021.

   Performed spectro-electrochemistry measurements to probe te effects of surface trap states on the PL intensity. The analysis of anodic currents and PL traces with the applied electrochemical potential, provided a good estimation of the Fermi energy level in our NCs, also demonstrating the existence of sulfur donor states $\sim$0.8 eV below the conduction band.

3. Sb-Doped Metal Halide Nanocrystals: A 0D versus 3D Comparison *Zhu, D.;* ***Zaffalon, M. L.****; Zito, J.; Cova, F.; Meinardi, F.; De Trizio, L.; Infante, I.; Brovelli, S.; Manna, L.*, ACS Energy Letters, 6, 2283-2292, 2021.

   Performed steady-state and time-resolved optical spectroscopic measurements.

The collected data were analyzed experimentally supporting theoretical predictions on radiative relaxation processes in isolated [SbCl6] octahedra. In collaboration with Dr. Cova, I also performed a RL survey on the most representative set of NCs suggesting that Sb-doped double perovskites are promising nanoscintillators with intrinsic Stokes shifted emission.

4. Intrinsic and Extrinsic Exciton Recombination Pathways in AgInS2 Colloidal Nanocrystals, ***Zaffalon, M. L.***; *Pinchetti, V.; Camellini, A.; Vikulov, S.; Capitani, C.; Bai, B.; Xu, M.; Meinardi, F.; Zhang, J.; Manna, L.; Zavelani-Rossi, M.; Crooker, S. A.; Brovelli, S.*, Energy Material Advances, Vol 2021, 2021.

   First author: performed all spectroscopic measurements and data analysis.

5. Bright Blue Emitting Cu-doped Cs2ZnCl4 Colloidal Nanocrystals, *Zhu, D.;* ***Zaffalon, M. L.***; *Pinchetti, V.; Brescia, R.; Moro, F.; Fasoli, M.; Fanciulli, M.; Tang, A.; Infante, I.; De Trizio, L.; Brovelli, S.; Manna, L.*, Chemistry of Materials, 32, 13, 5897-5903, 2020.

   Performed steady-state and time-resolved optical spectroscopic measurements proving insights on the recombination mechanisms from tetrahedral coordinated Cu sites.

6. Efficient, fast and reabsorption-free perovskite nanocrystal-based sensitized plastic scintillators, *Gandini, M.; Villa, I.; Beretta, M.; Gotti, C.; Imran, M.; Carulli, F.; Fantuzzi, E.; Sassi, M.;* ***Zaffalon, M. L.***; *Brofferio, C.; Manna, L.; Beverina, L.; Vedda, A.; Fasoli, M.; Gironi, L.; Brovelli, S.*,Nature Nanotechnology, 15, 6, 462-468, 2020.

   Performed time-resolved PL measurements on CsPbBr3 NCs while progressively adding **1** dye in solution. The results confirmed the occurrence of an energy transfer process from the LPH to the organic dye.

7. Evidence for the Band-Edge Exciton of CuInS2 Nanocrystals Enables Record Efficient Large-Area Luminescent Solar Concentrators, *Anand, A.;* ***Zaffalon, M. L.***; *Gariano, G.; Camellini, A.; Gandini, M.; Brescia, R.; Capitani, C.; Bruni, F.; Pinchetti, V.; Zavelani-Rossi, M.; Meinardi, F.; Crooker, S. A.; Brovelli, S.*, Advanced Functional Materials, 1906629, 2019.

   First author: performed all spectroscopic measurements and data analysis in collaboration with Dr. Anand.

Bibliography

[1] J. M. Pietryga, Y. S. Park, J. Lim, A. F. Fidler, W. K. Bae, S. Brovelli, and V. I. Klimov, "Spectroscopic and device aspects of nanocrystal quantum dots," *Chemical Reviews*, vol. 116, pp. 10513–10622, sep 2016.

[2] V. Klimov, *Nanocrystal Quantum Dots*, vol. 134. 2007.

[3] D. H. Jara, S. J. Yoon, K. G. Stamplecoskie, and P. V. Kamat, "Size-Dependent Photovoltaic Performance of CuInS2 Quantum Dot-Sensitized Solar Cells," *Chemistry of Materials*, vol. 26, pp. 7221–7228, dec 2014.

[4] V. R. Voggu, J. Sham, S. Pfeffer, J. Pate, L. Fillip, T. B. Harvey, R. M. Brown, and B. A. Korgel, "Flexible CuInSe2 nanocrystal solar cells on paper," *ACS Energy Letters*, vol. 2, no. 3, pp. 574–581, 2017.

[5] J. E. Halpert, F. S. Morgenstern, B. Ehrler, Y. Vaynzof, D. Credgington, and N. C. Greenham, "Charge Dynamics in Solution-Processed Nanocrystalline CuInS2 Solar Cells," *ACS Nano*, vol. 9, pp. 5857–5867, jun 2015.

[6] I. Levchuk, C. Würth, F. Krause, A. Osvet, M. Batentschuk, U. Resch-Genger, C. Kolbeck, P. Herre, H. P. Steinrück, W. Peukert, and C. J. Brabec, "Industrially scalable and cost-effective Mn2+ doped ZnxCd1-xS/ZnS nanocrystals with 70% photoluminescence quantum yield, as efficient down-shifting materials in photovoltaics," *Energy and Environmental Science*, vol. 9, no. 3, pp. 1083–1094, 2016.

[7] J. Tang, S. Hinds, S. O. Kelley, and E. H. Sargent, "Synthesis of colloidal CuGaSe2, CuInSe2, and Cu(InGa)Se2 nanoparticles," *Chemistry of Materials*, vol. 20, pp. 6906–6910, nov 2008.

[8] S. M. Kobosko and P. V. Kamat, "Indium-Rich AgInS2-ZnS Quantum Dots - Ag-/Zn-Dependent Photophysics and Photovoltaics," *Journal of Physical Chemistry C*, vol. 122, no. 26, pp. 14336–14344, 2018.

[9] F. Meinardi, H. McDaniel, F. Carulli, A. Colombo, K. A. Velizhanin, N. S. Makarov, R. Simonutti, V. I. Klimov, and S. Brovelli, "Highly efficient large-area colourless luminescent solar concentrators using heavy-metal-free colloidal quantum dots," *Nature Nanotechnology*, vol. 10, no. 10, pp. 878–885, 2015.

[10] K. Wu, H. Li, and V. I. Klimov, "Tandem luminescent solar concentrators based on engineered quantum dots," *Nature Photonics*, vol. 12, no. 2, pp. 105–110, 2018.

[11] C. Li, W. Chen, D. Wu, D. Quan, Z. Zhou, J. Hao, J. Qin, Y. Li, Z. He, and K. Wang, "Large Stokes Shift and High Efficiency Luminescent Solar Concentrator Incorporated with CuInS 2 /ZnS Quantum Dots," *Scientific Reports*, vol. 5, 2015.

[12] M. R. Bergren, N. S. Makarov, K. Ramasamy, A. Jackson, R. Guglielmetti, and H. McDaniel, "High-Performance CuInS2 Quantum Dot Laminated Glass Luminescent Solar Concentrators for Windows," *ACS Energy Letters*, vol. 3, pp. 520–525, mar 2018.

[13] Z. Bai, W. Ji, D. Han, L. Chen, B. Chen, H. Shen, B. Zou, and H. Zhong, "Hydroxyl-Terminated CuInS 2 Based Quantum Dots: Toward Efficient and Bright Light Emitting Diodes," *Chemistry of Materials*, vol. 28, pp. 1085–1091, feb 2016.

[14] B. Chen, H. Zhong, W. Zhang, Z. Tan, Y. Li, C. Yu, T. Zhai, Y. Bando, S. Yang, and B. Zou, "Highly emissive and color-tunable CuInS 2-based colloidal semiconductor nanocrystals: Off-stoichiometry effects and improved electroluminescence performance," *Advanced Functional Materials*, vol. 22, pp. 2081–2088, may 2012.

[15] W. Zhang, Q. Lou, W. Ji, J. Zhao, and X. Zhong, "Color-tunable highly bright photoluminescence of cadmium-free cu-doped Zn-In-S nanocrystals and electroluminescence," *Chemistry of Materials*, vol. 26, no. 2, pp. 1204–1212, 2014.

[16] D. Aldakov, A. Lefrançois, and P. Reiss, "Ternary and quaternary metal chalcogenide nanocrystals: synthesis, properties and applications," *Journal of Materials Chemistry C*, vol. 1, no. 24, p. 3756, 2013.

[17] Z. Tan, Y. Zhang, C. Xie, H. Su, J. Liu, C. Zhang, N. Dellas, S. E. Mohney, Y. Wang, J. Wang, and J. Xu, "Near-band-edge electroluminescence from heavy-metal-free colloidal quantum dots," *Advanced Materials*, vol. 23, pp. 3553–3558, aug 2011.

[18] J. Kolny-Olesiak and H. Weller, "Synthesis and application of colloidal CuInS2 semiconductor nanocrystals," *ACS Applied Materials and Interfaces*, vol. 5, pp. 12221–12237, dec 2013.

[19] M. G. Panthani, T. A. Khan, D. K. Reid, D. J. Hellebusch, M. R. Rasch, J. A. Maynard, and B. A. Korgel, "In vivo whole animal fluorescence imaging of a microparticle-based oral vaccine containing (CuInSexS2- x)/ZnS core/shell quantum dots," *Nano Letters*, vol. 13, no. 9, pp. 4294–4298, 2013.

[20] Z. Sun, G. Sitbon, T. Pons, A. A. Bakulin, and Z. Chen, "Reduced carrier recombination in PbS-CuInS 2 quantum dot solar cells," *Scientific Reports*, vol. 5, 2015.

[21] H. J. Yun, J. Lim, A. S. Fuhr, N. S. Makarov, S. Keene, M. Law, J. M. Pietryga, and V. I. Klimov, "Charge-Transport Mechanisms in CuInSe x S 2-x Quantum-Dot Films," *ACS Nano*, vol. 12, pp. 12587–12596, dec 2018.

[22] A. Singh, C. Coughlan, D. J. Milliron, and K. M. Ryan, "Solution synthesis and assembly of wurtzite-derived Cu-In-Zn-S nanorods with tunable composition and band gap," *Chemistry of Materials*, vol. 27, pp. 1517–1523, mar 2015.

[23] L. De Trizio, M. Prato, A. Genovese, A. Casu, M. Povia, R. Simonutti, M. J. Alcocer, C. D'Andrea, F. Tassone, and L. Manna, "Strongly fluorescent quaternary Cu-In-Zn-S nanocrystals prepared from Cu 1-xInS 2 nanocrystals by partial cation exchange," *Chemistry of Materials*, vol. 24, pp. 2400–2406, jun 2012.

[24] O. Yarema, D. Bozyigit, I. Rousseau, L. Nowack, M. Yarema, W. Heiss, and V. Wood, "Highly luminescent, size- and shape-tunable copper indium selenide based colloidal nanocrystals," *Chemistry of Materials*, vol. 25, no. 18, pp. 3753–3757, 2013.

[25] J. F. Lox, Z. Dang, V. M. Dzhagan, D. Spittel, B. Martín-García, I. Moreels, D. R. Zahn, and V. Lesnyak, "Near-Infrared Cu-In-Se-Based Colloidal Nanocrystals via Cation Exchange," *Chemistry of Materials*, vol. 30, pp. 2607–2617, apr 2018.

[26] H. Zhong, S. S. Lo, T. Mirkovic, Y. Li, Y. Ding, Y. Li, and G. D. Scholes, "Non-injection gram-scale synthesis of monodisperse pyramidal CuInS 2 nanocrystals and their size-dependent properties," *ACS Nano*, vol. 4, pp. 5253–5262, sep 2010.

[27] C. Xia, J. D. Meeldijk, H. C. Gerritsen, and C. De Mello Donega, "Highly Luminescent Water-Dispersible NIR-Emitting Wurtzite CuInS2/ZnS Core/Shell Colloidal Quantum Dots," *Chemistry of Materials*, vol. 29, pp. 4940–4951, jun 2017.

[28] L. Li, A. Pandey, D. J. Werder, B. P. Khanal, J. M. Pietryga, and V. I. Klimov, "Efficient synthesis of highly luminescent copper indium sulfide-based core/shell nanocrystals with surprisingly long-lived emission," *Journal of the American Chemical Society*, vol. 133, no. 5, pp. 1176–1179, 2011.

[29] H. Zhong, Z. Bai, and B. Zou, "Tuning the luminescence properties of colloidal I-III-VI semiconductor nanocrystals for optoelectronics and biotechnology applications," *Journal of Physical Chemistry Letters*, vol. 3, pp. 3167–3175, nov 2012.

[30] X. Hu, R. Kang, Y. Zhang, L. Deng, H. Zhong, B. Zou, and L.-J. Shi, "Ray-trace simulation of CuInS(Se)2 quantum dot based luminescent solar concentrators," *Optics Express*, vol. 23, no. 15, p. A858, 2015.

[31] K. E. Knowles, T. B. Kilburn, D. G. Alzate, S. McDowall, and D. R. Gamelin, "Bright CuInS2/CdS nanocrystal phosphors for high-gain full-spectrum luminescent solar concentrators," *Chemical Communications*, vol. 51, no. 44, pp. 9129–9132, 2015.

[32] F. Meinardi, F. Bruni, and S. Brovelli, "Luminescent solar concentrators for building-integrated photovoltaics," *Nature Reviews Materials*, vol. 2, p. 17072, dec 2017.

[33] A. C. Berends, M. J. J. Mangnus, C. Xia, F. T. Rabouw, and C. de Mello Donega, "Optoelectronic Properties of Ternary I–III–VI 2 Semiconductor Nanocrystals: Bright Prospects with Elusive Origins," *The Journal of Physical Chemistry Letters*, vol. 10, pp. 1600–1616, apr 2019.

[34] A. Shabaev, M. J. Mehl, and A. L. Efros, "Energy band structure of CuInS2 and optical spectra of CuInS2 nanocrystals," *Physical Review B*, vol. 92, no. 3, p. 035431, 2015.

[35] K. E. Knowles, H. D. Nelson, T. B. Kilburn, and D. R. Gamelin, "Singlet-triplet splittings in the luminescent excited states of colloidal Cu+:CdSe, Cu+:InP, and CuInS2 nanocrystals: Charge-transfer configurations and self-trapped excitons," *Journal of the American Chemical Society*, vol. 137, no. 40, pp. 13138–13147, 2015.

[36] K. E. Hughes, S. R. Ostheller, H. D. Nelson, and D. R. Gamelin, "Copper's role in the photoluminescence of Ag1-xCuxInS2nanocrystals, from copper-doped AgInS2(x $\sim$ 0) to CuInS2(x = 1)," *Nano Letters*, vol. 19, pp. 1318–1325, feb 2019.

[37] V. Pinchetti, Q. Di, M. Lorenzon, A. Camellini, M. Fasoli, M. Zavelani-Rossi, F. Meinardi, J. Zhang, S. A. Crooker, and S. Brovelli, "Excitonic pathway to photoinduced magnetism in colloidal nanocrystals with nonmagnetic dopants," *Nature Nanotechnology*, vol. 13, pp. 145–151, feb 2018.

[38] A. D. Leach and J. E. Macdonald, "Optoelectronic Properties of CuInS2 Nanocrystals and Their Origin," *Journal of Physical Chemistry Letters*, vol. 7, no. 3, pp. 572–583, 2016.

[39] W. Hu, J. Ludwig, B. Pattengale, S. Yang, C. Liu, X. Zuo, X. Zhang, and J. Huang, "Unravelling the Correlation of Electronic Structure and Carrier Dynamics in CuInS 2 Nanoparticles," *The Journal of Physical Chemistry C*, vol. 122, pp. 974–980, jan 2018.

[40] C. Xia, W. Wu, T. Yu, X. Xie, C. van Oversteeg, H. C. Gerritsen, and C. de Mello Donega, "Size-Dependent Band-Gap and Molar Absorption Coefficients of Colloidal CuInS 2 Quantum Dots," *ACS Nano*, vol. 12, pp. 8350–8361, aug 2018.

[41] A. C. Berends, F. T. Rabouw, F. C. Spoor, E. Bladt, F. C. Grozema, A. J. Houtepen, L. D. Siebbeles, and C. De Mello Donegá, "Radiative and Nonradiative Recombination in CuInS2 Nanocrystals and CuInS2-Based Core/Shell Nanocrystals," *Journal of Physical Chemistry Letters*, vol. 7, no. 17, pp. 3503–3509, 2016.

[42] H. Zang, H. Li, N. S. Makarov, K. A. Velizhanin, K. Wu, Y.-S. Park, and V. I. Klimov, "Thick-Shell CuInS 2 /ZnS Quantum Dots with Suppressed "Blinking" and Narrow Single-Particle Emission Line Widths," *Nano Letters*, vol. 17, pp. 1787–1795, mar 2017.

[43] V. Pinchetti, M. Lorenzon, H. McDaniel, R. Lorenzi, F. Meinardi, V. I. Klimov, and S. Brovelli, "Spectro-electrochemical Probing of Intrinsic and Extrinsic Processes in Exciton Recombination in I–III–VI 2 Nanocrystals," *Nano Letters*, vol. 17, pp. 4508–4517, jul 2017.

[44] A. S. Fuhr, H. J. Yun, N. S. Makarov, H. Li, H. McDaniel, and V. I. Klimov, "Light Emission Mechanisms in CuInS 2 Quantum Dots Evaluated by Spectral Electrochemistry," *ACS Photonics*, vol. 4, pp. 2425–2435, oct 2017.

[45] W. van der Stam, M. de Graaf, S. Gudjonsdottir, J. J. Geuchies, J. J. Dijkema, N. Kirkwood, W. H. Evers, A. Longo, and A. J. Houtepen, "Tuning and Probing the Distribution of Cu + and Cu 2+ Trap States Responsible for Broad-Band Photoluminescence in CuInS 2 Nanocrystals," *ACS Nano*, vol. 12, pp. 11244–11253, nov 2018.

[46] W. D. Rice, H. McDaniel, V. I. Klimov, and S. A. Crooker, "Magneto-Optical Properties of CuInS 2 Nanocrystals," *The Journal of Physical Chemistry Letters*, vol. 5, pp. 4105–4109, dec 2014.

[47] A. Pandey, S. Brovelli, R. Viswanatha, L. Li, J. M. Pietryga, V. I. Klimov, and S. A. Crooker, "Long-lived photoinduced magnetization in copper-doped ZnSe-CdSe core-shell nanocrystals," *Nature Nanotechnology*, vol. 7, no. 12, pp. 792–797, 2012.

[48] W. Liu, Y. Zhang, W. Zhai, Y. Wang, T. Zhang, P. Gu, H. Chu, H. Zhang, T. Cui, Y. Wang, J. Zhao, and W. W. Yu, "Temperature-dependent photoluminescence of ZnCuInS/ZnSe/ZnS quantum dots," *Journal of Physical Chemistry C*, vol. 117, pp. 19288–19294, sep 2013.

[49] D. W. Houck, E. I. Assaf, H. Shin, R. M. Greene, D. R. Pernik, and B. A. Korgel, "Pervasive cation vacancies and antisite defects in copper indium diselenide (CuInSe2) nanocrystals," *Journal of Physical Chemistry C*, vol. 123, no. 14, pp. 9544–9551, 2019.

[50] I. T. Kraatz, M. Booth, B. J. Whitaker, M. G. Nix, and K. Critchley, "Subbandgap emission and intraband defect-related excited-state dynamics in colloidal CuInS2/ZnS quantum dots revealed by femtosecond pump-dump-probe spectroscopy," *Journal of Physical Chemistry C*, vol. 118, pp. 24102–24109, oct 2014.

[51] H. D. Nelson and D. R. Gamelin, "Valence-Band Electronic Structures of Cu + -Doped ZnS, Alloyed Cu–In–Zn–S, and Ternary CuInS 2 Nanocrystals: A Unified Description of Photoluminescence across Compositions," *The Journal of Physical Chemistry C*, vol. 122, pp. 18124–18133, aug 2018.

[52] G. Nagamine, H. B. Nunciaroni, H. McDaniel, A. L. Efros, C. H. De Brito Cruz, and L. A. Padilha, "Evidence of Band-Edge Hole Levels Inversion in Spherical CuInS2Quantum Dots," *Nano Letters*, vol. 18, pp. 6353–6359, 2018.

[53] G. K. Grandhi and R. Viswanatha, "Tunable infrared phosphors using Cu doping in semiconductor nanocrystals: Surface electronic structure evaluation," *Journal of Physical Chemistry Letters*, vol. 4, pp. 409–415, feb 2013.

[54] R. Viswanatha, S. Brovelli, A. Pandey, S. A. Crooker, and V. I. Klimov, "Copper-Doped Inverted Core/Shell Nanocrystals with "Permanent" Optically Active Holes," *Nano Letters*, vol. 11, pp. 4753–4758, nov 2011.

[55] S. A. Crooker, T. Barrick, J. A. Hollingsworth, and V. I. Klimov, "Multiple temperature regimes of radiative decay in CdSe nanocrystal quantum dots: Intrinsic limits to the dark-exciton lifetime," *Applied Physics Letters*, vol. 82, pp. 2793–2795, apr 2003.

[56] M. Nirmal, D. J. Norris, M. Kuno, M. G. Bawendi, A. L. Efros, and M. Rosen, "Observation of the "dark exciton" in CdSe quantum dots," *Physical Review Letters*, vol. 75, no. 20, pp. 3728–3731, 1995.

[57] A. L. Efros, M. Rosen, M. Kuno, M. Nirmal, D. Norris, and M. Bawendi, "Band-edge exciton in quantum dots of semiconductors with a degenerate valence band: Dark and bright exciton states," *Physical Review B - Condensed Matter and Materials Physics*, vol. 54, no. 7, pp. 4843–4856, 1996.

[58] R. Romestain and G. Fishman, "Excitonic wave function, correlation energy, exchange energy, and oscillator strength in a cubic quantum dot," *Physical Review B*, vol. 49, no. 3, pp. 1774–1781, 1994.

[59] H. Zhong, Y. Zhou, M. Ye, Y. He, J. Ye, C. He, C. Yang, and Y. Li, "Controlled synthesis and optical properties of colloidal ternary chalcogenide CuInS2 nanocrystals," *Chemistry of Materials*, vol. 20, pp. 6434–6443, oct 2008.

[60] D. E. Nam, W. S. Song, and H. Yang, "Noninjection, one-pot synthesis of Cu-deficient CuInS2/ZnS core/shell quantum dots and their fluorescent properties," *Journal of Colloid and Interface Science*, vol. 361, no. 2, pp. 491–496, 2011.

[61] M. Booth, A. P. Brown, S. D. Evans, and K. Critchley, "Determining the concentration of CuInS 2 quantum dots from the size-dependent molar extinction coefficient," *Chemistry of Materials*, vol. 24, pp. 2064–2070, jun 2012.

[62] D. A. Bussian, S. A. Crooker, M. Yin, M. Brynda, A. L. Efros, and V. I. Klimov, "Tunable magnetic exchange interactions in manganese-doped inverted core–shell ZnSe–CdSe nanocrystals," *Nature Materials*, vol. 8, pp. 35–40, jan 2009.

[63] R. Xie, M. Rutherford, and X. Peng, "Formation of High-Quality I-III-VI Semiconductor Nanocrystals by Tuning Relative Reactivity of Cationic Precursors," *Journal of the American Chemical Society*, vol. 131, pp. 5691–5697, apr 2009.

[64] C. Capitani, V. Pinchetti, G. Gariano, B. Santiago-González, C. Santambrogio, M. Campione, M. Prato, R. Brescia, A. Camellini, F. Bellato, F. Carulli, A. Anand, M. Zavelani-Rossi, F. Meinardi, S. A. Crooker, and S. Brovelli, "Quantized Electronic Doping towards Atomically Controlled "charge-Engineered" Semiconductor Nanocrystals," *Nano Letters*, vol. 19, no. 2, pp. 1307–1317, 2019.

[65] B. K. Ridley, *Quantum Processes in Semiconductors*. Oxford University Press, aug 2013.

[66] J. H. Blokland, V. I. Claessen, F. J. Wijnen, E. Groeneveld, C. De Mello Donegá, D. Vanmaekelbergh, A. Meijerink, J. C. Maan, and P. C. Christianen, "Exciton lifetimes of CdTe nanocrystal quantum dots in high magnetic fields," *Physical Review B - Condensed Matter and Materials Physics*, vol. 83, jan 2011.

[67] J. Eilers, J. Van Hest, A. Meijerink, and C. D. M. Donega, "Unravelling the size and temperature dependence of exciton lifetimes in colloidal ZnSe quantum dots," *Journal of Physical Chemistry C*, vol. 118, pp. 23313–23319, oct 2014.

[68] A. Granados Del Águila, E. Groeneveld, J. C. Maan, C. De Mello Donegá, and P. C. Christianen, "Effect of Electron-Hole Overlap and Exchange Interaction on Exciton Radiative Lifetimes of CdTe/CdSe Heteronanocrystals," *ACS Nano*, vol. 10, no. 4, pp. 4102–4110, 2016.

[69] S. Brovelli, R. Schaller, S. Crooker, F. García-Santamaría, Y. Chen, R. Viswanatha, J. Hollingsworth, H. Htoon, and V. Klimov, "Nano-engineered electron–hole exchange interaction controls exciton dynamics in core–shell semiconductor nanocrystals," *Nature Communications*, vol. 2, p. 280, sep 2011.

[70] D. Oron, A. Aharoni, C. De Mello Donega, J. Van Rijssel, A. Meijerink, and U. Banin, "Universal role of discrete acoustic phonons in the low-temperature optical emission of colloidal quantum dots," *Physical Review Letters*, vol. 102, apr 2009.

[71] C. Robert, T. Amand, F. Cadiz, D. Lagarde, E. Courtade, M. Manca, T. Taniguchi, K. Watanabe, B. Urbaszek, and X. Marie, "Fine structure and lifetime of dark excitons in transition metal dichalcogenide monolayers," *Physical Review B*, vol. 96, oct 2017.

[72] M. G. Debije, C. Tzikas, V. A. Rajkumar, and M. M. de Jong, "The solar noise barrier project: 2. The effect of street art on performance of a large scale luminescent solar concentrator prototype," *Renewable Energy*, vol. 113, pp. 1288–1292, 2017.

[73] N. Aste, L. C. Tagliabue, C. Del Pero, D. Testa, and R. Fusco, "Performance analysis of a large-area luminescent solar concentrator module," *Renewable Energy*, vol. 76, pp. 330–337, 2015.

[74] M. G. Debije, "Solar energy collectors with tunable transmission," *Advanced Functional Materials*, vol. 20, pp. 1498–1502, may 2010.

[75] R. Lesyuk, V. Lesnyak, A. Herguth, D. Popovych, Y. Bobitski, C. Klinke, and N. Gaponik, "Simulation study of environmentally friendly quantum-dot-based photovoltaic windows," *Journal of Materials Chemistry C*, vol. 5, no. 45, pp. 11790–11797, 2017.

[76] M. Uehara, K. Watanabe, Y. Tajiri, H. Nakamura, and H. Maeda, "Synthesis of CuInS2 fluorescent nanocrystals and enhancement of fluorescence by controlling crystal defect," *Journal of Chemical Physics*, vol. 129, no. 13, 2008.

[77] F. Meinardi, S. Ehrenberg, L. Dhamo, F. Carulli, M. Mauri, F. Bruni, R. Simonutti, U. Kortshagen, and S. Brovelli, "Highly efficient luminescent solar concentrators based on earth-Abundant indirect-bandgap silicon quantum dots," *Nature Photonics*, vol. 11, no. 3, pp. 177–185, 2017.

[78] Y. Gromova, A. Sokolova, D. Kurshanov, I. Korsakov, V. Osipova, S. Cherevkov, A. Dubavik, V. Maslov, T. Perova, Y. Gun'ko, A. Baranov, and A. Fedorov, "Investigation of AgInS2/ZnS Quantum Dots by Magnetic Circular Dichroism Spectroscopy," *Materials*, vol. 12, p. 3616, nov 2019.

[79] B. Mao, C.-h. Chuang, J. Wang, and C. Burda, "Synthesis and Photophysical Properties of Ternary I–III–VI AgInS 2 Nanocrystals: Intrinsic versus Surface States," *The Journal of Physical Chemistry C*, vol. 115, pp. 8945–8954, may 2011.

[80] S. O. Hinterding, M. J. Mangnus, P. T. Prins, H. J. Jöbsis, S. Busatto, D. Vanmaekelbergh, C. De Mello Donega, and F. T. Rabouw, "Unusual Spectral Diffusion of Single CuInS2Quantum Dots Sheds Light on the Mechanism of Radiative Decay," *Nano Letters*, vol. 21, pp. 658–665, jan 2021.

[81] R. D. Schaller, S. M. Harvey, D. W. Houck, M. S. Kirschner, N. C. Flanders, A. Brumberg, A. A. Leonard, N. E. Watkins, L. X. Chen, W. R. Dichtel, X. Zhang, B. A. Korgel, and M. R. Wasielewski, "Transient lattice response upon photoexcitation in CuInSe2 nanocrystals with organic or inorganic surface passivation," *ACS Nano*, vol. 14, pp. 13548–13556, oct 2020.

[82] A. S. Baimuratov, I. V. Martynenko, A. V. Baranov, A. V. Fedorov, I. D. Rukhlenko, and S. Y. Kruchinin, "Giant Stokes Shifts in AgInS2 Nanocrystals with Trapped Charge Carriers," *Journal of Physical Chemistry C*, vol. 123, no. 26, pp. 16430–16438, 2019.

[83] A. Anand, M. L. Zaffalon, G. Gariano, A. Camellini, M. Gandini, R. Brescia, C. Capitani, F. Bruni, V. Pinchetti, M. Zavelani-Rossi, F. Meinardi, S. A. Crooker, and S. Brovelli, "Evidence for the Band-Edge Exciton of CuInS2 Nanocrystals Enables Record Efficient Large-Area Luminescent Solar Concentrators," *Advanced Functional Materials*, vol. 30, no. 4, pp. 1–13, 2020.

[84] T. Kameyama, T. Takahashi, T. Machida, Y. Kamiya, T. Yamamoto, S. Kuwabata, and T. Torimoto, "Controlling the Electronic Energy Structure of ZnS-AgInS2 Solid Solution Nanocrystals for Photoluminescence and Photocatalytic Hydrogen Evolution," *Journal of Physical Chemistry C*, vol. 119, no. 44, pp. 24740–24749, 2015.

[85] J. Liu, Q. Zhao, J.-l. Liu, Y.-s. Wu, Y. Cheng, M.-w. Ji, H.-m. Qian, W.-c. Hao, L.-J. Zhang, X.-j. Wei, S.-g. Wang, J.-t. Zhang, Y. Du, S.-X. Dou, and H.-S. Zhu, "Heterovalent-Doping-Enabled Efficient Dopant Luminescence and Controllable Electronic Impurity Via a New Strategy of Preparing II-VI Nanocrystals," *Advanced Materials*, vol. 27, pp. 2753–2761, may 2015.

[86] N. Samarth and J. K. Furdyna, "Diluted Magnetic Semiconductors," *MRS Bulletin*, vol. 13, no. 6, pp. 32–36, 1988.

[87] Y. Hamanaka, T. Ogawa, M. Tsuzuki, and T. Kuzuya, "Photoluminescence properties and its origin of AgInS2 quantum dots with chalcopyrite structure," *Journal of Physical Chemistry C*, vol. 115, no. 5, pp. 1786–1792, 2011.

[88] O. Stroyuk, F. Weigert, A. Raevskaya, F. Spranger, C. Würth, U. Resch-Genger, N. Gaponik, and D. R. Zahn, "Inherently Broadband Photoluminescence in Ag-In-S/ZnS Quantum Dots Observed in Ensemble and Single-Particle Studies," *Journal of Physical Chemistry C*, vol. 123, no. 4, pp. 2632–2641, 2019.

[89] P. J. Whitham, A. Marchioro, K. E. Knowles, T. B. Kilburn, P. J. Reid, and D. R. Gamelin, "Single-particle photoluminescence spectra, blinking, and delayed luminescence of colloidal CuInS2nanocrystals," *Journal of Physical Chemistry C*, vol. 120, no. 30, pp. 17136–17142, 2016.

[90] D. K. Sharma, S. Hirata, L. Bujak, V. Biju, T. Kameyama, M. Kishi, T. Torimoto, and M. Vacha, "Single-particle spectroscopy of I-III-VI semiconductor nanocrystals: Spectral diffusion and suppression of blinking by two-color excitation," *Nanoscale*, vol. 8, no. 28, pp. 13687–13694, 2016.

[91] M. Lorenzon, L. Sortino, Q. Akkerman, S. Accornero, J. Pedrini, M. Prato, V. Pinchetti, F. Meinardi, L. Manna, and S. Brovelli, "Role of nonradiative defects and environmental oxygen on exciton recombination processes in CsPbBr3 perovskite nanocrystals," *Nano Letters*, vol. 17, no. 6, pp. 3844–3853, 2017.

[92] S. Gardelis, M. Fakis, N. Droseros, D. Georgiadou, A. Travlos, and A. G. Nassiopoulou, "Energy transfer in aggregated CuInS2/ZnS core-shell quantum dots deposited as solid films," *Journal of Physics D: Applied Physics*, vol. 50, no. 3, p. 035107, 2017.

[93] Y. Hamanaka, K. Watanabe, and T. Kuzuya, "Luminescence enhancement mechanisms of AgInS2/ZnS core/shell nanoparticles fabricated by suppressing quaternary alloying," *Journal of Luminescence*, vol. 217, p. 116794, jan 2020.

[94] V. Dzhagan, O. Selyshchev, O. Raievska, O. Stroyuk, L. Hertling, N. Mazur, M. Y. Valakh, and D. R. Zahn, "Phonon Spectra of Strongly Luminescent Non-stoichiometric Ag-In-S, Cu-In-S, and Hg-In-S Nanocrystals of Small Size," *Journal of Physical Chemistry C*, vol. 124, no. 28, pp. 15511–15522, 2020.

[95] C. Dujardin, E. Auffray, E. Bourret-Courchesne, P. Dorenbos, P. Lecoq, M. Nikl, A. N. Vasil'ev, A. Yoshikawa, and R.-Y. Zhu, "Needs, Trends, and Advances in Inorganic Scintillators," *IEEE Transactions on Nuclear Science*, vol. 65, pp. 1977–1997, aug 2018.

[96] C. Kim, W. Lee, A. Melis, A. Elmughrabi, K. Lee, C. Park, and J.-Y. Yeom, "A Review of Inorganic Scintillation Crystals for Extreme Environments," *Crystals*, vol. 11, p. 669, jun 2021.

[97] O. Stroyuk, A. Raevskaya, F. Spranger, O. Selyshchev, V. Dzhagan, S. Schulze, D. R. T. Zahn, and A. Eychmüller, "Origin and Dynamics of Highly Efficient Broadband Photoluminescence of Aqueous Glutathione-Capped Size-Selected Ag-In-S Quantum Dots," *The Journal of Physical Chemistry C*, vol. 122, pp. 13648–13658, jun 2018.

[98] M. D. Birowosuto, D. Cortecchia, W. Drozdowski, K. Brylew, W. Lachmanski, A. Bruno, and C. Soci, "X-ray Scintillation in Lead Halide Perovskite Crystals," *Scientific Reports*, vol. 6, p. 37254, dec 2016.

[99] Q. Chen, J. Wu, X. Ou, B. Huang, J. Almutlaq, A. A. Zhumekenov, X. Guan, S. Han, L. Liang, Z. Yi, J. Li, X. Xie, Y. Wang, Y. Li, D. Fan, D. B. Teh, A. H. All, O. F. Mohammed, O. M. Bakr, T. Wu, M. Bettinelli, H. Yang, W. Huang, and X. Liu, "All-inorganic perovskite nanocrystal scintillators," *Nature*, vol. 561, no. 7721, pp. 88–93, 2018.

[100] M. Gandini, I. Villa, M. Beretta, C. Gotti, M. Imran, F. Carulli, E. Fantuzzi, M. Sassi, M. Zaffalon, C. Brofferio, L. Manna, L. Beverina, A. Vedda, M. Fasoli, L. Gironi, and S. Brovelli, "Efficient, fast and reabsorption-free perovskite nanocrystal-based sensitized plastic scintillators," *Nature Nanotechnology*, vol. 15, pp. 462–468, jun 2020.

[101] Z. Xu, X. Tang, Y. Liu, Z. Zhang, W. Chen, K. Liu, and Z. Yuan, "CsPbBr 3 Quantum Dot Films with High Luminescence Efficiency and Irradiation Stability for Radioluminescent Nuclear Battery Application," *ACS Applied Materials and Interfaces*, vol. 11, pp. 14191–14199, apr 2019.

[102] W. Chen, Y. Liu, Z. Yuan, Z. Xu, Z. Zhang, K. Liu, Z. Jin, and X. Tang, "X-ray radioluminescence effect of all-inorganic halide perovskite CsPbBr3 quantum dots," *Journal of Radioanalytical and Nuclear Chemistry*, vol. 314, pp. 2327–2337, dec 2017.

[103] D. Yu, P. Wang, F. Cao, Y. Gu, J. Liu, Z. Han, B. Huang, Y. Zou, X. Xu, and H. Zeng, "Two-dimensional halide perovskite as β-ray scintillator for nuclear radiation monitoring," *Nature Communications*, vol. 11, p. 3395, dec 2020.

[104] H. Kraner, "Radiation detection and measurement," *Proceedings of the IEEE*, vol. 69, no. 4, pp. 495–495, 1981.

[105] Q. Xu, W. Shao, J. Liu, Z. Zhu, X. Ouyang, J. Cai, B. Liu, B. Liang, Z. Wu, and X. Ouyang, "Bulk Organic–Inorganic Methylammonium Lead Halide Perovskite Single Crystals for Indirect Gamma Ray Detection," *ACS Applied Materials and Interfaces*, vol. 11, pp. 47485–47490, dec 2019.

[106] H. Wei and J. Huang, "Halide lead perovskites for ionizing radiation detection," *Nature Communications*, vol. 10, p. 1066, dec 2019.

[107] L. Protesescu, S. Yakunin, M. I. Bodnarchuk, F. Krieg, R. Caputo, C. H. Hendon, R. X. Yang, A. Walsh, and M. V. Kovalenko, "Nanocrystals of Cesium Lead Halide Perovskites (CsPbX3, X = Cl, Br, and I): Novel Optoelectronic Materials Showing Bright Emission with Wide Color Gamut," *Nano Letters*, vol. 15, pp. 3692–3696, jun 2015.

[108] M. Imran, F. Di Stasio, Z. Dang, C. Canale, A. H. Khan, J. Shamsi, R. Brescia, M. Prato, and L. Manna, "Colloidal Synthesis of Strongly Fluorescent CsPbBr3Nanowires with Width Tunable down to the Quantum Confinement Regime," *Chemistry of Materials*, vol. 28, pp. 6450–6454, sep 2016.

[109] J. Shamsi, P. Rastogi, V. Caligiuri, A. L. Abdelhady, D. Spirito, L. Manna, and R. Krahne, "Bright-Emitting Perovskite Films by Large-Scale Synthesis and Photoinduced Solid-State Transformation of CsPbBr3 Nanoplatelets," *ACS Nano*, vol. 11, pp. 10206–10213, oct 2017.

[110] G. Nedelcu, L. Protesescu, S. Yakunin, M. I. Bodnarchuk, M. J. Grotevent, and M. V. Kovalenko, "Fast Anion-Exchange in Highly Luminescent Nanocrystals of Cesium Lead Halide Perovskites (CsPbX3, X = Cl, Br, I)," *Nano Letters*, vol. 15, no. 8, pp. 5635–5640, 2015.

[111] J. Liu, B. Shabbir, C. Wang, T. Wan, Q. Ou, P. Yu, A. Tadich, X. Jiao, D. Chu, D. Qi, D. Li, R. Kan, Y. Huang, Y. Dong, J. Jasieniak, Y. Zhang, and Q. Bao, "Flexible, Printable Soft-X-Ray Detectors Based on All-Inorganic Perovskite Quantum Dots," *Advanced Materials*, vol. 31, p. 1901644, jun 2019.

[112] A. Vedda, M. Fasoli, M. Nikl, V. V. Laguta, E. Mihokova, J. Pejchal, A. Yoshikawa, and M. Zhuravleva, "Trap-center recombination processes by rare earth activators in YAlO3 single crystal host," *Physical Review B - Condensed Matter and Materials Physics*, vol. 80, aug 2009.

[113] X. Y. Liu, G. Pilania, A. A. Talapatra, C. R. Stanek, and B. P. Uberuaga, "Band-Edge Engineering To Eliminate Radiation-Induced Defect States in Perovskite Scintillators," *ACS applied materials and interfaces*, vol. 12, pp. 46296–46305, oct 2020.

[114] M. Nikl, V. V. Laguta, and A. Vedda, "Complex oxide scintillators: Material defects and scintillation performance," *Physica Status Solidi (B) Basic Research*, vol. 245, pp. 1701–1722, sep 2008.

[115] M. Nikl and A. Yoshikawa, "Recent R\&D Trends in Inorganic Single-Crystal Scintillator Materials for Radiation Detection," *Advanced Optical Materials*, vol. 3, pp. 463–481, apr 2015.

[116] M. Kitaura, S. Watanabe, K. Kamada, K. Jin Kim, M. Yoshino, S. Kurosawa, T. Yagihashi, A. Ohnishi, and K. Hara, "Shallow electron traps formed by Gd2+ ions adjacent to oxygen vacancies in cerium-doped Gd3Al2Ga3O12 crystals," *Applied Physics Letters*, vol. 113, p. 41906, jul 2018.

[117] V. Babin, P. Bohacek, L. Grigorjeva, M. Kučera, M. Nikl, S. Zazubovich, and A. Zolotarjovs, "Effect of Mg2+ ions co-doping on luminescence and defects formation processes in Gd3(Ga,Al)5O12:Ce single crystals," *Optical Materials*, vol. 66, pp. 48–58, 2017.

[118] T. J. Hajagos, C. Liu, N. J. Cherepy, and Q. Pei, "High-Z Sensitized Plastic Scintillators: A Review," *Advanced Materials*, vol. 30, jul 2018.

[119] P. Lecoq, "Pushing the Limits in Time-of-Flight PET Imaging," *IEEE Transactions on Radiation and Plasma Medical Sciences*, vol. 1, no. 6, pp. 473–485, 2017.

[120] R. M. Turtos, S. Gundacker, A. Polovitsyn, S. Christodoulou, M. Salomoni, E. Auffray, I. Moreels, P. Lecoq, and J. Q. Grim, "Ultrafast emission from colloidal nanocrystals under pulsed X-ray excitation," *Journal of Instrumentation*, vol. 11, no. 10, 2016.

[121] A. Vedda, F. Moretti, M. Fasoli, M. Nikl, and V. Laguta, "Intrinsic trapping and recombination centers in CdWO4 investigated using thermally stimulated luminescence," *Physical Review B - Condensed Matter and Materials Physics*, vol. 80, aug 2009.

[122] M. Korzhik, G. Tamulaitis, and A. N. Vasil'ev, *Physics of Fast Processes in Scintillators*, vol. 49 of *Particle Acceleration and Detection*. Cham: Springer International Publishing, 2020.

[123] P. Lecoq, "Particle Physics Reference Library," in *Particle Physics Reference Library* (C. W. Fabjan and H. Schopper, eds.), ch. 3, pp. 337–382, Cham: Springer International Publishing, 2020.

[124] D. Totsuka, T. Yanagida, Y. Fujimoto, Y. Yokota, F. Moretti, A. Vedda, and A. Yoshikawa, "Afterglow suppression by codoping with Bi in CsI:TI crystal scintillator," *Applied Physics Express*, vol. 5, may 2012.

[125] O. Sidletskiy, A. Vedda, M. Fasoli, S. Neicheva, and A. Gektin, "Crystal Composition and Afterglow in Mixed Silicates: The Role of Melting Temperature," *Physical Review Applied*, vol. 4, aug 2015.

[126] A. Dey, P. Rathod, and D. Kabra, "Role of Localized States in Photoluminescence Dynamics of High Optical Gain CsPbBr3 Nanocrystals," *Advanced Optical Materials*, vol. 6, jun 2018.

[127] X. Lao, Z. Yang, Z. Su, Z. Wang, H. Ye, M. Wang, X. Yao, and S. Xu, "Luminescence and thermal behaviors of free and trapped excitons in cesium lead halide perovskite nanosheets," *Nanoscale*, vol. 10, no. 21, pp. 9949–9956, 2018.

[128] M. Dendebera, Y. Chornodolskyy, R. Gamernyk, O. Antonyak, I. Pashuk, S. Myagkota, I. Gnilitskyi, V. Pankratov, V. Vistovskyy, V. Mykhaylyk, M. Grin-

berg, and A. Voloshinovskii, "Time resolved luminescence spectroscopy of CsPbBr3 single crystal," *Journal of Luminescence*, vol. 225, p. 117346, sep 2020.

[129] V. S. Chirvony, S. González-Carrero, I. Suárez, R. E. Galian, M. Sessolo, H. J. Bolink, J. P. Martínez-Pastor, and J. Pérez-Prieto, "Delayed Luminescence in Lead Halide Perovskite Nanocrystals," *Journal of Physical Chemistry C*, vol. 121, pp. 13381–13390, jun 2017.

[130] V. B. Mykhaylyk, H. Kraus, V. Kapustianyk, H. J. Kim, P. Mercere, M. Rudko, P. Da Silva, O. Antonyak, and M. Dendebera, "Bright and fast scintillations of an inorganic halide perovskite CsPbBr3 crystal at cryogenic temperatures," *Scientific Reports*, vol. 10, p. 8601, dec 2020.

[131] M. Ito, S. J. Hong, and J. S. Lee, "Positron emission tomography (PET) detectors with depth-of- interaction (DOI) capability," *Biomedical Engineering Letters*, vol. 1, no. 2, pp. 70–81, 2011.

[132] J. Shamsi, A. S. Urban, M. Imran, L. De Trizio, and L. Manna, "Metal Halide Perovskite Nanocrystals: Synthesis, Post-Synthesis Modifications, and Their Optical Properties," *Chemical Reviews*, vol. 119, pp. 3296–3348, mar 2019.

[133] D. N. Dirin, L. Protesescu, D. Trummer, I. V. Kochetygov, S. Yakunin, F. Krumeich, N. P. Stadie, and M. V. Kovalenko, "Harnessing Defect-Tolerance at the Nanoscale: Highly Luminescent Lead Halide Perovskite Nanocrystals in Mesoporous Silica Matrixes," *Nano Letters*, vol. 16, no. 9, pp. 5866–5874, 2016.

[134] Y. C. Kim, K. H. Kim, D. Y. Son, D. N. Jeong, J. Y. Seo, Y. S. Choi, I. T. Han, S. Y. Lee, and N. G. Park, "Printable organometallic perovskite enables large-area, low-dose X-ray imaging," *Nature*, vol. 550, no. 7674, pp. 87–91, 2017.

[135] J. H. Heo, D. H. Shin, J. K. Park, D. H. Kim, S. J. Lee, and S. H. Im, "High-Performance Next-Generation Perovskite Nanocrystal Scintillator for Nondestructive X-Ray Imaging," *Advanced Materials*, vol. 30, no. 40, pp. 1–6, 2018.

[136] Y. He, L. Matei, H. J. Jung, K. M. McCall, M. Chen, C. C. Stoumpos, Z. Liu, J. A. Peters, D. Y. Chung, B. W. Wessels, M. R. Wasielewski, V. P. Dravid, A. Burger, and M. G. Kanatzidis, "High spectral resolution of gamma-rays at room temperature by perovskite CsPbBr3 single crystals," *Nature Communications*, vol. 9, no. 1, pp. 1–8, 2018.

[137] Y. Zhang, R. Sun, X. Ou, K. Fu, Q. Chen, Y. Ding, L. J. Xu, L. Liu, Y. Han, A. V. Malko, X. Liu, H. Yang, O. M. Bakr, H. Liu, and O. F. Mohammed, "Metal Halide Perovskite Nanosheet for X-ray High-Resolution Scintillation Imaging Screens," *ACS Nano*, vol. 13, pp. 2520–2525, feb 2019.

[138] H. Wei, Y. Fang, P. Mulligan, W. Chuirazzi, H.-H. Fang, C. Wang, B. R. Ecker, Y. Gao, M. A. Loi, L. Cao, and J. Huang, "Sensitive X-ray detectors made of methylammonium lead tribromide perovskite single crystals," *Nature Photonics*, vol. 10, pp. 333–339, may 2016.

[139] W. Wei, Y. Zhang, Q. Xu, H. Wei, Y. Fang, Q. Wang, Y. Deng, T. Li, A. Gruverman, L. Cao, and J. Huang, "Monolithic integration of hybrid perovskite single crystals with heterogenous substrate for highly sensitive X-ray imaging," *Nature Photonics*, vol. 11, no. 5, pp. 315–321, 2017.

[140] S. Yakunin, D. N. Dirin, Y. Shynkarenko, V. Morad, I. Cherniukh, O. Nazarenko, D. Kreil, T. Nauser, and M. V. Kovalenko, "Detection of gamma photons using solution-grown single crystals of hybrid lead halide perovskites," *Nature Photonics*, vol. 10, no. 9, pp. 585–589, 2016.

[141] S. Yakunin, M. Sytnyk, D. Kriegner, S. Shrestha, M. Richter, G. J. Matt, H. Azimi, C. J. Brabec, J. Stangl, M. V. Kovalenko, and W. Heiss, "Detection of X-ray photons by solution-processed lead halide perovskites," *Nature Photonics*, vol. 9, no. 7, pp. 444–449, 2015.

[142] Q. A. Akkerman, M. Gandini, F. Di Stasio, P. Rastogi, F. Palazon, G. Bertoni, J. M. Ball, M. Prato, A. Petrozza, and L. Manna, "Strongly emissive perovskite nanocrystal inks for high-voltage solar cells," *Nature Energy*, vol. 2, no. 2, 2017.

[143] C. Rodà, A. L. Abdelhady, J. Shamsi, M. Lorenzon, V. Pinchetti, M. Gandini, F. Meinardi, L. Manna, and S. Brovelli, "O2 as a molecular probe for nonradiative surface defects in CsPbBr3 perovskite nanostructures and single crystals," *Nanoscale*, vol. 11, no. 16, pp. 7613–7623, 2019.

[144] H. Henschel, J. Kuhnhenn, and U. Weinand, "Radiation hard optical fibers," in *OFC/NFOEC Technical Digest. Optical Fiber Communication Conference, 2005.*, p. 4 pp. Vol. 4, IEEE, 2005.

[145] G. Rainò, A. Landuyt, F. Krieg, C. Bernasconi, S. T. Ochsenbein, D. N. Dirin, M. I. Bodnarchuk, and M. V. Kovalenko, "Underestimated Effect of a Polymer

Matrix on the Light Emission of Single CsPbBr 3 Nanocrystals," *Nano Letters*, vol. 19, pp. 3648–3653, jun 2019.

[146] L. Feiler, H. Langhals, and K. Polborn, "Synthesis of perylene-3,4-dicarboximides — Novel highly photostable fluorescent dyes," *Liebigs Annalen*, vol. 1995, pp. 1229–1244, jul 1995.

[147] A. L. Bulin, A. Vasil'Ev, A. Belsky, D. Amans, G. Ledoux, and C. Dujardin, "Modelling energy deposition in nanoscintillators to predict the efficiency of the X-ray-induced photodynamic effect," *Nanoscale*, vol. 7, no. 13, pp. 5744–5751, 2015.

[148] M. Moszyński, M. Kapusta, M. Mayhugh, D. Wolski, and S. O. Flyckt, "Absolute light output of scintillators," *IEEE Transactions on Nuclear Science*, vol. 44, no. 3 PART 1, pp. 1052–1061, 1997.

[149] P. N. Zhmurin, Y. A. Gurkalenko, V. N. Pereymak, D. A. Eliseev, and O. V. Eliseeva, "Plastic Scintillators with the Improved Radiation Hardness Level," *Springer Proceedings in Physics*, vol. 227, pp. 125–145, 2019.

[150] W. Wolszczak, K. W. Krämer, and P. Dorenbos, "CsBa2I5:Eu2+,Sm2+—The First High-Energy Resolution Black Scintillator for γ-Ray Spectroscopy," *Physica Status Solidi - Rapid Research Letters*, vol. 13, sep 2019.

[151] P. Dorenbos, "The quest for high resolution γ-ray scintillators," *Optical Materials: X*, vol. 1, p. 100021, jan 2019.

[152] P. A. Rodnyi, "Core-valence luminescence in scintillators," *Radiation Measurements*, vol. 38, no. 4-6, pp. 343–352, 2004.

[153] R. Visser, P. Dorenbos, C. W. Van Eijk, and H. W. Den Hartog, "Energy transfer processes observed in the scintillation decay of BaF 2:La," *Journal of Physics: Condensed Matter*, vol. 4, no. 45, pp. 8801–8812, 1992.

[154] C. van Eijk, "Cross-luminescence," *Journal of Luminescence*, vol. 60-61, pp. 936–941, apr 1994.

[155] R. W. Novotny, K.-T. Brinkmann, V. Dormenev, M. Finger, J. Houzvicka, M. Korjik, P. Krist, S. Ochesanu, D. Petrydes, and H.-G. Zaunick, "High-Quality Lead Tungstate Crystals for PANDA Produced at CRYTUR," *IEEE Transactions on Nuclear Science*, vol. 65, pp. 1998–2003, aug 2018.

[156] M. I. Saidaminov, M. A. Haque, J. Almutlaq, S. Sarmah, X. H. Miao, R. Begum, A. A. Zhumekenov, I. Dursun, N. Cho, B. Murali, O. F. Mohammed, T. Wu, and O. M. Bakr, "Inorganic Lead Halide Perovskite Single Crystals: Phase-Selective Low-Temperature Growth, Carrier Transport Properties, and Self-Powered Photodetection," *Advanced Optical Materials*, vol. 5, jan 2017.

[157] S. W. S. McKeever and R. H. Bube, "Thermoluminescence of Solids," *Physics Today*, vol. 40, pp. 80–81, apr 1987.

[158] K. Schötz, A. M. Askar, W. Peng, D. Seeberger, T. P. Gujar, M. Thelakkat, A. Köhler, S. Huettner, O. M. Bakr, K. Shankar, and F. Panzer, "Double peak emission in lead halide perovskites by self-absorption," *Journal of Materials Chemistry C*, vol. 8, no. 7, pp. 2289–2300, 2020.

[159] Y. Liu, J. Wang, L. Zhang, W. Liu, C. Wu, C. Liu, Z. Wu, L. Xiao, Z. Chen, and S. Wang, " Exciton and bi-exciton mechanisms in amplified spontaneous emission from CsPbBr 3 perovskite thin films ," *Optics Express*, vol. 27, no. 20, p. 29124, 2019.

[160] M. Sebastian, J. A. Peters, C. C. Stoumpos, J. Im, S. S. Kostina, Z. Liu, M. G. Kanatzidis, A. J. Freeman, and B. W. Wessels, "Excitonic emissions and above-band-gap luminescence in the single-crystal perovskite semiconductors CsPbB r3 and CsPbC l3," *Physical Review B - Condensed Matter and Materials Physics*, vol. 92, dec 2015.

[161] S. V. Myagkota, A. V. Gloskovskiĭ, and A. S. Voloshinovskiĭ, "Photo- and X-ray Luminescence Spectra of CsPbX3 Microcrystals Dispersed in a PbX2 (X = Cl, Br) Matrix," *Optics and Spectroscopy (English translation of Optika i Spektroskopiya)*, vol. 88, pp. 538–541, apr 2000.

[162] S. T. Birkhold, E. Zimmermann, T. Kollek, D. Wurmbrand, S. Polarz, and L. Schmidt-Mende, "Impact of Crystal Surface on Photoexcited States in Organic-Inorganic Perovskites," *Advanced Functional Materials*, vol. 27, p. 1604995, feb 2017.

[163] T. Yamada, Y. Yamada, Y. Nakaike, A. Wakamiya, and Y. Kanemitsu, "Photon Emission and Reabsorption Processes in CH3NH3PbBr3 Single Crystals Revealed by Time-Resolved Two-Photon-Excitation Photoluminescence Microscopy," *Physical Review Applied*, vol. 7, jan 2017.

[164] A. Shinde, R. Gahlaut, and S. Mahamuni, "Low-Temperature Photoluminescence Studies of CsPbBr3 Quantum Dots," *Journal of Physical Chemistry C*, vol. 121, pp. 14872–14878, jul 2017.

[165] K. Wei, Z. Xu, R. Chen, X. Zheng, X. Cheng, and T. Jiang, "Temperature-dependent excitonic photoluminescence excited by two-photon absorption in perovskite CsPbBr3 quantum dots," *Optics Letters*, vol. 41, no. 16, p. 3821, 2016.

[166] K. Shibata, J. Yan, Y. Hazama, S. Chen, and H. Akiyama, "Exciton Localization and Enhancement of the Exciton-LO Phonon Interaction in a CsPbBr3Single Crystal," *Journal of Physical Chemistry C*, vol. 124, pp. 18257–18263, aug 2020.

[167] M. A. Becker, R. Vaxenburg, G. Nedelcu, P. C. Sercel, A. Shabaev, M. J. Mehl, J. G. Michopoulos, S. G. Lambrakos, N. Bernstein, J. L. Lyons, T. Stöferle, R. F. Mahrt, M. V. Kovalenko, D. J. Norris, G. Rainò, and A. L. Efros, "Bright triplet excitons in caesium lead halide perovskites," *Nature*, vol. 553, pp. 189–193, jan 2018.

[168] R. Visocekas, M. Ouchene, and B. Gallois, "Tunneling afterglow and anomalous fading in dosimetry with CaSO4:Dy," *Nuclear Instruments and Methods In Physics Research*, vol. 214, no. 2-3, pp. 553–555, 1983.

[169] M. Nikl, A. Vedda, M. Fasoli, I. Fontana, V. V. Laguta, E. Mihokova, J. Pejchal, J. Rosa, and K. Nejezchleb, "Shallow traps and radiative recombination processes in Lu3 Al5 O12: Ce single crystal scintillator," *Physical Review B - Condensed Matter and Materials Physics*, vol. 76, p. 195121, nov 2007.

[170] A. Vedda and M. Fasoli, "Tunneling recombinations in scintillators, phosphors, and dosimeters," *Radiation Measurements*, vol. 118, no. June, pp. 86–97, 2018.

[171] A. C. Coleman and E. G. Yukihara, "On the validity and accuracy of the initial rise method investigated using realistically simulated thermoluminescence curves," *Radiation Measurements*, vol. 117, pp. 70–79, oct 2018.

[172] M. Liu, Q. Wan, H. Wang, F. Carulli, X. Sun, W. Zheng, L. Kong, Q. Zhang, C. Zhang, Q. Zhang, S. Brovelli, and L. Li, "Suppression of temperature quenching in perovskite nanocrystals for efficient and thermally stable light-emitting diodes," *Nature Photonics*, vol. 15, pp. 379–385, may 2021.

[173] I. Holl, E. Loren, and G. Mageras, "A measurement of the light yield of common inorganic scintillators," *IEEE Transactions on Nuclear Science*, vol. 35, no. 1, pp. 105–109, 1988.

[174] J. Hubbell and S. J. G. Seltzer, "NIST Standard Reference Database 126," 1996.

[175] L. Yang, H. Zhang, M. Zhou, L. Zhao, W. Chen, T. Wang, X. Yu, D. Zhou, J. Qiu, and X. Xu, "High-Stable X-ray Imaging from All-Inorganic Perovskite Nanocrystals under a High Dose Radiation," *The Journal of Physical Chemistry Letters*, vol. 11, pp. 9203–9209, nov 2020.

[176] Q. Xu, H. Zhang, J. Nie, W. Shao, X. Wang, B. Zhang, and X. Ouyang, "Effect of methylammonium lead tribromide perovskite based-photoconductor under gamma photons radiation," *Radiation Physics and Chemistry*, vol. 181, p. 109337, apr 2021.

[177] A. G. Boldyreva, L. A. Frolova, I. S. Zhidkov, L. G. Gutsev, E. Z. Kurmaev, B. R. Ramachandran, V. G. Petrov, K. J. Stevenson, S. M. Aldoshin, and P. A. Troshin, "Unravelling the Material Composition Effects on the Gamma Ray Stability of Lead Halide Perovskite Solar Cells: MAPbI 3 Breaks the Records," *The Journal of Physical Chemistry Letters*, vol. 11, pp. 2630–2636, apr 2020.

[178] Q. Xu, J. Wang, W. Shao, X. Ouyang, X. Wang, X. Zhang, Y. Guo, and X. Ouyang, "A solution-processed zero-dimensional all-inorganic perovskite scintillator for high resolution gamma-ray spectroscopy detection," *Nanoscale*, vol. 12, no. 17, pp. 9727–9732, 2020.

[179] Q. Xu, J. Huang, J. Liu, J. Wang, S. Zhou, X. Wang, J. Nie, Y. Guo, and X. Ouyang, "Lead halide perovskite quantum dots based liquid scintillator for x-ray detection," *Nanotechnology*, vol. 32, p. 205201, may 2021.

[180] G. Mannino, I. Deretzis, E. Smecca, A. La Magna, A. Alberti, D. Ceratti, and D. Cahen, "Temperature-Dependent Optical Band Gap in CsPbBr3, MAPbBr3, and FAPbBr3 Single Crystals," *Journal of Physical Chemistry Letters*, vol. 11, pp. 2490–2496, apr 2020.

[181] J. Butkus, P. Vashishtha, K. Chen, J. K. Gallaher, S. K. Prasad, D. Z. Metin, G. Laufersky, N. Gaston, J. E. Halpert, and J. M. Hodgkiss, "The Evolution of Quantum Confinement in CsPbBr3 Perovskite Nanocrystals," *Chemistry of Materials*, vol. 29, pp. 3644–3652, apr 2017.

[182] E. Auffray, G. Dosovitskiy, A. Fedorov, I. Guz, M. Korjik, N. Kratochwill, M. Lucchini, S. Nargelas, D. Kozlov, V. Mechinsky, P. Orsich, O. Sidletskiy, G. Tamulaitis, and A. Vaitkevičius, "Irradiation effects on Gd3Al2Ga3O12 scintillators prospective for application in harsh irradiation environments," *Radiation Physics and Chemistry*, vol. 164, nov 2019.

[183] H. J. Snaith, "Present status and future prospects of perovskite photovoltaics," *Nature Materials*, vol. 17, pp. 372–376, may 2018.

[184] Q. A. Akkerman, G. Rainò, M. V. Kovalenko, and L. Manna, "Genesis, challenges and opportunities for colloidal lead halide perovskite nanocrystals," *Nature Materials*, vol. 17, pp. 394–405, may 2018.

[185] S. Ghosh and B. Pradhan, "Lead-Free Metal Halide Perovskite Nanocrystals: Challenges, Applications, and Future Aspects," *ChemNanoMat*, vol. 5, pp. 300–312, mar 2019.

[186] H. Fu, "Review of lead-free halide perovskites as light-absorbers for photovoltaic applications: From materials to solar cells," *Solar Energy Materials and Solar Cells*, vol. 193, pp. 107–132, may 2019.

[187] F. Giustino and H. J. Snaith, "Toward Lead-Free Perovskite Solar Cells," *ACS Energy Letters*, vol. 1, pp. 1233–1240, dec 2016.

[188] Y. Bekenstein, J. C. Dahl, J. Huang, W. T. Osowiecki, J. K. Swabeck, E. M. Chan, P. Yang, and A. P. Alivisatos, "The Making and Breaking of Lead-Free Double Perovskite Nanocrystals of Cesium Silver-Bismuth Halide Compositions," *Nano Letters*, vol. 18, pp. 3502–3508, jun 2018.

[189] S. E. Creutz, E. N. Crites, M. C. De Siena, and D. R. Gamelin, "Colloidal Nanocrystals of Lead-Free Double-Perovskite (Elpasolite) Semiconductors: Synthesis and Anion Exchange to Access New Materials," *Nano Letters*, vol. 18, pp. 1118–1123, feb 2018.

[190] Y. Liu, Y. Jing, J. Zhao, Q. Liu, and Z. Xia, "Design Optimization of Lead-Free Perovskite Cs2AgInCl6:Bi Nanocrystals with 11.4% Photoluminescence Quantum Yield," *Chemistry of Materials*, vol. 31, pp. 3333–3339, may 2019.

[191] J. C. Dahl, W. T. Osowiecki, Y. Cai, J. K. Swabeck, Y. Bekenstein, M. Asta, E. M. Chan, and A. P. Alivisatos, "Probing the Stability and Band Gaps of

Cs 2 AgInCl 6 and Cs 2 AgSbCl 6 Lead-Free Double Perovskite Nanocrystals," *Chemistry of Materials*, vol. 31, pp. 3134–3143, may 2019.

[192] J. Breternitz, S. Levcenko, H. Hempel, G. Gurieva, A. Franz, A. Hoser, and S. Schorr, "Mechanochemical synthesis of the lead-free double perovskite Cs2[AgIn]Br6 and its optical properties," *JPhys Energy*, vol. 1, p. 025003, may 2019.

[193] B. Yang, F. Hong, J. Chen, Y. Tang, L. Yang, Y. Sang, X. Xia, J. Guo, H. He, S. Yang, W. Deng, and K. Han, "Colloidal Synthesis and Charge-Carrier Dynamics of Cs 2 AgSb 1-y Bi y X 6 (X: Br, Cl) Double Perovskite Nanocrystals," *Angewandte Chemie - International Edition*, vol. 58, pp. 2278–2283, feb 2019.

[194] W. Deng, Z. Y. Deng, J. He, M. Wang, Z. X. Chen, S. H. Wei, and H. J. Feng, "Synthesis of Cs2AgSbCl6 and improved optoelectronic properties of Cs2AgSbCl6/TiO2 heterostructure driven by the interface effect for lead-free double perovskites solar cells," *Applied Physics Letters*, vol. 111, p. 151602, oct 2017.

[195] T. T. Tran, J. R. Panella, J. R. Chamorro, J. R. Morey, and T. M. McQueen, "Designing indirect-direct bandgap transitions in double perovskites," *Materials Horizons*, vol. 4, no. 4, pp. 688–693, 2017.

[196] K. Z. Du, W. Meng, X. Wang, Y. Yan, and D. B. Mitzi, "Bandgap Engineering of Lead-Free Double Perovskite Cs2AgBiBr6 through Trivalent Metal Alloying," *Angewandte Chemie - International Edition*, vol. 56, pp. 8158–8162, jul 2017.

[197] W. Meng, X. Wang, Z. Xiao, J. Wang, D. B. Mitzi, and Y. Yan, "Parity-Forbidden Transitions and Their Impact on the Optical Absorption Properties of Lead-Free Metal Halide Perovskites and Double Perovskites," *Journal of Physical Chemistry Letters*, vol. 8, pp. 2999–3007, jul 2017.

[198] J. Luo, S. Li, H. Wu, Y. Zhou, Y. Li, J. Liu, J. Li, K. Li, F. Yi, G. Niu, and J. Tang, "Cs2AgInCl6 Double Perovskite Single Crystals: Parity Forbidden Transitions and Their Application for Sensitive and Fast UV Photodetectors," *ACS Photonics*, vol. 5, pp. 398–405, feb 2018.

[199] F. Locardi, M. Cirignano, D. Baranov, Z. Dang, M. Prato, F. Drago, M. Ferretti, V. Pinchetti, M. Fanciulli, S. Brovelli, L. De Trizio, and L. Manna, "Colloidal Synthesis of Double Perovskite Cs2AgInCl6 and Mn-Doped Cs2AgInCl6

Nanocrystals," *Journal of the American Chemical Society*, vol. 140, pp. 12989–12995, oct 2018.

[200] G. Volonakis, A. A. Haghighirad, R. L. Milot, W. H. Sio, M. R. Filip, B. Wenger, M. B. Johnston, L. M. Herz, H. J. Snaith, and F. Giustino, "Cs2InAgCl6: A New Lead-Free Halide Double Perovskite with Direct Band Gap," *Journal of Physical Chemistry Letters*, vol. 8, pp. 772–778, feb 2017.

[201] A. Karmakar, M. S. Dodd, S. Agnihotri, E. Ravera, and V. K. Michaelis, "Cu(II)-Doped Cs2SbAgCl6 Double Perovskite: A Lead-Free, Low-Bandgap Material," *Chemistry of Materials*, vol. 30, pp. 8280–8290, nov 2018.

[202] K. Nila Nandha and A. Nag, "Synthesis and luminescence of Mn-doped Cs2AgInCl6 double perovskites," *Chemical Communications*, vol. 54, no. 41, pp. 5205–5208, 2018.

[203] J. Zhou, X. Rong, P. Zhang, M. S. Molokeev, P. Wei, Q. Liu, X. Zhang, and Z. Xia, "Manipulation of Bi 3+ /In 3+ Transmutation and Mn 2+ -Doping Effect on the Structure and Optical Properties of Double Perovskite Cs 2 NaBi 1-x In x Cl 6," *Advanced Optical Materials*, vol. 7, apr 2019.

[204] J. D. Majher, M. B. Gray, T. A. Strom, and P. M. Woodward, "Cs 2 NaBiCl 6 :Mn 2+ - A New Orange-Red Halide Double Perovskite Phosphor," *Chemistry of Materials*, vol. 31, pp. 1738–1744, mar 2019.

[205] N. Chen, T. Cai, W. Li, K. Hills-Kimball, H. Yang, M. Que, Y. Nagaoka, Z. Liu, D. Yang, A. Dong, C. Y. Xu, R. Zia, and O. Chen, "Yb- and Mn-Doped Lead-Free Double Perovskite Cs 2 AgBiX 6 (X = Cl - , Br -) Nanocrystals," *ACS Applied Materials and Interfaces*, vol. 11, pp. 16855–16863, may 2019.

[206] W. Lee, S. Hong, and S. Kim, "Colloidal Synthesis of Lead-Free Silver-Indium Double-Perovskite Cs 2 AgInCl 6 Nanocrystals and Their Doping with Lanthanide Ions," *Journal of Physical Chemistry C*, vol. 123, pp. 2665–2672, jan 2019.

[207] S. Khalfin and Y. Bekenstein, "Advances in lead-free double perovskite nanocrystals, engineering band-gaps and enhancing stability through composition tunability," *Nanoscale*, vol. 11, no. 18, pp. 8665–8679, 2019.

[208] J. Luo, X. Wang, S. Li, J. Liu, Y. Guo, G. Niu, L. Yao, Y. Fu, L. Gao, Q. Dong, C. Zhao, M. Leng, F. Ma, W. Liang, L. Wang, S. Jin, J. Han, L. Zhang, J. Etheridge, J. Wang, Y. Yan, E. H. Sargent, and J. Tang, "Efficient and stable emission of warm-white light from lead-free halide double perovskites," *Nature*, vol. 563, pp. 541–545, nov 2018.

[209] S. V. Yurtaeva, A. E. Usachev, and Y. V. Yablokov, "Spin-spin interactions of Ce3+ ions in the elpasolite crystal Cs2NaInCl6," *Physics of the Solid State*, vol. 39, no. 7, pp. 1075–1080, 1997.

[210] L. R. Morss, M. Siegal, L. Stenger, and N. Edelstein, "Preparation of Cubic Chloro Complex Compounds of Trivalent Metals: Cs2NaM Cl61a," *Inorganic Chemistry*, vol. 9, pp. 1771–1775, jul 1970.

[211] J. Hutter, M. Iannuzzi, F. Schiffmann, and J. Vandevondele, "Cp2k: Atomistic simulations of condensed matter systems," *Wiley Interdisciplinary Reviews: Computational Molecular Science*, vol. 4, pp. 15–25, jan 2014.

[212] J. P. Perdew, K. Burke, and M. Ernzerhof, "Generalized gradient approximation made simple," *Physical Review Letters*, vol. 77, no. 18, pp. 3865–3868, 1996.

[213] J. Zhou, Z. Xia, M. S. Molokeev, X. Zhang, D. Peng, and Q. Liu, "Composition design, optical gap and stability investigations of lead-free halide double perovskite Cs2AgInCl6," *Journal of Materials Chemistry A*, vol. 5, no. 29, pp. 15031–15037, 2017.

[214] F. Meinardi, A. Colombo, K. A. Velizhanin, R. Simonutti, M. Lorenzon, L. Beverina, R. Viswanatha, V. I. Klimov, and S. Brovelli, "Large-area luminescent solar concentrators based on Stokes-shift-engineered nanocrystals in a mass-polymerized PMMA matrix," *Nature Photonics*, vol. 8, no. 5, pp. 392–399, 2014.

[215] F. Zhao, Z. Song, J. Zhao, and Q. Liu, "Double perovskite Cs2AgInCl6:Cr3+: Broadband and near-infrared luminescent materials," *Inorganic Chemistry Frontiers*, vol. 6, no. 12, pp. 3621–3628, 2019.

[216] K. Dave, M. H. Fang, Z. Bao, H. T. Fu, and R. S. Liu, "Recent Developments in Lead-Free Double Perovskites: Structure, Doping, and Applications," *Chemistry - An Asian Journal*, vol. 15, pp. 242–252, jan 2020.

[217] X. G. Zhao, D. Yang, J. C. Ren, Y. Sun, Z. Xiao, and L. Zhang, "Rational Design of Halide Double Perovskites for Optoelectronic Applications," *Joule*, vol. 2, no. 9, pp. 1662–1673, 2018.

[218] Y. Mahor, W. J. Mir, and A. Nag, "Synthesis and Near-Infrared Emission of Yb-Doped Cs 2 AgInCl 6 Double Perovskite Microcrystals and Nanocrystals," *The Journal of Physical Chemistry C*, vol. 123, pp. 15787–15793, jun 2019.

[219] D. Manna, T. K. Das, and A. Yella, "Tunable and Stable White Light Emission in Bi3+-Alloyed Cs2AgInCl6 Double Perovskite Nanocrystals," *Chemistry of Materials*, vol. 31, pp. 10063–10070, dec 2019.

[220] M. B. Gray, J. D. Majher, T. A. Strom, and P. M. Woodward, "Broadband White Emission in Cs2AgIn1- xBixCl6 Phosphors," *Inorganic Chemistry*, vol. 58, pp. 13403–13410, oct 2019.

[221] B. Zhang, M. Wang, M. Ghini, A. E. Melcherts, J. Zito, L. Goldoni, I. Infante, M. Guizzardi, F. Scotognella, I. Kriegel, L. De Trizio, and L. Manna, "Colloidal Bi-Doped Cs2Ag1- xNaxInCl6Nanocrystals: Undercoordinated Surface Cl Ions Limit their Light Emission Efficiency," *ACS Materials Letters*, vol. 2, pp. 1442–1449, nov 2020.

[222] W. Lee, D. Choi, and S. Kim, "Colloidal synthesis of shape-controlled Cs2NaBiX6(X = Cl, Br) double perovskite nanocrystals: Discrete optical transition by non-bonding characters and energy transfer to Mn dopants," *Chemistry of Materials*, vol. 32, pp. 6864–6874, aug 2020.

[223] F. Locardi, E. Sartori, J. Buha, J. Zito, M. Prato, V. Pinchetti, M. L. Zaffalon, M. Ferretti, S. Brovelli, I. Infante, L. De Trizio, and L. Manna, "Emissive Bi-Doped Double Perovskite Cs2Ag1- xNaxInCl6 Nanocrystals," *ACS Energy Letters*, vol. 4, pp. 1976–1982, aug 2019.

[224] B. Yang, X. Mao, F. Hong, W. Meng, Y. Tang, X. Xia, S. Yang, W. Deng, and K. Han, "Lead-Free Direct Band Gap Double-Perovskite Nanocrystals with Bright Dual-Color Emission," *Journal of the American Chemical Society*, vol. 140, pp. 17001–17006, dec 2018.

[225] R. Zeng, L. Zhang, Y. Xue, B. Ke, Z. Zhao, D. Huang, Q. Wei, W. Zhou, and B. Zou, "Highly Efficient Blue Emission from Self-Trapped Excitons in Stable

Sb3+-Doped Cs2NaInCl6 Double Perovskites," *Journal of Physical Chemistry Letters*, vol. 11, no. 6, pp. 2053–2061, 2020.

[226] S. Wu, W. Li, J. Hu, and P. Gao, "Antimony doped lead-free double perovskites (Cs2NaBi1-: xSbxCl6) with enhanced light absorption and tunable emission," *Journal of Materials Chemistry C*, vol. 8, no. 39, pp. 13603–13611, 2020.

[227] M. B. Gray, S. Hariyani, T. A. Strom, J. D. Majher, J. Brgoch, and P. M. Woodward, "High-efficiency blue photoluminescence in the Cs2NaInCl6:Sb3+double perovskite phosphor," *Journal of Materials Chemistry C*, vol. 8, no. 20, pp. 6797–6803, 2020.

[228] A. Noculak, A. Noculak, V. Morad, V. Morad, K. M. McCall, S. Yakunin, Y. Shynkarenko, S. Yakunin, Y. Shynkarenko, M. Wörle, and M. V. Kovalenko, "Bright Blue and Green Luminescence of Sb(III) in Double Perovskite Cs2MInCl6(M = Na, K) Matrices," *Chemistry of Materials*, vol. 32, no. 12, pp. 5118–5124, 2020.

[229] K. M. McCall, V. Morad, B. M. Benin, and M. V. Kovalenko, "Efficient Lone-Pair-Driven Luminescence: Structure-Property Relationships in Emissive 5s2Metal Halides," *ACS Materials Letters*, vol. 2, pp. 1218–1232, sep 2020.

[230] X. Liu, X. Xu, B. Li, L. Yang, Q. Li, H. Jiang, and D. Xu, "Tunable Dual-Emission in Monodispersed Sb3+/Mn2+ Codoped Cs2NaInCl6 Perovskite Nanocrystals through an Energy Transfer Process," *Small*, vol. 16, no. 31, pp. 1–7, 2020.

[231] E. W. Oomen, W. M. Smit, and G. Blasse, "On the luminescence of sb3+in cs2namcl6 (With m = sc, y, la): A model system for the study of trivalent s2 ions," *Journal of Physics C: Solid State Physics*, vol. 19, no. 17, pp. 3263–3272, 1986.

[232] Y. Jing, Y. Liu, J. Zhao, and Z. Xia, "Sb3+ Doping-Induced Triplet Self-Trapped Excitons Emission in Lead-Free Cs2SnCl6 Nanocrystals," *Journal of Physical Chemistry Letters*, vol. 10, pp. 7439–7444, dec 2019.

[233] J. Li, Z. Tan, M. Hu, C. Chen, J. Luo, S. Li, L. Gao, Z. Xiao, G. Niu, and J. Tang, "Antimony doped Cs2SnCl6 with bright and stable emission," *Frontiers of Optoelectronics*, vol. 12, pp. 352–364, dec 2019.

[234] J. D. Majher, M. B. Gray, T. Liu, N. P. Holzapfel, and P. M. Woodward, "Rb3InCl6: A Monoclinic Double Perovskite Derivative with Bright Sb3+-Activated Photoluminescence," *Inorganic Chemistry*, vol. 59, no. 19, pp. 14478–14485, 2020.

[235] Y. Jing, Y. Liu, X. Jiang, M. S. Molokeev, Z. Lin, and Z. Xia, "Sb 3+ Dopant and Halogen Substitution Triggered Highly Efficient and Tunable Emission in Lead-Free Metal Halide Single Crystals," *Chemistry of Materials*, vol. 32, pp. 5327–5334, jun 2020.

[236] P. Han, C. Luo, S. Yang, Y. Yang, W. Deng, and K. Han, "All-Inorganic Lead-Free 0D Perovskites by a Doping Strategy to Achieve a PLQY Boost from <2 % to 90 %," *Angewandte Chemie - International Edition*, vol. 59, pp. 12709–12713, jul 2020.

[237] H. Arfin, A. S. Kshirsagar, J. Kaur, B. Mondal, Z. Xia, S. Chakraborty, and A. Nag, "ns 2 Electron (Bi 3+ and Sb 3+) Doping in Lead-Free Metal Halide Perovskite Derivatives," *Chemistry of Materials*, vol. 32, pp. 10255–10267, dec 2020.

[238] X. Liu, X. Xu, B. Li, Y. Liang, Q. Li, H. Jiang, and D. Xu, "Antimony-doping induced highly efficient warm-white emission in indium-based zero-dimensional perovskites," *CCS Chemistry*, vol. 2, pp. 216–224, apr 2020.

[239] B. Zhang, V. Pinchetti, J. Zito, A. Ray, A. E. M. Melcherts, M. Ghini, A. Pianetti, I. Infante, S. Brovelli, L. De Trizio, and L. Manna, " Isolated [SbCl 6] 3– Octahedra Are the Only Active Emitters in Rb 7 Sb 3 Cl 16 Nanocrystals ," *ACS Energy Letters*, pp. 3952–3959, oct 2021.

[240] G. S. Pawley, "Unit-cell refinement from powder diffraction scans," *Journal of Applied Crystallography*, vol. 14, no. 6, pp. 357–361, 1981.

[241] J. Dean, "LANGE'S HANDBOOK OF CHEMISTRY," *Materials and Manufacturing Processes*, vol. 5, pp. 687–688, jan 1990.

[242] M. Yuan, L. N. Quan, R. Comin, G. Walters, R. Sabatini, O. Voznyy, S. Hoogland, Y. Zhao, E. M. Beauregard, P. Kanjanaboos, Z. Lu, D. H. Kim, and E. H. Sargent, "Perovskite energy funnels for efficient light-emitting diodes," *Nature Nanotechnology*, vol. 11, no. 10, pp. 872–877, 2016.

[243] D. Zhu, J. Zito, V. Pinchetti, Z. Dang, A. Olivati, L. Pasquale, A. Tang, M. L. Zaffalon, F. Meinardi, I. Infante, L. De Trizio, L. Manna, and S. Brovelli, "Compositional Tuning of Carrier Dynamics in Cs2Na1- xAgxBiCl6Double-Perovskite Nanocrystals," *ACS Energy Letters*, vol. 5, pp. 1840–1847, jun 2020.

[244] D. Zhu, M. L. Zaffalon, J. Zito, F. Cova, F. Meinardi, L. De Trizio, I. Infante, S. Brovelli, and L. Manna, "Sb-Doped Metal Halide Nanocrystals: A 0D versus 3D Comparison," *ACS Energy Letters*, vol. 6, pp. 2283–2292, jun 2021.